UC Santa Barbara
UC Santa Barbara Electronic Theses and Dissertations

Title
Phase Behavior, Processing, and Properties of Thermoresponsive Colloidal Gels

Permalink
https://escholarship.org/uc/item/3rp8f240

Author
Nguyen, Tuan Terrence Do

Publication Date
2020

Peer reviewed|Thesis/dissertation

eScholarship.org Powered by the California Digital Library
University of California

University of California
Santa Barbara

Phase Behavior, Processing, and Properties of Thermoresponsive Colloidal Gels

A dissertation submitted in partial satisfaction
of the requirements for the degree

Doctor of Philosophy
in
Chemical Engineering

by

Tuan Terrence Do Nguyen

Committee in charge:

Professor Matthew E. Helgeson, Chair
Professor Glenn H. Fredrickson
Professor M. Scott Shell
Professor Omar A. Saleh

March 2020

The Dissertation of Tuan Terrence Do Nguyen is approved.

Professor Glenn H. Fredrickson

Professor M. Scott Shell

Professor Omar A. Saleh

Professor Matthew E. Helgeson, Committee Chair

January 2020

Phase Behavior, Processing, and Properties of Thermoresponsive Colloidal Gels

Copyright © 2020

by

Tuan Terrence Do Nguyen

To my parents, Thành and Lan.

Acknowledgements

I have a great many people to acknowledge for their presence and participation throughout my doctorate journey. Upon entering UCSB I naïvely ascribed to the notion that PhD research would be a tremendously solitary experience, but I think that the many thanks below should help to refute that notion.

I am first and foremost grateful for Matt — for his wisdom, steadiness, and humor as my advisor. If nothing else, I will strive for his level of understanding in all my future endeavors. I valued both the scientific freedom he permitted me in times of exploration, as well as the reassuring guidance he provided me in times of disorientation. His mentorship helped me think more critically about my work and not be satisfied with just data and information, and for all of these lessons I will be forever thankful.

I would not have been able to delve into the tools, techniques, and thinking associated with my dissertation topic without the help of some friendly neighborhood researchers. To begin, I would like to thank Juntae Kim, Paula Malo de Molina, Emma Filippidi, Alexandra Bayles, and Yongxiang Gao for helping me get started during my first year. I would also like to thank Peng Cheng, Gwen Zhang, Patrick Corona, Mike Burroughs, Nick Sherck, and Scott Fenton for their inquisitive discussions regarding my project. I would like to thank Yuanming Zhang, Shamon Walker, and Jennifer Smith for their instrument scientist expertise, and I would like to thank our collaborators — Roseanna Zia, Poornima Padmanabhan, Lilian Johnson, and Brian Ryu through the DMREF project, and Abhi Shetty through the Anton Paar VIP Program. The UCSB atmosphere truly fostered my appreciation for the many possibilities enabled by cooperative scientific research.

Outside of UCSB, I was fortunate to have a reliable network of friends and friends of friends to partake in non-research activities with me over the years, whether that meant enjoying the great outdoors, grabbing a bite to eat, drinking Central Coast wine and beer, running a marathon, or playing all manner of board games. In hopes that they read at least this far into my dissertation, I will list a few of them here: Johnny Jung, Frances Chen, Frank Liu, Minnie Lai, Obosa Obazuaye, Sam Yim, Diana Mar, Jason Wang, Rohaine Hsu, Lisa Gai, Sarah Tran, Ryan Su, Camille Amparo, Karina Hwang, Justin Yoo, Elizabeth Hiroyasu, Christopher Uraine, Brian Markman, Jacob Monroe, Cheyenne Lynsky, Chris Pynn, Daniil Bochkov, and of course Momo. I am glad that our personal friendships had the space to grow even while I was busy growing as a researcher.

I am even more so fortunate to have a sizeable family in California and across the country totaling some thirty uncles and aunts and fifty or so first cousins. My heart and stomach remained continuously full owing to the many holiday gatherings and family celebrations that populated various weekends and breaks. I especially would like to acknowledge my closest family including Bố, Mom, Anh Trung, Christy, Anh Tín, Sara, Lily, Tyler, and Evan. Thank you all so much for always loving me and instilling in me the mental fortitude to tackle this arduous academic undertaking. I hope to continue to make you proud through what I do and who I am.

Finally, I want to end by expressing my deepest thanks and five-ever love to Lesley Chan for being my partner through this chapter of not only my life but also our relationship. Her spirited presence and unwavering support throughout these grad school days, whether unremarkable or exhilarating, have without a doubt made me the luckiest person in the known universe. I only hope I am able to echo her optimistic perseverance as we go on to face future successes, failures, and everything in between. And most of all, I look forward to the weeks, months, years, and decades that lie ahead for us.

Curriculum Vitæ

Tuan Terrence Do Nguyen

Education

2020 (expected)	Doctor of Philosophy in Chemical Engineering, University of California, Santa Barbara
2014	Bachelor of Science in Engineering with High Distinction, Harvey Mudd College, Claremont, California

Professional Appointments

2014–2020	Graduate Research Assistant, Department of Chemical Engineering, University of California, Santa Barbara
2015–2018	Graduate Teaching Assistant, Department of Chemical Engineering, University of California, Santa Barbara
2012–2014	Undergraduate Research Assistant, Department of Engineering, Harvey Mudd College, Claremont, California

Publications

T. T. D. Nguyen and M. E. Helgeson. "Structure formation and gel elasticity in thermoresponsive colloidal gels formed via arrested phase separation," *In preparation.*

P. Padmanabhan, T. T. D. Nguyen, S. Fenton, M. E. Helgeson, and R. N. Zia. "Three distinct temporal regimes describe gelation following arrested phase separation of colloids," *In preparation.*

T. T. D. Nguyen, B. K. Ryu, S. Fenton, M. E. Helgeson, and R. N. Zia. "Toward a theoretical model for thermoresponsive colloids with short-ranged repulsion and long-ranged attractions," *In preparation.*

Presentations

T. T. D. Nguyen, A. Shetty, and M. E. Helgeson. “Large-scale structural rearrangement during yielding of heterogeneous colloidal gels revealed by rheo-microscopy,” 91st Society of Rheology Annual Meeting, October 20-24, 2019, Raleigh, NC.

T. T. D. Nguyen and M. E. Helgeson. “Using rheo-microscopy to directly correlate structural and mechanical aging in a thermoreversible colloidal gel,” 90th Society of Rheology Annual Meeting, October 14-18, 2018, Houston, TX.

B. K. Ryu, T. T. D. Nguyen, S. Fenton, M. E. Helgeson, and R. N. Zia. “A theoretical model for thermoresponsive nanoemulsions with polymer bridging interactions,” Poster at the 90th Society of Rheology Annual Meeting, October 14-18, 2018, Houston, TX.

M. E. Helgeson, T. T. D. Nguyen, P. Padmanabhan, and R. N. Zia. “Thermal processing of colloidal gels: Kinetics of quenching, coarsening and arrest,” 90th Society of Rheology Annual Meeting, October 14-18, 2018, Houston, TX.

T. T. D. Nguyen, J. T. Kim, and M. E. Helgeson. “Using thermal processing to control structure and rheology in thermoresponsive colloidal gels,” Poster at the 89th Society of Rheology Annual Meeting, October 8-12, 2017, Denver, CO.

T. T. D. Nguyen, J. T. Kim, and M. E. Helgeson. “Probing Quench-Dependent Gelation in Thermoresponsive Attractive Colloids,” AIChE 2016 National Meeting, November 13-18, 2016, San Francisco, CA.

Fields of Study

Studies in colloidal gel phase behavior, structure, and rheology with Professor Matthew E. Helgeson

Abstract

Phase Behavior, Processing, and Properties of Thermoresponsive Colloidal Gels

by

Tuan Terrence Do Nguyen

The ability to engineer macroscopic properties of colloidal gels through controlled processing of their microscopic substituents presents an opportunity to improve soft material technology in emergent fields such as additive manufacturing and biomaterial production. However, the fundamental underpinnings of colloidal gel formation and behavior are not comprehensively developed to a degree that would facilitate new material design. To build toward such an understanding of colloidal gels, in this dissertation we use a model thermoresponsive colloidal system to investigate (1) the formation of colloidal gels with respect their interparticle potential, phase behavior, and gel arrest kinetics, and (2) the resultant properties of colloidal gels as observed through their structure, viscoelasticity, and yielding.

The system of interest to this work comprises nanoemulsion dispersions with interactions mediated by thermoresponsive polymers. To model the effective interdroplet attractions arising from thermoresponsive behavior, we employ a hard sphere two-Yukawa interaction potential and determine model parameters from experimental scattering measurements. The interaction potential is subsequently used to make mean field predictions of the effective pseudo-one component colloidal phase behavior by means of variational perturbation methods, which are found to agree with measurements from sedimented phase separating gels as well as comparable coarse-grained molecular dynamics simulations. These results are noteworthy because they provide evidence that near-equilibrium behavior can still be recovered underneath the non-equilibrium glassy arrest line.

Additionally, we report qualitatively distinct gelation kinetics between colloidal gels formed at volume fractions below and above the predicted spinodal boundary. To explain gelation kinetics inside the phase coexistence region, we use rheo-microscopy which enables simultaneous characterization of gel linear viscoelasticity and microstructure. Through this characterization, we map out an isothermal transformation diagram to identify the sequential transitions that occur en route to prolonged arrest for varying thermal quenches. From rheological analysis of linear elasticity, we find that conventional nondimensionalization proves insufficient to collapse the quench dependence of gel elasticity, demonstrating a need for further investigation into the appropriate length and energy scales for scaling colloidal gel rheology. From imaging analysis of gel structuration, we find that late-stage coarsening rates exhibit a sigmoidal quench dependence akin to the effective interdroplet attraction strength, which can be predicted from a simple mean-field description of sub-critical viscoelastic phase separation.

Finally, we describe novel experimental techniques and metrics to evaluate colloidal gel structure during the process of yielding during large amplitude oscillatory shear deformation. Combining intracycle and intercycle analyses of microstructure and rheology reveals a three-stage process of network rupture, softening, and alignment that the yielding gel undergoes. Establishing this methodology provides a robust experimental platform for forthcoming studies into the direct influence of gelation and shearing conditions on the complex yielding process.

Contents

List of Figures

List of Tables

Chapter 1

Introduction

1.1 Motivation

This dissertation investigates colloidal gels, a class of materials wherein "colloid" describes a variety of everyday materials such as milk, foams, paints, and inks. Etymologically, the term "colloid" comes from a description by German biochemist Wolfgang Ostwald regarding the "glue-like" behavior observed in collections of these particles. [1] Appropriately, the persistent scientific motivation in studying colloidal systems – including the thermoresponsive colloidal gel central to this dissertation – endeavors to understand the origins and consequences of the "glue-like" interparticle interactions as they manifest in the system.

The latter term of this material class – "gel" – is also used to describe a variety of qualitatively different soft materials. The consensus view is that gels are continuous, solid-like networks of polymers or colloids that span the volume in a material system. Moreover, gels typically exhibit disordered, mesoscopic structures as well as a yield stress i.e., the propensity to flow upon the application of a sufficiently large yet finite force. [2] In its totality, however, this broad definition overlooks some key equilibrium and non-equilibrium features of colloidal gels that are present throughout their lifetime. To provide a more complete definition of colloidal gels, we address the relevant interaction, formation, and kinetic factors in the following section.

From a scientific perspective, research into colloidal systems allow us to better understand a wide range of phenomena observed in natural environments. Often idealized as "superatoms", colloidal studies provide insight into phase behavior and structure on length scales ranging from the atomic to the protein level. [3] Protein self-assembly, then, becomes better understood and manipulated as a result of colloidal gel studies. [4] Even complex biological features such as β-keratin nanostructures on bird feathers are hypothesized to follow physical processes that reflect underlying protein phase behavior. [5]

From a materials engineering perspective, research advances in colloidal systems are integral to the continued development of familiar consumer products as described at the onset of this section, as well as to the nascent development of emerging technologies that include additive manufacturing resins, biocompatible polymer-based materials, electrochemical energy storage, and plant-based meat alternatives. [6–9] By treating colloidal particles as tunable building blocks for hierarchical structures that can be orders of magnitudes larger than their substituents, there is an endless horizon of material applications that can be realized through rational colloidal design.

1.2 Colloidal gels

1.2.1 Colloidal interactions

Colloidal suspensions are formed when solid or fluid matter is dispersed in a surrounding, immiscible medium. Unlike molecular solutes, which comprise particles of a size similar to their solvent, colloidal particles are typically much larger than the constituents of their surrounding medium. [10] Examples can be found both in natural [11] and synthetic [12] systems as alluded to in the previous section.

The often-invoked analogy between colloids and atoms contends that a thermodynamic treatment of colloidal suspensions is comparable to atomic systems, and so the elementary ingredient of gel formation consists of the colloidal interactions. [13] Whereas in atomic systems a Lennard-Jones potential is often sufficient, in colloidal systems the unique features of the colloids, colloidal surfaces, and solvent can give rise to many different functional forms of the interaction potential.

To highlight one notable form, the Derjaguin-Landau-Verwey-Overbeek (DLVO) potential captures the integrated attractive component due to fluctuating atomic dipoles in concert with a repulsive component quantifying the electrostatic double layer. [14] Despite its ubiquity, however, additional interactions not described by DLVO theory have been observed to arise e.g. due to hydrophobic surface interactions, non-adsorbing polymer depletion attractions, and adsorbing polymer bridging attractions. [15–17]

The existence of attractions between colloidal particles is critical to gel formation. Put more simply, under appropriate conditions the colloids must stick together to form a persistent network of interparticle "bonds" that comprises the emergent gel.[1] For attrac-

---

[1] In purely repulsive systems, sufficiently high particle volume fractions (on the order of 56%) can result in measurable mechanical structure, but the physics associated with such repulsive glasses is qualitatively different from behavior in systems with attractions. [18–22] Notwithstanding, attractive systems exhibit a similarly classified attractive glass state in densely packed systems.

tive systems, an easily definable feature of a given potential is its interaction strength minimum, U_{min}, typically occurring at or near hard contact between two particles. Additionally, as will be discussed in depth in Chapter 3, the second virial coefficient B_2 offers another reduced parameter with which to describe interaction potentials of qualitatively different functional forms. [23] These measures provide an order parameter coordinate along which we can systematically consider variations in effective "bond" strength between colloids and thus rationalize the resultant gel formation that occurs.

1.2.2 Gel formation theory

Gel formation can be fundamentally described by considering the two rate processes that lead to assembly in an attractive colloidal suspension. First, we must assume that the forward reaction of two particles attracting to form an effective bond (agnostic of the underlying mechanism) is faster than the backward reaction of that bond being broken and the particles separating. These conditions ensure that gel formation is progressing towards full network formation and not ephemeral network dissipation.

The first relevant rate is the frequency with which particles successfully form bonds, which should be set in part by the strength of these bonds as well as by the availability of other particles to form such bonds. The second relevant rate is the frequency with which particles encounter one another due to random Brownian motion, set by the particle diffusivity in its surrounding medium. Comparing these rates, we establish a dimensionless group describing diffusion-reaction gelation kinetics, generally defined as a Damköhler number, Da:

$$\mathrm{Da} \equiv \frac{\text{reaction rate}}{\text{diffusion rate}} = \frac{k_{\text{eff}} a^2}{D_{\text{eff}}} \tag{1.1}$$

where k_{eff} is the effective bond formation rate constant, a is the particle radius, and D_{eff} is the effective particle diffusivity that accounts for the hydrodynamics of the particle in solution. [24]

The predominant theories for gel formation can be addressed by evaluating the two limiting regimes of the above Damköhler number. For Da $\ll 1$, gels are formed via reaction-limited cluster aggregation (RLCA) because colloids will diffuse toward each other frequently but will not always react to aggregate when they do. For Da $\gg 1$, gels are formed via diffusion-limited cluster aggregation (DLCA) because colloids will not diffuse toward each other frequently but will easily react to aggregate once they do. Experiments with low volume fraction colloidal suspensions support the existence of these two pathways. [25, 26]

One consequence of this gel formation dichotomy is observed in the cluster dimensionality, which is captured by a non-integer fractal dimension d_f. The number of particles in an aggregate cluster, N_{agg}, will scale with the cluster radius R_{agg} as $N_{agg} \propto (R_{agg}/a)^{d_f}$. Thus, the qualitatively distinct aggregation mechanisms give rise to quantitatively distinct scaling of the measurable cluster radii, with DLCA gels typically exhibiting a fractal dimension $d_f \sim 1.78$ and RLCA gels typically exhibiting a fractal dimension $d_f \sim 2.1$. [27] In the same vein, scaling relationships related to the fractal dimension have been developed and reported for viscoelastic moduli and yield strain. [28]

1.2.3 Limitations of gel formation theory

While the prior reaction-diffusion description is a straightforward way to evaluate two limiting cases of gel formation, the presence of thermodynamic and dynamic transitions frequently complicates the interpretation of colloidal gel structure property relationships.

Due to equilibrium thermodynamics, regions of colloidal phase instability are known to exist in certain regions of the colloidal phase diagram. [3, 16] This is a predictable consequence of the underlying colloidal interaction potentials in keeping with the colloid as atom analogy. When a system enters a region of phase instability, there exists an unfavorably high free energy penalty due to the concentration fluctuations between the two stable phases, reflecting the unstable, negative concavity of the Helmholtz free energy function. [13] Consequently, an unstable colloidal system will evolve toward thermodynamic equilibrium through the process of spinodal decomposition.[2] The earliest kinetic description of spinodal decomposition was provided via the Cahn-Hilliard model, which allows for a quantitative prediction of the kinetic processes by which spinodal decomposition proceeds. [29] Subsequent to its successes in describing purely diffusive phase separation dynamics, we acknowledge now that the Cahn-Hilliard model ignores both dynamic arrest and viscoelastic contributions arising from a network structure in one or both of the individual phases. Theoretical efforts to extend the Cahn-Hilliard model to viscoelastic systems have resulted in a more general model of phase separation that accounts for asymmetries in the viscosity or elasticity of the separating phases. [30]

As an alternative mechanism of gelation, colloidal gels can undergo an attractive glass transition at sufficiently high volume fraction. In this dynamic arrest mechanism, colloidal clusters experience a limited mobility due to caging effects. [31] Similar to supercooled liquids, the characteristic caged particle movement of glassy arrest can be described with a β-relaxation process, and the movement of larger domains with an α-relaxation process. [32] An early framework for understanding attractive glasses is mode coupling theory (MCT), which described the time evolution of density autocorrelation functions. It is a first-principles theory for glassy liquids that only requires knowledge of the liquid structure factor. [33] Although MCT does not provide direct predictions for the boundaries of gelation, it provides a rational understanding for viscoelastic dynamics in the resultant arrested gel.

---

[2] Alternatively, a *metastable* region of the free energy function should phase separate via nucleation and growth.

Considering both spinodal decomposition and glassy arrest, Medina-Noyola and coworkers have extended Onsager's theory of thermal fluctuations to non-stationary processes and are ultimately able to model arrested spinodal decomposition. Presented as a non-equilibrium self-consistent generalized Langevin equation (NE-SCGLE), the analysis broadly predicts how a colloidal system will evolve in response to thermal and mechanical processing. The time evolution of structure in NE-SCGLE is determined by the mean concentration profile and its covariance. What results from NE-SCGLE is a set of numerical predictions for the attractive glass arrest line within the two-phase region for a hard sphere plus attractive potential undergoing an instantaneous thermal quench, illustrated in Figure 1.1 as the dashed red line. The glassy arrest is identified by a liquid-glass dynamic arrest line, delineated by whether the equilibrium localization length diverges (reflecting ergodicity) or remains finite (reflecting non-ergodic arrest). [34] The theoretical results qualitatively compare with the colloidal behavior expected, identifying an intersection of the glass transition with the equilibrium coexistence line along its dense branch. In addition, results from NE-SCGLE theory find that the equilibrium phase coexistence line is "dynamically irrelevant" below the liquid-glass arrest transition. [34, 35]

Experimental approaches in characterizing arrested spinodal decomposition have used depletion attraction systems, with evidence showing that MCT is consistent with the observed dynamics. [36] For thermoresponsive nanoemulsions, the gelation mechanisms have been ascribed to proceed by either homogeneous percolation (i.e., via RLCA or DLCA) or arrested spinodal decomposition, depending on the volume fraction [37]. However, what remains unclear is whether spinodal decomposition is a necessary condition for gelation to occur. Additionally, no direct comparison of thermoresponsive nanoemulsions with MCT nor NE-SCGLE has been made.

To summarize, the states that are accessible due to both equilibrium and non-equilibrium transitions can be described with the picture in Figure 1.1. These include phase coexistence regions as indicated by a binodal and spinodal, as well as dynamic transitions such as percolation and attractive glass arrest. [38, 39]

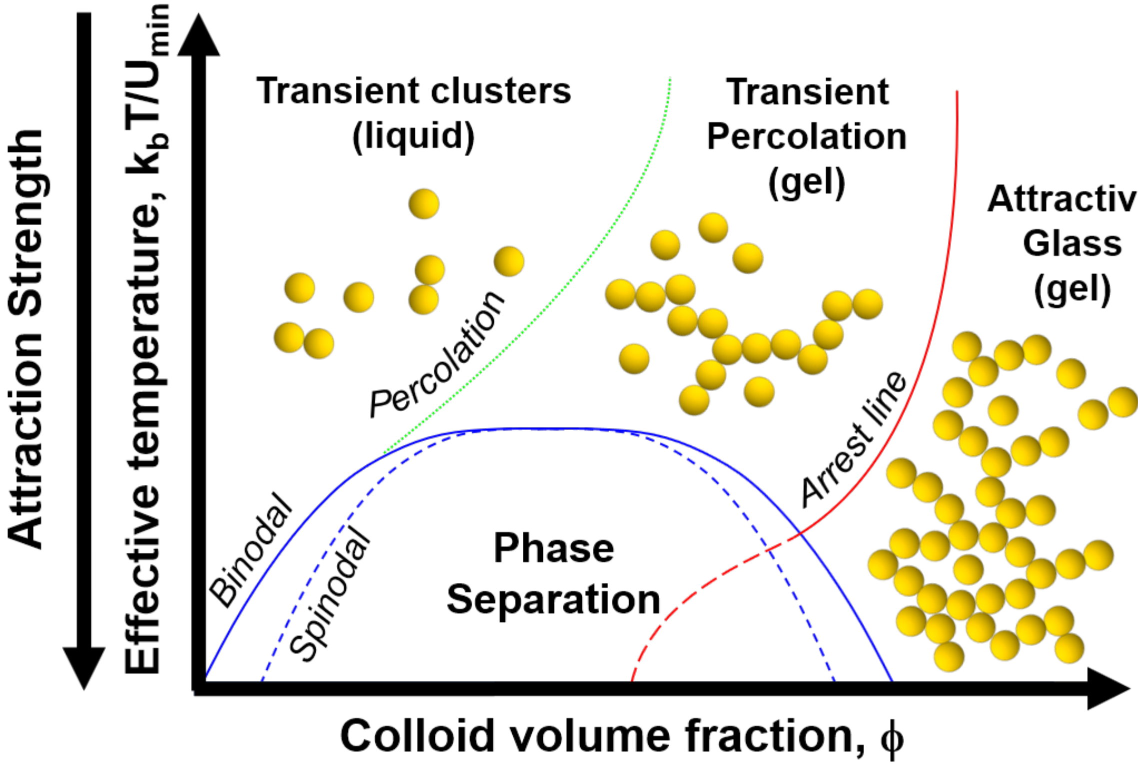

Figure 1.1: Schematic of an attractive colloidal phase diagram. In the region of weak attraction and low packing fraction, the system behaves as a continuous fluid with transient clusters. As the packing fraction is increased past the percolation line, transient percolated networks can form. At sufficiently high volume fractions the system forms an attractive glass. As the attraction strength is increased into the phase envelope, the spinodal instability leads to a phase separated system with colloid rich and colloid poor domains with composition determined by the binodal line. For sufficiently deep quenches, phase separation is arrested by the attractive glass line, which continues into the two-phase region. In this overlap region, phase separation becomes arrested in the dense phase.

1.2.4 Structural and mechanical properties

The transition from fluid colloidal suspension to viscoelastic colloidal gel is associated with significant mechanical and structural changes to the material. Notably, the viscosity diverges, and a yield stress emerges as gelation proceeds. [28] Additionally, the DLCA/RLCA gelation theories proscribe scaling arguments of the elastic modulus, G', and yield stress, σ_y. [27] These scaling relations take the form of $G' \propto \phi^x$ for an exponent x that is a function of the fractal dimension, where ϕ is the particle volume fraction. [15]

By considering the bond energy per unit area between colloids, Russel et al. developed scaling theories to relate the shape of the interparticle attraction to the macroscopically observed yield stress and gel elastic modulus for weakly attractive colloids. [10]

$$G' \propto \frac{\phi^x}{a}\left(\frac{d^2U}{dr^2}\right)_{\max} \tag{1.2}$$

where x is an exponent related to the distribution of bonds taking the value $x = 2$ for randomly distributed bonds, and $U(r)$ is the interparticle potential and the max subscript denotes the value of the second derivative at the attraction well minimum. Figure 1.2 illustrates this characteristic feature of a given interaction potential.

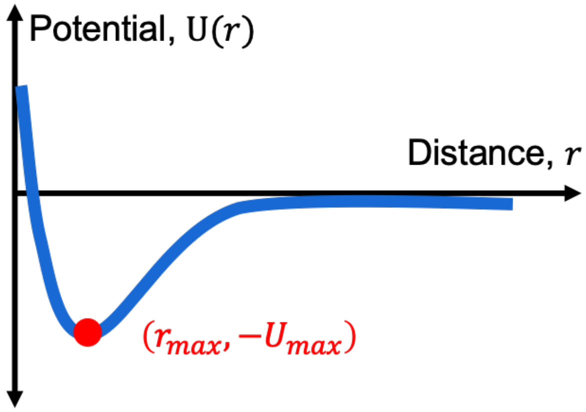

Figure 1.2: Interaction minimum used in elastic scaling theory. The second derivative of the interaction potential, $U(r)$, is calculated at the radial location of the interaction minimum in red.

The characteristics of colloidal gel network structure prior to and during yielding are important to understanding mechanical behavior. Namely, whereas homogeneous colloidal gels comprise a single network structure, heterogeneous gels exhibit hierarchical, nonuniform structure. In terms of yielding, homogeneous yielding occurs across a single yield point when measuring viscoelastic moduli as a function of strain amplitude, whereas heterogeneous yielding exhibits two or more characteristic points reflecting multiscale network rearrangement. Homogeneous colloidal gels have been shown to follow a heterogeneous process. [40, 41] Furthermore, simulations have identified the stress localization pathways that lead to network breakage, stiffening, and ultimate yielding. [42] However, qualitatively different yielding behavior has been reported for heterogeneous gels, with simulations of reversible colloidal gels finding re-entrant gel behavior during start-up shear [43], and experimental observations of heterogeneous gels reporting large-scale structural rearrangement during yielding from large amplitude oscillatory shear. [37, 44]

1.2.5 Open questions

In light of the extensive progress that has been made to enhance our understanding of colloidal gel behavior, questions around the gelation transition still remain. To begin, the intersection of the equilibrium phase boundary and glass arrest line (as seen in Figure 1.1) is not sufficiently characterized. At its root, the issue arises from the competition between equilibrium thermodynamics which sets the phase boundary and arrest kinetics which sets a dynamical transition. Experimental studies into short-ranged attractions have definitively shown that phase separation can indeed drive gelation irrespective of percolation. [16] But does the equilibrium colloidal phase boundary still retain physical meaning below the arrest line, or does it lose relevance due to the dominant glassy arrest process? Some experimental results for a model protein system as well as theoretical work based on NE-SCGLE support the latter claim, but the matter is far from resolved. [34, 45]

An additional question arises within the realm of gelation kinetics. By what sequence of events does colloidal gelation proceed, in particular in situations involving the competition of phase instability and glassy arrest? Because of the nature of the interactions studied previously, dynamical studies have been limited in scope and have not successfully resolved the full extent of structural formation and growth throughout the life of a nascent and aging colloidal gel. Rather, many colloidal gel studies have focused on the resultant gel structure and mechanics after the deeply arrested state has been reached. A study by Hsiao and coworkers has identified clear differences in linear viscoelastic response for varying quench kinetics, but a deeper understanding of the relationship between rheology and structure is needed. [46]

Finally, questions regarding the structure and yielding of colloidal gels have emerged as a result of studies into material performance. With current studies focusing on the complex yielding descriptions in homogeneous colloidal gels, heterogeneous gels present an even less clear picture. Kim et al. proposed a sequence of hierarchical yielding based on scattering measurements, but direct structural observation of such a mechanism has not been reported. [44] Thus, an immediate question is whether or not this yielding hypothesis in heterogeneous gels is borne out in reality. Or even as a first step, can we resolve any manner of structural changes due to yielding at all? This priority of this question is predicated on the fact that direct experimental characterization of colloidal gels during yielding presents many technical challenges.

1.3 Model colloidal gel systems

To tackle the open questions that remain in improving our fundamental knowledge of colloidal gels, a number of model systems are available thanks to the synthetic advances made over the past several decades. Broadly, the characteristic features include interparticle attractions that can be directly and dynamically tuned, with optically resolvable gel structure and mechanically resolvable viscoelasticity. In what follows, we survey four prevalent classes of model colloidal gel systems that have been studied in contributions to the current body of knowledge and consider their advantages and disadvantages for the purposes of our explorations in this dissertation.

1.3.1 Depletion gels

The earliest theoretical basis for depletion gels was proffered by Asakura and Oosawa, lending to subsequent investigations which describe such gels to have an Asakura-Oosawa potential. [47] Physically, the mechanism of particle attraction originates from the inclusion of non-adsorbing polymer in the continuous phase. Because of excluded volume effects, the polymer cannot physically occupy the space between colloids separated by a distance shorter than the polymer's radius of gyration. Consequently, the relatively higher concentration of polymer outside of the small gap pushes particles together due to the resulting osmotic pressure difference.

Depletion gels are a model system due to the simple nature of the interactions. Phase behavior can thus be described quantitatively and compared effectively against molecular dynamics simulations employing the same potential form. [48–50] The coupling of experiment and simulation has led to critical discoveries about colloidal gel behavior in depletion systems, most notably that phase separation is a necessary condition for gelation, whereas percolation is insufficient. [16]

For continued inquiry into colloidal gel phenomena, however, depletion gels have their limitations. Because the origins of attractions are set by depletant polymer concentration, varying the attraction strength dynamically is not easily executed without disruptive mixing steps that may prematurely yield a nascent gel. Indeed, the fully formed gels with elastic moduli on the order of 0.1 Pa to 10 Pa become increasingly challenging to experimentally interrogate. [18, 51] Perhaps more fundamentally, it is also unclear whether features unique to depletion gels (e.g. having "bonds" that are frictionless under rotation) limit the generalizability of conclusions made from their study. Thus, depletion gels are not suited for kinetic studies into gel formation and processing.

1.3.2 Grafted silica nanoparticles

Grafted silica nanoparticles comprise hard silica cores with a thin, chemically grafted alkane brush. [52] The gelation undergone by such systems is rooted in a low temperature phase change of the surface brush layer in non-polar solvents, which leads to increased interdigitation with the solvent. [53] The interparticle potential for grafted silica has been modeled effectively as one of adhesive hard spheres, in which the attraction strength is nearly irreversible upon contact of the surface layers. The gelation observed in the system has been assessed within a state diagram that includes a thermodynamic coexistence region. [54] Notably, the mechanism of gelation has been ascribed to rigidity percolation by DLCA, with the experimental gel arrest line residing well above the region of phase instability. [55] In this way, the grafted silica system is unable to access the rich phase behavior, especially in systematic study of arrested phase separation processes known to occur in many gelling systems.

1.3.3 Thermoresponsive microgels

Thermoresponsive microgels operate on the basis of a lower critical solution temperature (LCST) which causes the polymer microgel particles to swell or contract across a polymer-dependent threshold temperature. Most common in this application is the poly(N-isopropylacrylamide) (PNIPAM) system, which swells drastically across a narrow temperature range around 32 °C. [56] The ability to trigger this transition with temperature has resulted in successful studies of colloidal gel phase behavior [57], as well as deeper studies into the glass transition for denser particle loadings. [58]

While the thermoresponsive nature of microgel attractions overcomes the latent limitations in depletion gels, similar to the grafted silica system the richness of the phase space is lacking. The gels formed from microgel systems are relatively homogeneous and devoid of hierarchical structure, and thus do not provide a material platform for studies into heterogeneous gel behavior.

1.3.4 Thermoresponsive nanoemulsions

Nanoemulsion systems that exhibit thermoresponsive behavior are a material development originating with Helgeson and coworkers. [59] Nanoemulsions — colloidal dispersions of nanoscale droplets — are formed via high energy methods and result in optically transparent solutions of suspended droplets. [60]

By including telechelic (i.e., bifunctional end-modified), water-soluble polymers in the continuous phase of an oil-in water nanoemulsion, the nanoemulsion exhibits a sharp increase in elastic behavior when subjected to an increase in temperature. Shown in Figure 1.3 is a typical viscoelastic response to an increase in temperature, as indicated by the storage and loss moduli measured in small amplitude oscillatory shear. The key thermal transition is demarcated as T_{gel}, where there is a crossover from viscous-dominant to elastic-dominant linear response. The attractive interactions have been shown to occur for a variety of polymer end functionalities and are attributed to the temperature induced solubility change of the hydrophobic end groups, resulting in bridging of polymers between droplets. [37, 59]

The structures formed during this reversible gelation process can be observed and

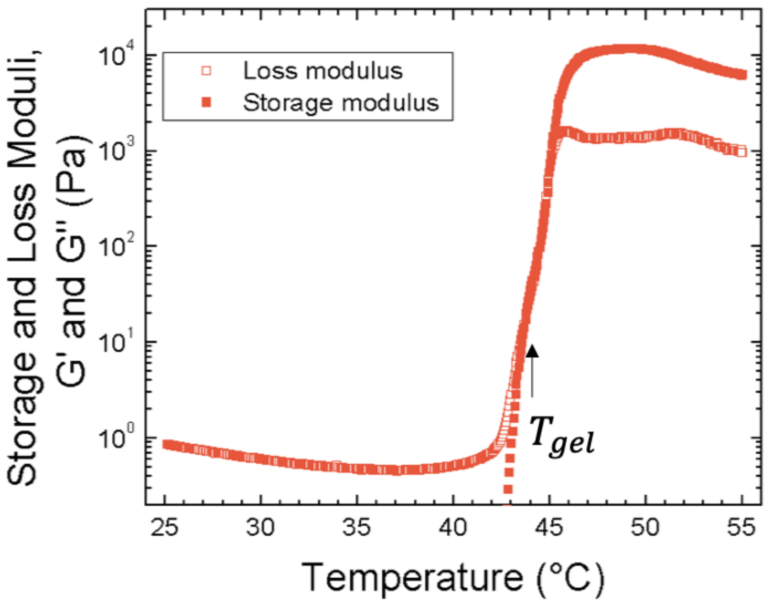

Figure 1.3: Representative thermorheology for a thermoresponsive nanoemulsion. The sample is subjected to a small amplitude oscillatory shear in the linear viscoelastic regime while the temperature is increased at a constant rate of $0.5\,^{\circ}\mathrm{C\,min}^{-1}$. As the temperature is increased, the storage modulus appears and grows to exceed the loss modulus, reflecting the formation of an elastic gel network. The details of formulation and features of linear viscoelastic rheology are discussed in more detail in Chapter 2.

analyzed through bright field microscopy. As shown in Figure 1.4, a heterogeneous, bicontinuous network develops as the temperature is increased over time and relaxes as the temperature is subsequently decreased back below T_{gel}.

Recalling the discussion of colloidal gels in Section 1.2.3, thermoresponsive nanoemulsions have been shown to exhibit both percolation and phase separation as a gelation mechanism. [37] Kim et al. studied yielding behavior of the thermoresponsive nanoemulsion gels under large amplitude deformations, finding that the yielding proceeds with decreasing domain size through three distinct regions. [44] Dynamics en route to gelation have also been described, showing that the arrest is driven by the interfacial coarsening of dense, cluster-like domains of droplets. [61] Thermal processing remains to be fully

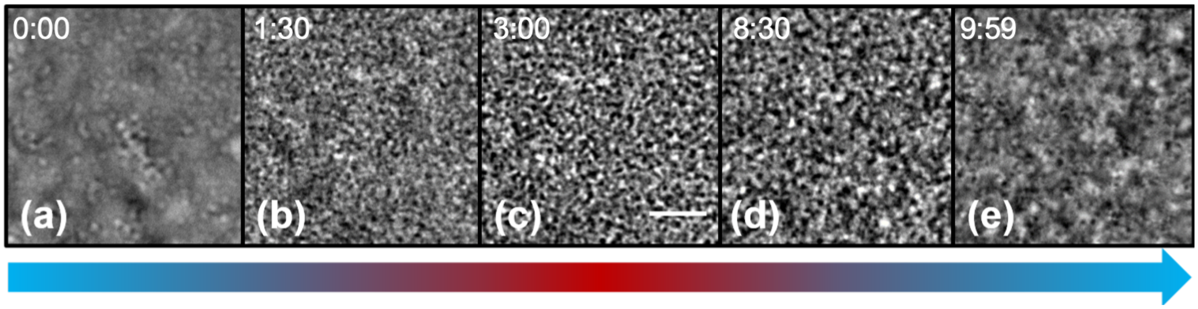

Figure 1.4: Sequence of bright field microscopy images demonstrating the qualitative microscopic features of thermoreversible gelation. From (a) a sample at room temperature, (b) controlled heating is applied to increase the temperature resulting in the initiation of phase separation as evident by the bicontinuous structure. Image (c) shows the fully developed and arrested gel at the final temperature of 45°C. At 6:30, the temperature is lowered down to room temperature, during which (d) the sample is cooling down and its structure relaxed until (e) it is returned to room temperature and the free solution begins to become clear again. With sufficient shear rejuvenation, it would revert to its appearance in (a). Scale bar indicates 20 μm.

understood, with recent work observing the existence quench dependent behavior. [46]

Overall, the thermoresponsive nanoemulsion system provides an ideal model system by way of its easily tuned thermoresponsive attractions, rich phase behavior, and heterogeneous structure. Additionally, the kinetics of coarsening are sufficiently slow to provide us with unprecedented access to interrogate the effects of processing en route to gel arrest.

1.4 Objectives and approach

The goal of this dissertation is to develop a coherent physical understanding of colloidal gelation by using a model thermoresponsive colloidal gel and studying both its equilibrium and non-equilibrium behavior. We evaluate the phase behavior, processing, and properties of a thermoresponsive nanoemulsion to achieve this goal. In Chapter 2 we detail the materials employed throughout our studies as well as provide abbreviated descriptions of the characterization techniques necessary for quantitative analysis. Once establishing the system and tools, in Chapter 3 we consider the theory and experimental approach by which colloidal interaction potentials are developed, connecting experimental scattering data to fundamental descriptions of the polymer bridging attraction. With an operative interaction potential, in Chapter 4 we use these interactions to develop mean-field predictions for equilibrium phase coexistence regions using a variational free energy technique. These phase envelope predictions are then compared to determinations of phase boundaries based on centrifugal separation experiments. Then we move onto kinetics in Chapter 5, where we investigate the sequential, non-equilibrium transitions leading up to, and resulting in, gel arrest. The sequence of transitions presents complications to a simpler equilibrium picture of gelation, but it allows us to develop a framework by which gel transformation processes can be delineated in terms of an isothermal transformation diagram. In Chapter 6 the formation of gel structure is examined more closely, and we develop scaling arguments to describe observable coarsening rates in late-stage arrest of spinodal decomposition. Furthermore, the relationship between plateau storage modulus and attraction strength is evaluated with respect to theoretical predictions for weakly attractive colloidal gels. In the penultimate Chapter 7, we lay out preliminary studies into more advanced experimental methods that are required to probe nonlinear yielding phenomena in colloidal gels, wherein signal synchronization intracycle analysis techniques are presented. Finally, Chapter 8 summarizes the key scientific contributions developed throughout the work and outlines recommendations and observations on future research efforts.

Bibliography

[1] P.-G. de Gennes, "Ultradivided matter," *Nature*, vol. 412, no. 6845, p. 385, 2001.

[2] A. D. McNaught, *Compendium of chemical terminology*, vol. 1669. Blackwell Science Oxford, 1997.

[3] W. C. Poon, "Phase separation, aggregation and gelation in colloid-polymer mixtures and related systems," *Current Opinion in Colloid & Interface Science*, vol. 3, no. 6, pp. 593–599, 1998.

[4] J. J. McManus, P. Charbonneau, E. Zaccarelli, and N. Asherie, "The physics of protein self-assembly," *Current opinion in colloid & interface science*, vol. 22, pp. 73–79, 2016.

[5] E. R. Dufresne, H. Noh, V. Saranathan, S. G. Mochrie, H. Cao, and R. O. Prum, "Self-assembly of amorphous biophotonic nanostructures by phase separation," *Soft Matter*, vol. 5, no. 9, pp. 1792–1795, 2009.

[6] J. E. Smay, J. Cesarano, and J. A. Lewis, "Colloidal inks for directed assembly of 3-d periodic structures," *Langmuir*, vol. 18, no. 14, pp. 5429–5437, 2002.

[7] S. D. Kimmins and N. R. Cameron, "Functional porous polymers by emulsion templating: recent advances," *Advanced Functional Materials*, vol. 21, no. 2, pp. 211–225, 2011.

[8] J. J. Richards, J. B. Hipp, J. K. Riley, N. J. Wagner, and P. D. Butler, "Clustering and percolation in suspensions of carbon black," *Langmuir*, vol. 33, no. 43, pp. 12260–12266, 2017.

[9] E. Dickinson, “Stabilising emulsion-based colloidal structures with mixed food ingredients,” *Journal of the Science of Food and Agriculture*, vol. 93, no. 4, pp. 710–721, 2013.

[10] W. B. Russel, D. A. Saville, and W. R. Schowalter, *Colloidal dispersions.* Cambridge New York: Cambridge University Press, 1989.

[11] R. Mezzenga, P. Schurtenberger, A. Burbidge, and M. Michel, “Understanding foods as soft materials,” *Nature materials*, vol. 4, no. 10, pp. 729–740, 2005.

[12] F. Leal-Calderon, V. Schmitt, and J. Bibette, *Emulsion science: basic principles.* Springer Science & Business Media, 2007.

[13] N. A. Verhaegh, D. Asnaghi, H. N. Lekkerkerker, M. Giglio, and L. Cipelletti, “Transient gelation by spinodal decomposition in colloid-polymer mixtures,” *Physica A: Statistical Mechanics and its Applications*, vol. 242, no. 1, pp. 104–118, 1997.

[14] J. N. Israelachvili, *Intermolecular and surface forces*, vol. 53. 2011.

[15] C. Rueb and C. Zukoski, “Viscoelastic properties of colloidal gels,” *Journal of Rheology*, vol. 41, no. 2, p. 197, 1998.

[16] P. J. Lu, E. Zaccarelli, F. Ciulla, A. B. Schofield, F. Sciortino, and D. a. Weitz, “Gelation of particles with short-range attraction,” *Nature*, vol. 453, pp. 499–503, May 2008.

[17] S. R. Bhatia and W. B. Russel, “End-Capped Associative Polymer Chains between Nanospheres: Attractions in Ideal Solutions,” *Macromolecules*, vol. 33, pp. 5713–5720, jul 2000.

[18] E. Zaccarelli, “Colloidal Gels: Equilibrium and Non-Equilibrium Routes,” *Journal of Physics: Condensed Matter*, vol. 19, p. 323101, aug 2007.

[19] K. Pham, G. Petekidis, D. Vlassopoulos, S. Egelhaaf, W. Poon, and P. Pusey, "Yielding behavior of repulsion-and attraction-dominated colloidal glasses," *Journal of Rheology*, vol. 52, no. 2, pp. 649–676, 2008.

[20] P. Pusey, "Colloidal glasses," *Journal of Physics: Condensed Matter*, vol. 20, no. 49, p. 494202, 2008.

[21] W. C. Poon, "Colloidal glasses," *MRS Bulletin*, vol. 29, no. 2, pp. 96–99, 2004.

[22] M. E. Helgeson, "Colloidal behavior of nanoemulsions: Interactions, structure and rheology," *Current Opinion in Colloid & Interface Science*, pp. –, 2016.

[23] M. G. Noro and D. Frenkel, "Extended corresponding-states behavior for particles with variable range attractions," *The Journal of Chemical Physics*, vol. 113, no. 8, pp. 2941–2944, 2000.

[24] L. G. Leal, *Advanced transport phenomena: fluid mechanics and convective transport processes.* Cambridge University Press, 2007.

[25] D. Weitz and M. Oliveria, "Fractal structures formed by kinetic aggregation of aqueous gold colloids," *Physical Review Letters*, vol. 52, no. 16, p. 1433, 1984.

[26] M. Lin, H. Lindsay, D. Weitz, R. Ball, R. Klein, and P. Meakin, "Universal reaction-limited colloid aggregation," *Physical review A*, vol. 41, no. 4, p. 2005, 1990.

[27] W.-H. Shih, W. Y. Shih, S.-I. Kim, J. Liu, and I. A. Aksay, "Scaling behavior of the elastic properties of colloidal gels," *Physical Review A*, vol. 42, no. 8, p. 4772, 1990.

[28] J. Mewis and N. J. Wagner, *Colloidal suspension rheology.* Cambridge New York: Cambridge University Press, 2012.

[29] J. E. Cahn and J. W. Hilliard, "Free Energy of a Nonuniform System. I. Interfacial Free Energy," *The Journal of Chemical Physics*, vol. 28, no. 2, pp. 258–267, 1958.

[30] H. Tanaka, "Viscoelastic phase separation," *Journal of Physics: Condensed Matter*, vol. 12, no. 15, p. R207, 2000.

[31] F. Sciortino, "Disordered materials: One liquid, two glasses," *Nature materials*, vol. 1, no. 3, pp. 145–146, 2002.

[32] W. Gotze and L. Sjogren, "Relaxation processes in supercooled liquids," *Reports on Progress in Physics*, vol. 55, pp. 241–376, mar 1992.

[33] P. Charbonneau and D. Reichman, "Mode-coupling theory," *J. Stat. Mech: Theory and Experiment*, vol. 05013, pp. 1–22, 2005.

[34] J. M. Olais-Govea, L. López-Flores, and M. Medina-Noyola, "Non-equilibrium theory of arrested spinodal decomposition," *The Journal of chemical physics*, vol. 143, no. 17, p. 174505, 2015.

[35] P. Ramírez-González and M. Medina-Noyola, "General nonequilibrium theory of colloid dynamics," *Physical Review E*, vol. 82, no. 6, p. 061503, 2010.

[36] S. Manley, H. Wyss, K. Miyazaki, J. Conrad, V. Trappe, L. Kaufman, D. Reichman, and D. Weitz, "Glasslike arrest in spinodal decomposition as a route to colloidal gelation," *Physical review letters*, vol. 95, no. 23, p. 238302, 2005.

[37] M. E. Helgeson, Y. Gao, S. E. Moran, J. Lee, M. Godfrin, A. Tripathi, A. Bose, and P. S. Doyle, "Homogeneous percolation versus arrested phase separation in attractively-driven nanoemulsion colloidal gels," *Soft matter*, vol. 10, no. 17, pp. 3122–3133, 2014.

[38] Y. Chiew and E. Glandt, "Percolation behaviour of permeable and of adhesive spheres," *Journal of Physics A: Mathematical and General*, vol. 16, no. 11, p. 2599, 1983.

[39] S. Netemeyer and E. D. Glandt, "Percolation behavior of the square-well fluid," *The Journal of chemical physics*, vol. 85, no. 10, pp. 6054–6059, 1986.

[40] T. Gibaud, D. Frelat, and S. Manneville, "Heterogeneous yielding dynamics in a colloidal gel," *Soft Matter*, vol. 6, no. 15, pp. 3482–3488, 2010.

[41] N. Koumakis and G. Petekidis, "Two step yielding in attractive colloids: transition from gels to attractive glasses," *Soft Matter*, vol. 7, no. 6, pp. 2456–2470, 2011.

[42] J. Colombo and E. Del Gado, "Stress localization, stiffening, and yielding in a model colloidal gel," *Journal of rheology*, vol. 58, no. 5, pp. 1089–1116, 2014.

[43] L. C. Johnson, B. J. Landrum, and R. N. Zia, "Yield of reversible colloidal gels during flow start-up: release from kinetic arrest," *Soft matter*, vol. 14, no. 24, pp. 5048–5068, 2018.

[44] J. Kim, D. Merger, M. Wilhelm, and M. E. Helgeson, "Microstructure and nonlinear signatures of yielding in a heterogeneous colloidal gel under large amplitude oscillatory shear," *Journal of Rheology (1978-present)*, vol. 58, no. 5, pp. 1359–1390, 2014.

[45] F. Cardinaux, T. Gibaud, A. Stradner, and P. Schurtenberger, "Interplay between Spinodal Decomposition and Glass Formation in Proteins Exhibiting Short-Range Attractions," *Physical Review Letters*, vol. 99, p. 118301, sep 2007.

[46] L. C. Hsiao and P. S. Doyle, "Celebrating soft matter's 10th anniversary: Sequential

phase transitions in thermoresponsive nanoemulsions," *Soft Matter*, vol. 11, no. 43, pp. 8426–8431, 2015.

[47] S. Asakura and F. Oosawa, "On interaction between two bodies immersed in a solution of macromolecules," *The Journal of Chemical Physics*, vol. 22, no. 7, pp. 1255–1256, 1954.

[48] H. Lekkerkerker, W.-K. Poon, P. Pusey, A. Stroobants, and P. . Warren, "Phase behaviour of colloid+ polymer mixtures," *EPL (Europhysics Letters)*, vol. 20, no. 6, p. 559, 1992.

[49] S. Ramakrishnan, M. Fuchs, K. S. Schweizer, and C. F. Zukoski, "Entropy driven phase transitions in colloid–polymer suspensions: Tests of depletion theories," *The Journal of chemical physics*, vol. 116, no. 5, pp. 2201–2212, 2002.

[50] J. C. Conrad, H. M. Wyss, V. Trappe, S. Manley, K. Miyazaki, L. J. Kaufman, a. B. Schofield, D. R. Reichman, and D. a. Weitz, "Arrested fluid-fluid phase separation in depletion systems: Implications of the characteristic length on gel formation and rheology," *Journal of Rheology*, vol. 54, no. 2, p. 421, 2010.

[51] A. Meller, T. Gisler, D. A. Weitz, and J. Stavans, "Viscoelasticity of depletion-induced gels in emulsion- polymer systems," *Langmuir*, vol. 15, no. 6, pp. 1918–1922, 1999.

[52] A. Van Helden, J. Jansen, and A. Vrij, "Preparation and characterization of spherical monodisperse silica dispersions in nonaqueous solvents," *Journal of Colloid and Interface Science*, vol. 81, no. 2, pp. 354–368, 1981.

[53] A. P. Eberle, N. J. Wagner, B. Akgun, and S. K. Satija, "Temperature-dependent

nanostructure of an end-tethered octadecane brush in tetradecane and nanoparticle phase behavior," *Langmuir*, vol. 26, no. 5, pp. 3003–3007, 2010.

[54] A. P. Eberle, N. J. Wagner, and R. Castañeda-Priego, "Dynamical arrest transition in nanoparticle dispersions with short-range interactions," *Physical review letters*, vol. 106, no. 10, p. 105704, 2011.

[55] A. P. Eberle, R. Castaneda-Priego, J. M. Kim, and N. J. Wagner, "Dynamical arrest, percolation, gelation, and glass formation in model nanoparticle dispersions with thermoreversible adhesive interactions," *Langmuir*, vol. 28, no. 3, pp. 1866–1878, 2012.

[56] H. G. Schild, "Poly (n-isopropylacrylamide): experiment, theory and application," *Progress in polymer science*, vol. 17, no. 2, pp. 163–249, 1992.

[57] J. Wu, B. Zhou, and Z. Hu, "Phase behavior of thermally responsive microgel colloids," *Physical review letters*, vol. 90, no. 4, p. 048304, 2003.

[58] R. Rivas-Barbosa, E. Lázaro-Lázaro, P. Mendoza-Méndez, T. Still, V. Piazza, P. E. Ramírez-González, M. Medina-Noyola, and M. Laurati, "Different routes into the glass state for soft thermo-sensitive colloids," *Soft matter*, vol. 14, no. 24, pp. 5008–5018, 2018.

[59] M. E. Helgeson, S. E. Moran, H. Z. An, and P. S. Doyle, "Mesoporous organohydrogels from thermogelling photocrosslinkable nanoemulsions," *Nature Materials*, vol. 11, pp. 344–352, February 2012.

[60] T. G. Mason, J. N. Wilking, K. Meleson, C. B. Chang, and S. M. Graves, "Nanoemulsions: formation, structure, and physical properties," *Journal of Physics: condensed matter*, vol. 18, no. 41, p. R635, 2006.

[61] Y. Gao, J. Kim, and M. E. Helgeson, “Microdynamics and arrest of coarsening during spinodal decomposition in thermoreversible colloidal gels,” *Soft Matter*, vol. 11, no. 32, pp. 6360–6370, 2015.

Chapter 2

Materials and methods

2.1 Nanoemulsion preparation

In general, thermoresponsive nanoemulsion formulation comprises four chemical components that are combined and processed to synthesize nanoscale droplets with thermoreversible gelation behavior. The four components include a dispersed phase typically comprised of an oil, and an aqueous continuous phase comprised of a surfactant and a water-soluble bridging polymer in water. Shown in Table 2.1 are the specific chemical components employed in the current thesis, although the thermoresponsive behavior studied here has been observed in a variety of other material systems. [1–4] The compositional state variables used for nanoemulsion synthesis include ϕ, the dispersed oil droplet volume fraction; P, the volume fraction of bridging polymer in the continuous phase; and C_s, the molar concentration of surfactant in the continuous phase. The remainder of the volume is occupied by water.

2.1.1 Synthesis

All chemicals listed in Table 2.1 were purchased from the Sigma-Aldrich Corporation and used without further purification. For studies using nuclear magnetic resonance or neutron scattering, deuterated water purchased from Cambridge Isotope Laboratories was used instead of deionized water.

Surfactant and polymer are first stirred at 350 rpm using the desired amounts dispensed into a beaker with deionized water. Then, silicone oil (polydimethylsiloxane, viscosity 5 cSt) is added dropwise with a burette into the continuous mixture over the course of two hours while stirred at 750 rpm. The resulting intermediate mixture comprises at crude, opaque emulsion with micron-scale oil droplets.

To reduce the droplet size distribution of the crude emulsion, the mixture is passed multiple times (N=16 passes) through a high-pressure homogenizer (Avestin EmulsiFlex-C5) at a homogenization pressure of 10 kpsi. Note that prior studies report a plateau in nanoemulsion droplet size as a function of repeated homogenization passes, with the plateau occurring past $N = 12$. [1] The resultant nanoemulsion is optically transparent and is stored in a refrigerator at 5 °C in polyethylene tubes prior to further use. Dynamic light scattering, explained in more detail later in the next section, is used to characterize nanoemulsion droplet size distribution.

Component	**Density** (g/mL)	**Function**
Deionized water	1.00	Continuous phase
Silicone oil	0.91	Dispersed phase
Sodium Dodecyl Sulfate (SDS)	1.01	Surfactant
Poly(ethylene glycol) diacrylate (PEGDA)	1.12	Thermoresponsive bridging polymer

Table 2.1: Summary description of chemicals used for thermoresponsive nanoemulsion formulation, including their respective functions in the resultant material.

2.2 Dynamic light scattering

Dynamic light scattering (DLS) is a characterization technique that relates the measurable temporal fluctuations in scattered laser light intensity to the diffusivity of scattering objects in a near-transparent sample, allowing for measurement of particle size distributions. [5] Operationally, a coherent laser light beam of wavelength λ is passed through a dilute sample of suspended scattering objects with refractive index n. After passing through the sample, the scattered light is collected at a fixed detector angle θ corresponding to a probing wavevector $q = \dfrac{4\pi n}{\lambda} \sin\left(\dfrac{\theta}{2}\right)$. The governing equation for DLS measurements is given by the Siegert relation between the intensity autocorrelation function, $g^2(q,\tau)$, and the electric field correlation function, $g^1(q,\tau)$, which assumes that the scattered field can be described as a Gaussian random variable. [6]

$$g^2(q,\tau) = 1 + c\left[g^1(q,\tau)\right]^2 \tag{2.1}$$

where τ is the delay time, and c is a constant of order unity that captures the physical properties of the laser beam path. The intensity autocorrelation function is measured by a self-correlation of the collected intensities over time, $I(t)$

$$g^2(\tau) = \frac{\langle I(t)I(t+\tau)\rangle}{\langle I(t)\rangle^2} \tag{2.2}$$

Figure 2.1 qualitatively illustrates the intensity and autocorrelation function signals as they vary with time and delay time, respectively. In an ergodic colloidal system undergoing Brownian motion, the assumed functional form of $g^1(q,\tau)$ is one of exponential decay such that

$$g^1(q,\tau) = \exp\left(-Dq^2\tau\right) \tag{2.3}$$

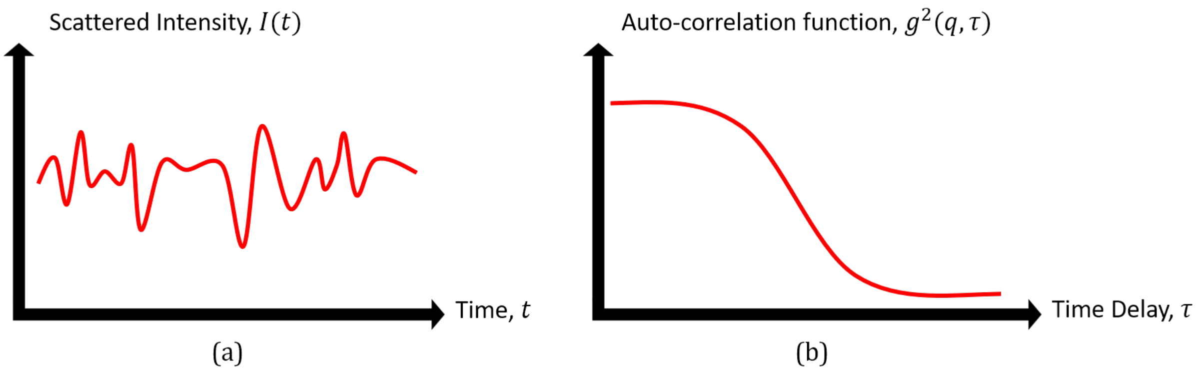

Figure 2.1: (a) Illustration of the fluctuations in scattered laser light intensity $I(t)$ as a function of sampling time. Using Equation (2.2), the signal is digitally correlated with itself to develop the autocorrelation function $g^2(\tau)$ in (b), which is plotted as a function of delay time τ. In the limit of short delay times, the intensities show complete correlation, i.e. $g^2(\tau) \to 1$, whereas the signal becomes uncorrelated at long delay times, i.e. $g^2(\tau) \to 0$.

where D is the Stokes-Einstein diffusivity. The hydrodynamic radius a of a particle is thus related using the expression for Stokes-Einstein assuming no slip at the droplet boundary,

$$D = \frac{k_B T}{6\pi\eta a} \tag{2.4}$$

where k_B is Boltzmann's constant, T is the absolute temperature, and η is the bulk solvent viscosity. The no slip assumption is valid if there are not significant internal flows inside the droplet.

In the nanoemulsion system, droplet size and polydispersity were measured with a Brookhaven BI 200SM light scattering apparatus upon dilution of the sample to a droplet volume fraction of $\phi = 0.01$ at fixed polymer volume fraction. Measurements were taken with a 532 nm green laser at a scattering angle of $\theta = 90°$. Dilution is not expected to change the size of the droplets [7], and measured samples are optically transparent to the eye. Polydispersity (PDI) is determined from a cumulant analysis of the autocorrelation function as provided by instrument software, which essentially expands the exponential decay form of the correlation function into a power series. The second-order cumulant is used to determine the polydispersity, which is related to the standard error (σ) of particle size as PDI $= \left(\frac{\sigma}{2a}\right)^2$. [5]

2.3 Linear viscoelastic rheology

Linear viscoelastic (LVE) rheology is a mechanical spectroscopy technique that can be probed using a variety of rheometric flows. [8] Here we focus on using an inputted sinusoidal oscillation with angular frequency ω and strain amplitude γ_0, then measuring the output stress $\sigma(t)$ in the material. [9] For sufficiently small strain amplitudes that do not perturb the structure of the sample, the output stress can be described by

$$\sigma(t) = \gamma_0 \left[G'(\omega)\ \sin(\omega t) + G''(\omega)\ \cos(\omega t)\right] \tag{2.5}$$

where G' is the storage, or elastic, modulus and G'' is the loss, or viscous, modulus. To describe the relationship between the two responses, the phase angle δ is another parameter that is useful to calculate, defined as $\delta = \tan^{-1}\left(\frac{G''}{G'}\right)$. To consider the limiting cases of this measurement, an ideal Hookean solid would exhibit a purely elastic response such that $G'' = 0$ and $\delta = 0$, whereas an ideal Newtonian fluid would exhibit a purely viscous response such that $G' = 0$ and $\delta = \frac{\pi}{2}$.

In measurements of real viscoelastic fluids, we can also qualitatively observe either “liquid-like” or “solid-like” frequency responses, as depicted in Figure 2.2. [9] In a “liquid-like” sample, the moduli will scale with frequency as $G' \propto \omega^2$ and $G'' \propto \omega$ at sufficiently small frequencies relative to the longest viscoelastic time scale of the material. In a “solid-like” sample, the moduli will be nearly frequency independent with $G' \gg G''$. The probing configuration employed for LVE measurements is limited to geometries that approximate rheometric flows, which includes upper cone/lower plate, upper plate/lower

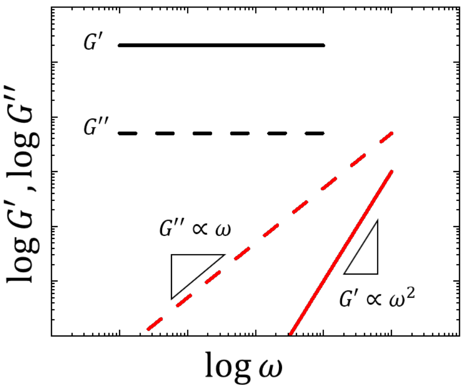

Figure 2.2: Qualitative plot illustrating the limiting low-frequency behavior for solid–like (black) or liquid-like (red) frequency response behavior under LVE rheological measurements.

plate, and concentric cylinder geometries. [8] In a majority of the work developed here, we focus on a stainless steel upper cone/lower plate (also called cone/plate) geometry with diameter 60 mm and angle 2° attached to a stress-controlled rheometer (AR-G2, TA Instruments), with a lower Peltier plate to enable temperature control. Additionally, a solvent trap filled with deionized water is used to maintain a humid environment around the sample and minimize evaporation during aging experiments. In Chapters 6 and 7, a plate/plate configuration is used to better facilitate imaging through glass geometries via rheo-microscopy, to be described in some more detail in the subsequent section.

A related technique to LVE that ventures into the nonlinear limit but still imposes a sinusoidal input is large amplitude oscillatory shear (LAOS). In this limit the input oscillations materially change the system's dynamics and structure and therefore mechanical properties. In general, this results in higher order terms needed to describe the response, which has been borne out through extensive work into various LAOS analysis techniques. [10, 11] Details associated with interpreting and analyzing LAOS data as obtained for the current colloidal gel system are described in more detail in Chapter 7.

In the context of the thermoresponsive nanoemulsion system, we use LVE rheology to track the transition from viscous fluid to viscoelastic solid by measuring both $G'(t)$ and $G''(t)$. Figure 1.3 illustrates a thermo-rheological experiment in which the temperature is linearly increased and the LVE moduli are measured as a function of temperature at constant angular velocity and constant strain amplitude in the LVE region. The LVE region is determined by conducting a strain amplitude sweep (i.e. varying γ_0 at constant ω) and identifying the maximum γ_0 below which G' and G'' plateau. Typical LVE strain amplitudes for colloidal gels are on the order of $\gamma_0 \sim O(0.1\%)$. [1, 12, 13]

2.4 Rheo-microscopy

Rheo-microscopy combines the mechanical spectroscopy of rheometry with the structural visualization of optical microscopy. This combination is enabled by advances in rheometer design, specifically employing a transparent glass plate upper geometry (diameter 43 mm, thickness 4.05 mm) and transparent glass plate lower geometry (thickness 4.17 mm) in line with the rheometer motor. Figure 2.3 schematically depicts the imaging platform, wherein white light is transmitted from above the upper glass plate, through the sample volume, and imaged by a camera (Lumenera Lm165) on a translatable stage from below. The platform design is validated through work from the Anton Paar Company and implemented on a stress-controlled rheometer (MCR702, Anton Paar). [14] Temperature control is enabled through Peltier heating around the circumference of the lower glass plate, with calibrations performed to correlate temperatures between center and edge of the glass plate.

With the unique combination of temperature, motor, and imaging control, experiments were performed by setting the desired temperature protocol, employing either LVE or nonlinear straining conditions, and simultaneously acquiring bright field microscopy

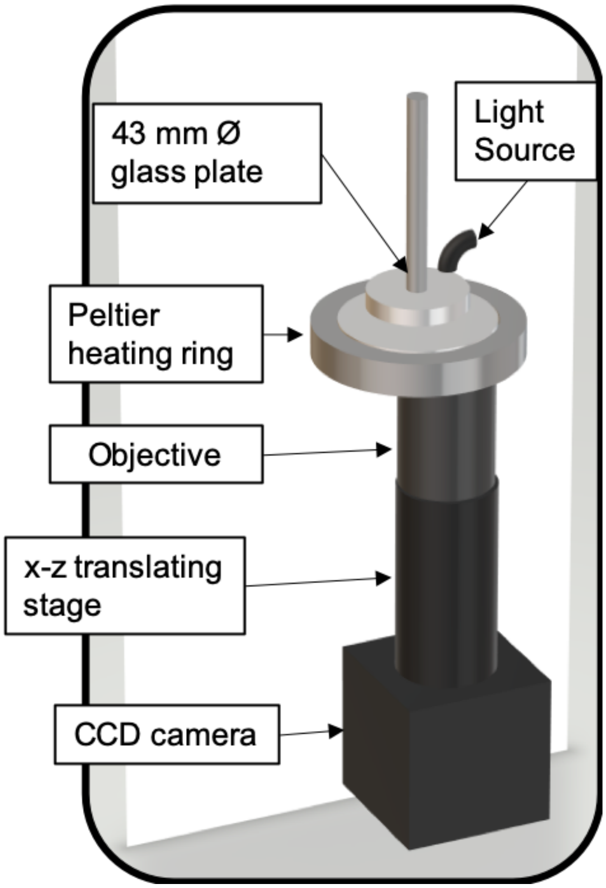

Figure 2.3: Schematic of platform for rheo-microscopy imaging and rheometry.

images that could be synchronized with rheological data points.

2.5 Nuclear magnetic resonance spectroscopy

Nuclear magnetic resonance (NMR) spectroscopy is a non-destructive chemical analysis technique that interrogates the unique nuclear environments in a sample using an applied magnetic field pulse. The different chemical environments of nuclei result in varying relaxation times as the induced magnetic moment of the sample processes back to its equilibrium state. From Fourier analysis of the decay response, a frequency response can be translated to a chemical shift spectrum using the resonance frequency of a reference sample. From a chemical shift spectrum, the integrated area under the curve is proportional to the number of nuclei being interrogated. [15] Because we can extract quantitative information about the relative contributions of proton environments (as tabulated in chemical shift tables), NMR can be used to quantify species in non-overlapping regions of chemical shift.

To obtain the solution-state proton NMR spectra developed in Chapter 5, we used a Bruker AVANCE 500 MHz spectrometer operating at a ^{1}H frequency of 500.1 MHz. Samples were diluted in deuterated water, which is not NMR active, to reduce the viscosity of highly viscous samples for filling narrow glass NMR tubes while still preserving the mole ratio of oil to polymer. Further details of sample preparation and NMR usage are detailed in Chapter 4.

2.6 Small angle neutron scattering

Small angle neutron scattering (SANS) is a structural characterization technique that uses neutrons (rather than laser light, as is the case in light scattering like DLS) to probe the nanometer- to micrometer-scale structures in a sample. Neutrons serve as a unique probe for interrogating structure of condensed materials because they interact with the nuclei of the sample, rather than the electron clouds as is the case for analogous light or x-ray scattering techniques. [16] For the colloidal gels we aim to study, this probing technique critically avoids disruptive sample heating or degradation due to high energy light or x-ray fluxes.

The quantitative information extracted from a scattering experiment is obtained by considering the expression for the total scattering intensity, $I(q)$. From the most general equation relating the scattering cross sections to scattering intensity, we make the simplifying assumptions that: (1) scattering within an object is independent of other objects and (2) object size and orientation are independent of position. [17] The resulting expression for the scattering intensity is then

$$I(q) = \phi V \left(\Delta\rho\right)^2 P(q)S(q) + I_b \tag{2.6}$$

where q is the probing wavevector which is a function of the neutron wavelength and scattering angle, ϕ is the volume fraction of scattering objects, V is the average volume of a scattering object, $\Delta\rho$ is the difference in scattering length density between the scattering objects and the surrounding medium, $P(q)$ is the form factor that accounts for intraparticle scattering correlations (including from the shape and polydispersity of the objects), $S(q)$ is the structure factor that accounts for the interparticle scattering correlations (including from effective interactions between objects), and I_b is the incoherent background scattering. [17] Descriptions of the relevant form factors and structure factors are provided in greater detail in Chapter 3, where the experimental SANS data is reduced and analyzed for varying forms of interaction potential. SANS measurements were conducted at the NIST Center for Neutron Research (NCNR) in Gaithersburg, Maryland, using the NGB7 30 m instrument which is capable of probing length scales from 1 nm to 500 nm. [17] Data reduction and processing were carried out using freely-available NCNR software packages in IGOR Pro (WaveMetrics, Inc.).

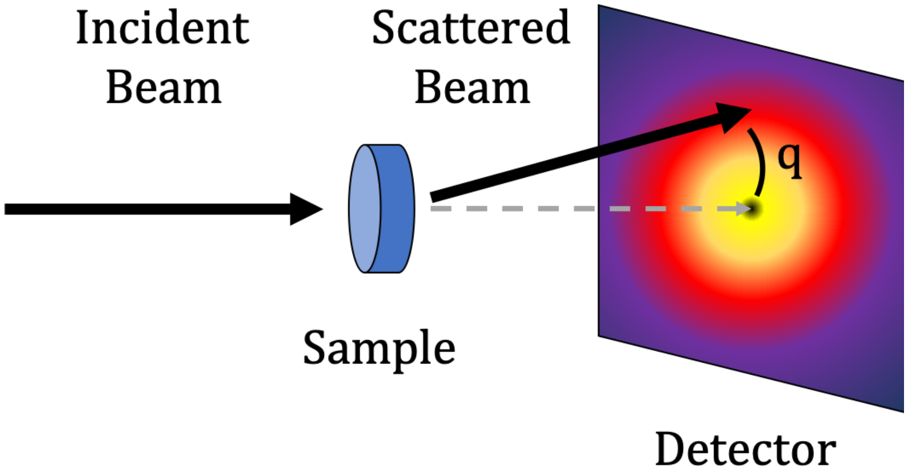

Figure 2.4: Schematic of neutron scattering experiment. An incident beam of neutrons is passed through a titanium sample cell with quartz windows, and scattered neutron beams are collected at various angles using a planar detector. The 2-D $I(q_x, q_y)$ data is reduced through radial averaging to $I(q)$, which is fit according to Equation (2.6)

Bibliography

[1] M. E. Helgeson, S. E. Moran, H. Z. An, and P. S. Doyle, "Mesoporous organohydrogels from thermogelling photocrosslinkable nanoemulsions," *Nature Materials*, vol. 11, pp. 344–352, February 2012.

[2] L.-C. Cheng, P. D. Godfrin, J. W. Swan, and P. S. Doyle, "Thermal processing of thermogelling nanoemulsions as a route to tune material properties," *Soft matter*, vol. 14, no. 27, pp. 5604–5614, 2018.

[3] L.-C. Cheng, Z. M. Sherman, J. W. Swan, and P. S. Doyle, "Colloidal gelation through thermally triggered surfactant displacement," *Langmuir*, vol. 35, no. 29, pp. 9464–9473, 2019.

[4] L.-C. Cheng, S. M. Hashemnejad, B. Zarket, S. Muthukrishnan, and P. S. Doyle, "Thermally and ph-responsive gelation of nanoemulsions stabilized by weak acid surfactants," *Journal of Colloid and Interface Science*, 2019.

[5] B. J. Berne and R. Pecora, "Dynamic light scattering: with applications to chemistry, biology and physics. 2000," *Mineola, NY: Dover Publications*, vol. 376.

[6] C. Johnson, *Laser light scattering.* New York: Dover, 1994.

[7] K. Meleson, S. Graves, and T. G. Mason, "Formation of concentrated nanoemulsions by extreme shear," *Soft Materials*, vol. 2, no. 2-3, pp. 109–123, 2004.

[8] C. Macosko, *Rheology : principles, measurements, and applications.* New York: VCH, 1994.

[9] R. G. Larson, *The structure and rheology of complex fluids*, vol. 150. Oxford university press New York, 1999.

[10] K. Hyun, M. Wilhelm, C. O. Klein, K. S. Cho, J. G. Nam, K. H. Ahn, S. J. Lee, R. H. Ewoldt, and G. H. McKinley, “A review of nonlinear oscillatory shear tests: Analysis and application of large amplitude oscillatory shear (laos),” *Progress in Polymer Science*, vol. 36, no. 12, pp. 1697–1753, 2011.

[11] S. A. Rogers and M. P. Lettinga, “A sequence of physical processes determined and quantified in large-amplitude oscillatory shear (laos): Application to theoretical nonlinear models,” *Journal of Rheology*, vol. 56, no. 1, p. 1, 2011.

[12] L. C. Hsiao and P. S. Doyle, “Celebrating soft matter’s 10th anniversary: Sequential phase transitions in thermoresponsive nanoemulsions,” *Soft Matter*, vol. 11, no. 43, pp. 8426–8431, 2015.

[13] M. B. Gordon, C. J. Kloxin, and N. J. Wagner, “The rheology and microstructure of an aging thermoreversible colloidal gel,” *Journal of Rheology*, vol. 61, no. 1, pp. 23–34, 2017.

[14] J. Läuger and P. Heyer, “Rheo small angle light scattering (rheo-sals) and rheo-microscopy as tools for investigations of structure-property relations in complex fluids,” *Ann. Trans. Nordic Rheol. Soc*, vol. 14, pp. 193–196, 2006.

[15] W. Kemp, *NMR in chemistry : a multinuclear introduction.* Houndmills, Basingstoke, Hampshire: Macmillan Education, 1986.

[16] B. T. M. Willis, ed., *Chemical applications of thermal neutron scattering.* Harwell series, London: Oxford University Press, 1973.

[17] B. Hammouda, “Probing nanoscale structures-the sans toolbox. national institute of standards and technology,” *Center for Neutron Research, Gaithersburg, MD, USA*, 2016.

Chapter 3

Developing an effective interaction potential for thermoresponsive polymer bridging attractions

In the present chapter, we develop a model interaction potential for thermoresponsive nanoemulsions based from fundamental arguments of the physics of intercolloidal polymer bridging. Prior to our work, several groups have addressed potential forms of the thermoresponsive attractions in polymer-nanoemulsion suspensions, with forthcoming descriptions in this chapter. Gao et al. used a relatively coarse hard sphere plus square well interaction to find an approximate boundary for phase separation based on Monte Carlo simulations, [1] and Cheng et al. considered classical DLVO interactions combined with depletion attractions to describe the bridging process in response to changes in pH as well as temperature. [2]

Generally, unlike atomic interactions which are governed by elemental chemistry, colloid-colloid interactions are often described as effective potentials arising from combinations of fundamental physical phenomena including London dispersion forces, electrostatic interactions, fluid-colloid interactions, and surface forces. [3, 4] As a result, colloidal systems can give rise to much wider variety of interparticle potentials that, in theory, can lead to a sea of exotic phases. [5] The early theories underlying effective potentials can be seen through examples such as the celebrated Derjaguin-Landau-Verwey-Overbeek (DLVO) theory, which accounts for the effective contributions from van der Waals attraction as well as electrostatic repulsion. [6] The development of DLVO potentials provides a functional form for the decay of attraction as well as repulsion. In another vein, Asakura-Oosawa theory provides a simple understanding of polymer-mediated depletion interactions between colloids, where the exclusion of non-adsorbing polymer between neighboring colloids results in a net pressure that can be described by an effective intercolloid attraction. [7]

There are, however, many other demonstrations of colloidal interactions that do not have potentials easily reduced to classical theories. For example, the early formation and gelation of cement hydrates have been modeled with a potential that combines a short ranged attraction with a Yukawa repulsion. [8] As another instance, the Baxter potential used to model so-called "sticky" hard spheres accounts for a narrow (but finite) interaction well such that colloids irreversibly aggregate on contact, hence "sticky". [9–11] In larger biological systems such as those involving complex proteins, two Yukawa potentials have been employed to broadly capture their overall attractive and repulsive components, allowing for adjustable features that can appear qualitatively similar to either DLVO or Lennard-Jones potentials. [12–15] The two Yukawa potential, as will be discussed later on, is a particularly useful model due to its mathematical tractability in calculations associated with thermodynamic and scattering data. While models of varying complexity can be considered to describe colloidal interactions, we will find that the potential we ultimately pursue is consistent with both a physical understanding and experimental observations of thermoresponsive nanoemulsions.

3.1 Molecular origins of thermoresponsive behavior

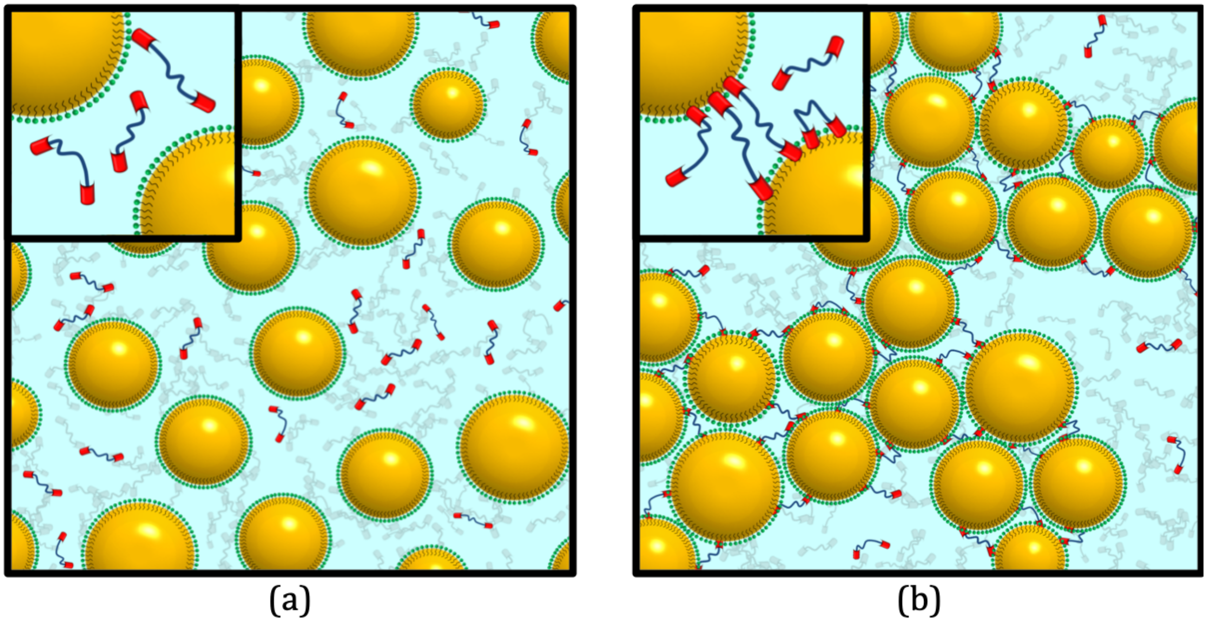

Figure 3.1: The thermoresponsive colloidal system is composed of silicone oil-in-water nanoemulsions with SDS as surfactant and short-chain PEGDA (Mn 700) as bridging polymer. (a) At room temperature the nanoemulsions are freely suspended in aqueous solution with polymer chains not predominately bridging. (b) At elevated temperatures the acrylate ends of the PEGDA preferentially partition into the oil phase due to the hydrophobic effect. Over time, the system forms a percolated, elastic colloidal gel network whose strands are formed by bridged nanoemulsion clusters.

To begin developing a reasonable model for effective interdroplet interactions, we consider the physical mechanisms at play in colloidal gelation of thermoresponsive nanoemulsions. Figure 3.1 depicts the transition from colloidal suspension to colloidal gel with all the chemical species present. As evidenced by neutron scattering experiments and variations in polymer end group chemistry, increasing hydrophobicity of the end groups results in an apparent increase in attraction strength and decrease in gelation temperature. [1, 16–18] The hypothesized mechanism of colloidal gelation is attributed to adsorption of the hydrophobic polymer end groups to the nanoemulsion oil droplet surface. As understood through the hydrophobic effect, the entropic penalty that drives polymer bridging originates from the increase in configuration constraints imposed on water molecules that have to order around the acrylate end groups. [19] The contribution to the Gibbs free energy, G, due to this ordering penalty increases with temperature, as understood through the relationship between the Gibbs free energy and entropy, S

$$\Delta G = \Delta H - T\Delta S \tag{3.1}$$

where H is the enthalpic contribution.

By thinking of effective interdroplet interactions in terms of the bridging polymer, we can begin to develop qualitative features necessary to reflect the fundamental polymer bridging physics. As two nanoemulsions are brought together from infinite separation, there should be no significant net interaction until their separation is on the order of the radius of gyration (R_g) of the bridging polymer. Additionally, because the polymers introduce an excluded volume between droplets, as adsorbed polymers are compressed beyond their preferred bridging length, there will be an additional entropic repulsion as they approach separations less than R_g. Because the nanoemulsion system includes anionic surfactant to stabilize the oil/water interface, the charges will cause an electrostatic repulsion between droplets. Finally, we expect two droplets to not overlap, and so there should be nearly hard sphere behavior related to the radius of droplets.[1]

To explore the polymer bridging interaction more deeply, we consider that in terms of configuration space, each polymer bridge between nanoemulsions as capable of attaining one of four conformations: free in solution, singly tethered, looped, or bridging. Figure 3.2 illustrates these possibilities, which can be generally drawn from the underlying theoretical descriptions of telechelic bridging chains (both polymeric and micellar) be-

---

[1] Although in principle fluid droplet particles should exhibit a softer repulsive wall at contact compared to solid particles, the absolute length scale of the nanoemulsions results in a high Laplace pressure and thus a steep, soft wall for individual emulsions since the Laplace pressure scales inversely with droplet radius.

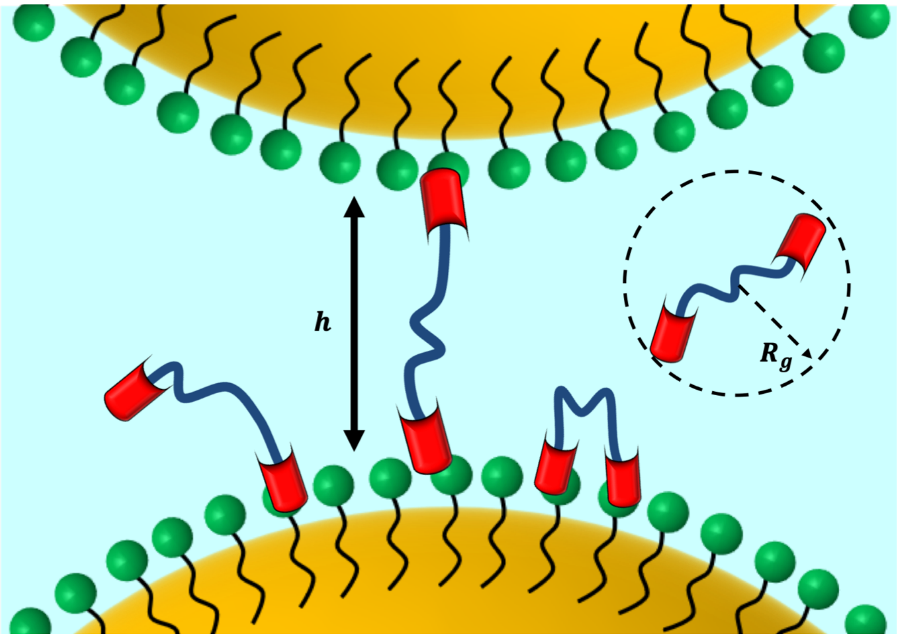

Figure 3.2: Depiction of possible bridging polymer configurations to motivate qualitative features of the effective intercolloidal interaction potential, where h is the interdroplet distance that can be nondimensionalized with the droplet diameter. The presence of attractions due to telechelic bridging polymers will be associated with a preferred spacing of nanoemulsions on the order of R_g for the PEGDA polymer. The entropic penalty of compressing polymer chains at distances less than R_g will be captured by repulsion near contact.

tween surfaces. [20–22] To develop a theoretical expectation for the shape of interactions mediated by polymer bridging, we can outline a formalism originally developed by Dolan and Edwards to describe polymer bridging statistical mechanics. [20] The model begins by considering a single, ideal polymer chain between parallel surfaces. In one dimension, we first determine the probability that a chain of length s begins at a position x and ends at another position x'. If we call the configurational probability density function for this polymer $G = G(x, x', s)$, the partial differential equation (PDE) and boundary conditions describing the single chain are given by

$$\frac{\partial G}{\partial s} = \frac{l^2}{6}\frac{\partial^2 G}{\partial x^2} \tag{3.2a}$$

$$G(0, x', s) = 0 \tag{3.2b}$$

$$G(h, x', s) = 0 \tag{3.2c}$$

$$G(x, x', 0) = \delta(x - x') \tag{3.2d}$$

where l is the segment length of the polymer, h is the distance between the surfaces, and $\delta(x)$ is the Dirac delta function. The boundary conditions (3.2b) and (3.2c) ensure that the polymer does not penetrate the surfaces, and the initial condition (3.2d) ensures that the chain begins at x'.

From the solutions to the PDE, the single chain partition function z is found by integrating $G(x, x', s)$ over all possible starting and ending positions. Analytic expressions in the limit of short and infinite separation can be obtained up to terms of order $\frac{1}{N}$, where N is the number of polymer chain segments. [21, 23]

For a system that exhibits reversible adsorption of the end groups, we must account for the four possible configurations of a polymer, as shown in Figure 3.2. To incorporate the energy E_{ads} required for an end group to reversibly adsorb onto the droplet surface, we weight each configurational partition function by a Boltzmann factor, which is a technique that has been applied to a similar model of reversible micellar adsorption. [22] Overall, we express our partition function:

$$z_n(h, N, E_{ads}) = \frac{\left(\xi \mathrm{e}^{E_{ads}/k_B T}\right)^n}{h} \int_{x'_0}^{x'_1} \int_{x''_0}^{x''_1} G(x', x'', N)\, dx'\, dx''$$

where N is the total number of chain segments, k_B is Boltzmann's constant, T is the absolute temperature, n is the number of adsorbed end groups (either 0, 1 or 2), and

ξ accounts for the finite confinement distance of a chain end near each surface within a distance ξ. [21] The integration bounds, which depend on n, are:

$$[(x_0', x_1'), (x_0'', x_1'')] = \begin{cases} [(0,h),(0,h)] & \text{if } n = 0 \\ [(0,\xi),(0,h)] & \text{if } n = 1 \\ [(0,\xi),(0,\xi)] & \text{if } n = 2 \text{ (loop)} \\ [(0,\xi),(h-\xi,\xi)] & \text{if } n = 2 \text{ (bridge)} \end{cases} .$$

By summing the contributions of the four partition functions, we calculate an effective Helmholtz energy per chain that is normalized by the free energy of an unconfined chain.

$$\frac{A_{plate}(h,N,E_{ads})}{k_B T} = -\ln\left[\sum_{n=0}^{2} \frac{z_n(h,N,E_{ads})}{z_n(\infty,N,E_{ads})}\right]$$

The energy between parallel plates can be converted to an energy between two spheres via the Derjaguin approximation,

$$A_{sphere} = \pi a \int_{r-2a}^{\infty} A_{plate}(x)\, dx \tag{3.3}$$

which is valid if the interdroplet center-to-center distance r is much smaller than the sphere radii a. [6] In the simulated system, we typically use PEGDA700 (radius of gyration $R_G \approx 1$ nm) [24] between nanodroplets of diameter $20-30$ nm.

Further, only a fraction of N_P, the total number of polymers per nanodroplet, are available to form bridges. This fraction is based on the accessible droplet surface between two spherical droplets. The relationship between r and maximum fractional surface coverage f_P of bridging chains is given by

$$f_P(r) = \frac{1}{\pi}\cos^{-1}\left(\frac{r-L_{max}}{2a}\right).$$

The final, adjusted equation for the total effective interdroplet potential is

$$U_{sphere}(r, N, E_{ads}) = aN_P \cos^{-1}\left(\frac{r - L_{max}}{2a}\right) \int_r^\infty A_{plate}(h, N, E_{ads})\, dh \tag{3.4}$$

This potential, in totality, provides an effective interaction between two nanodroplets due to the presence of bridging polymer. Closure is achieved if the temperature dependence of the adsorption energy is known. Figure 3.3 illustrates the shape of the potentials calculated through this method. The key features that we aim to recapitulate through a coarse-grained potential include a short-ranged repulsion and long-ranged attraction.

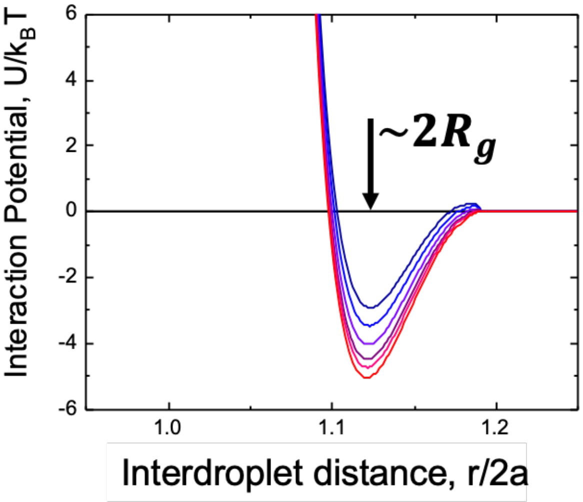

Figure 3.3: Resulting interaction potential from a statistical mechanical treatment of polymer bridging configurations as described in the text, Equation (3.4). the interaction potential exhibits a repulsion at close contact due to the brush and loop configurations, followed by a longer-ranged attraction due to polymer bridges at a distance comparable to $2R_g$. At progressively farther interdroplet distances, the interaction decays to zero because it is farther than the physical length of the stretched polymer chain.

Putting together the interaction components to establish the effective interparticle potential, we can consider the thermoresponsive behavior of each interaction component. The electrostatics will scale linearly with absolute temperature [19], and the polymer bridging, as considered above, will be temperature dependent with an exponential weight due to the adsorption energy. The hard sphere behavior will not significantly be affected by temperature, although physically there may be very weak changes in relative viscosity of the dispersed and continuous fluids. Overall, from molecular considerations of the effective interparticle potential, we see that a sufficient coarse-grained interaction model should account for a short-ranged repulsive component (hard sphere plus electrostatic repulsion) that is relatively temperature-insensitive with a relatively longer ranged attraction away from contact having a temperature-sensitive strength of the attraction minimum. Next, we move on to build up to the proper temperature scale and see that the two Yukawa potential provides a reasonable form to capture these desired features.

3.2 Second Virial Coefficient and Temperature

Temperature, pressure, and specific volume are all intensive system properties that commonly define a multidimensional space for mapping out phase behavior. The phase space in which we wish to understand the thermoresponsive nanoemulsion exists in the 2-D plane of temperature T and droplet volume fraction ϕ, which we justify because we observe that the complex arrested phase separation behavior occurs with change in system temperature, resulting in a gel with droplet dense and droplet dilute regions. However, in developing an interaction potential model, the natural energy scale that arises is the attraction strength ϵ, which typically describes the magnitude of the interaction strength (in units of k_BT) and is itself a function of temperature, $\epsilon = \epsilon(T)$. To properly nondimensionalize the effective temperature for any given shape of interaction potential, we calculate the second virial coefficient, which for spherically isotropic interactions is given by [25]

$$B_2(T) = -2\pi \int_0^\infty dr\ r^2 \left[\mathrm{e}^{-\beta U(r,T)} - 1\right] \tag{3.5}$$

where $\beta = (k_B T)^{-1}$. The use of the second virial coefficient as an effective temperature for different forms of interaction potentials is motivated by seminal work on the so-called extended corresponding states framework of Noro and Frenkel, where it was shown that for attractive colloids the second virial coefficient can be used as an effective temperature to compare qualitatively different short-ranged potentials. [26] This universality across varying potentials has proven valid up to the limit of attractive systems that also exhibit long-ranged repulsion. [27] Physically, the second virial coefficient describes the first order nonideal behavior of a fluid. [25] In subsequent sections, we develop the interaction potential theories that resolve our search for a suitable interaction potential that allows us to better model and understand the thermoresponsive colloidal gelation process. Calculating the second virial coefficient provides a unifying effective temperature scale for comparisons between experiment and theory for different candidate potentials.

3.3 Hard sphere

Perhaps the most basic model for non-ideal particle systems introduces a hard sphere interaction. That is, rather than assume that each substituent particle behaves ideally as a zero-dimensional point, we now account for the fact that the particles take up some non-zero amount of volume. The pair interaction potential, $U(\tilde{r})$, for such a system is expressed as

$$U(\tilde{r}) = \begin{cases} \infty & \tilde{r} < 1 \\ 0 & \tilde{r} \geq 1 \end{cases} \tag{3.6}$$

where the center-to-center, dimensional distance between particles r is normalized by the average particle diameter σ_{HS}, $\tilde{r} = \dfrac{r}{\sigma_{HS}}$. It can be shown that the resultant phase diagram for a hard sphere system is one dimensional, being only controlled by the volume fraction ϕ of particles in the system. [28] Because the resultant phase diagram is not an explicit function of temperature, the hard sphere behavior is considered athermal. This is also seen in calculation of its second virial coefficient using Equation (3.5), which becomes

$$B_2(T) = B_2 = \frac{2\pi\sigma_{HS}^3}{3} \tag{3.7}$$

As we will describe in the subsequent section, the above athermal hard sphere second virial coefficient is used as a normalization term for potentials of increasing complexity to measure their strength relative to excluded volume effects.

3.4 Square Well Attractions

To model the net aggregation observed in colloidal assembly, the hard sphere form can be modified with a region of negative potential i.e., attraction. For example, so-called "sticky" hard spheres describe hard spheres that becomes attached upon contact via a Baxter potential of vanishing width and approaching infinite well depth. [29] For potentials of a wider range, as is the case based on the polymer bridging interaction evident in thermoresponsive nanoemulsions, a finite-width square well should be considered, having the form

$$U\left(\tilde{r},T\right) = \begin{cases} \infty & \tilde{r} < 1 \\ -\varepsilon(T) & 1 \leq \tilde{r} < \lambda \\ 0 & \tilde{r} \geq \lambda \end{cases} \tag{3.8}$$

where ε is the temperature-dependent well depth, and λ is the width of the attractive well. For the nanoemulsion system, we contend that the well depth should be temperature dependent with a fixed width because the latter is set by the physical constraints of the bridging polymer. Although the radius of gyration for the polymer may varying slightly across the temperatures studied, we treat any deviations as a higher order effect and approximate the interaction range as constant.

Because this potential adds the attraction on top of the hard sphere repulsion, it is often referred to as a “hard sphere plus square well” (HSSW) potential. The second virial coefficient associated with this potential can be described analytically using Equation (3.5) and piecewise integrating the expression over the three regions. Furthermore, since we expect hard sphere behavior to underlie any additional contributions from attractions, we calculate the reduced second virial coefficient B_2^* given by

$$B_2^*(T) = \frac{B_2(T)}{B_2^{HS}} = 1 - 3\int_1^\infty d\tilde{r}\ \tilde{r}^2 \left[\mathrm{e}^{-\beta U(\tilde{r},T)} - 1\right] \tag{3.9}$$

where the $*$ in the superscript denotes normalization by the hard sphere contribution given in Equation (3.7). Due to the simplicity of the square well form, the analytic expression for its reduced second virial coefficient is realized as

$$B_{2,SW}^*(T) = 1 - \left(\lambda^3 - 1\right)\left[\mathrm{e}^{\beta\varepsilon(T)} - 1\right]. \tag{3.10}$$

To appreciate the limiting behavior of the above expression, it is clear that as $\lambda \to 1$ and/or $\varepsilon \to 0$, then $B_{2,SW}^*(T) \to 1$, approaching purely hard sphere behavior. Inversely, as λ and ε are increased, $B_{2,SW}^*$ becomes more negative.

3.5 Two Yukawa model

The Yukawa potential describes interactions of the general functional form $U(\tilde{r}) \propto \mathrm{e}^{-\tilde{r}}/\tilde{r}$. [30] Depending on the sign of the proportionality, the Yukawa potential can either describe an attraction or repulsion term that decays with increasing distance. To generalize an effective intercolloidal potential, we use a combination of two Yukawa terms reflecting an attractive and repulsive component. This form has been observed to suitably describe complex protein systems as well as other large molecular systems such as fullerenes and asphaltenes. [14, 31–33] With respect to Derjaguin-Landau-Verwey-Overbeek theory, screened Coulombic potentials between interacting spheres would fall into the general form of Yukawa-type potentials. Additionally, Yukawa potentials have been used to capture polymer-induced interactions with combinations of depletion and bridging. [34] Its usefulness in analytical predictions arises from a known form for the Laplace transform of the hard sphere pair-correlation function, which shall be made apparent in deriving the free energy equations in Chapter 4.

The expression we evaluate is a two-term Yukawa potential superimposed onto a hard sphere potential,

$$U\left(\tilde{r},T\right)=\begin{cases}\infty & \tilde{r}<1\\ U_{2Y}\left(\tilde{r},T\right) & 1\leq\tilde{r}\end{cases}\tag{3.11}$$

where $U_{2Y}\left(\tilde{r}\right)$ is given by

$$U_{2Y}\left(\tilde{r},T\right)=-\frac{K_1(T)}{\tilde{r}}\mathrm{e}^{-Z_1(\tilde{r}-1)}-\frac{K_2(T)}{\tilde{r}}\mathrm{e}^{-Z_2(\tilde{r}-1)}\tag{3.12}$$

for positive values of K_1 providing the magnitude of the attractive component, and negative values of K_2 providing the magnitude of the repulsive component. Analogous to the square well potential, here we only consider temperature dependence of the interaction strength parameters, $K_1 = K_1(T)$ and $K_2 = K_2(T)$. The justification relies on the physical limitations of the covalently bound bridging polymer chain, which should not vary in preferred radius of gyration greatly compared to variations in attraction strength due to end adsorption.

Because this potential does not have a reducible analytic expression for the reduced second virial, for a given set of parameters we calculate B_2^* by numerically integrating Equation (3.9) with Equation (3.12) as the interaction potential outside of hard sphere contact.

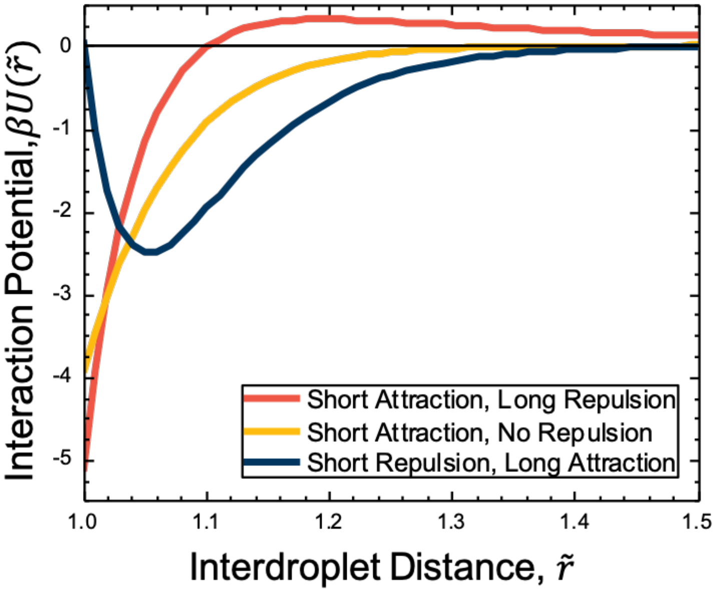

Figure 3.4: Depending on the values of the parameters used in the two Yukawa potential as shown in Equation (3.11), several different potential shapes with qualitatively different features can be considered. These include a short attraction potential with a repulsive barrier (orange), a short attraction potential with no repulsion (yellow), and a short repulsion potential with long attraction resulting in an offset minimum away from particle contact (blue). Based on our physical arguments of the polymer bridging attractions, we proceed with the short repulsion and long attraction potential.

As Figure 3.4 shows, the family of potentials described by the two Yukawa can vary in qualitative features, either resulting in a relatively long ranged repulsive barrier, a pure attraction with attraction at contact, and finally an offset attraction minimum with repulsion at closer distances. Given the features of polymer bridging physics detailed in Section 3.1, only the third of these three options reflects what we would expect to see in an effective potential arising from the PEGDA chains. To systematically evaluate the family of two Yukawa potentials with an offset minimum, we consider a reparameterized form of Equation (3.12) that explicitly includes the radial location, $\tilde{r}_m$, and temperature-dependent depth of the interaction potential well, $\epsilon(T)$. Ultimately, our objective is to provide expressions for $K_1(T)$ and $K_2(T)$ for the thermoresponsive nanoemulsions. To facilitate this, it is convenient to recast the 2Y potential in terms of $\tilde{r}_m$ and $\epsilon(T)$ while maintaining the attraction and repulsion range parameters. A detailed derivation of the reparameterization is provided in Appendix A. Notice also that we instead consider the parameter $\kappa \equiv \dfrac{Z_2}{Z_1}$ as the ratio of attraction range to repulsion range, only considering potentials where $\kappa > 1$ which qualitatively results in a finite interaction minimum offset from particle contact (blue line in Figure 3.4). Potentials where $\kappa < 1$ describe the family of potentials with an energy barrier offset from particle contact (red line in Figure 3.4), are not considered in this analysis.

$$
\begin{aligned}
K_1 &= \epsilon(T)\frac{(\kappa Z_1 \tilde{r}_m + 1)}{Z_1(\kappa - 1)}\mathrm{e}^{Z_1(\tilde{r}_m - 1)} \\
K_2 &= -\epsilon(T)\frac{(Z_1 \tilde{r}_m + 1)}{Z_1(\kappa - 1)}\mathrm{e}^{\kappa Z_1(\tilde{r}_m - 1)}
\end{aligned}
\tag{3.13}
$$

With the above relationships substituted for the strength of attraction and repulsion terms, Equation (3.12) becomes

$$
U_{2Y}(\tilde{r}, T) = -\epsilon(T)\frac{\left[(\kappa Z_1 \tilde{r}_m + 1)\,\mathrm{e}^{-Z_1(\tilde{r} - \tilde{r}_m)} - (Z_1 \tilde{r}_m + 1)\,\mathrm{e}^{-\kappa Z_1(\tilde{r} - \tilde{r}_m)}\right]}{\tilde{r} Z_1(\kappa - 1)} \tag{3.14}
$$

By inspection, it is clear that $U(\tilde{r} = \tilde{r}_m, T) = -\epsilon(T)$, satisfying the function behavior we set out to achieve. Thus, for any specified values for the interaction strength, interdroplet distance at the well minimum, and range parameters, Equations (3.12) and (3.14) can be used interchangeably.

Moving forward, in using the two Yukawa potential to model effective interactions, we are in effect coarse-graining the detailed molecular contributions from the surfactant, polymer, and solvents that comprise the nanoemulsion system. Through this analysis these details are subsumed into an effective medium across which the individual nanoemulsion droplets interact.

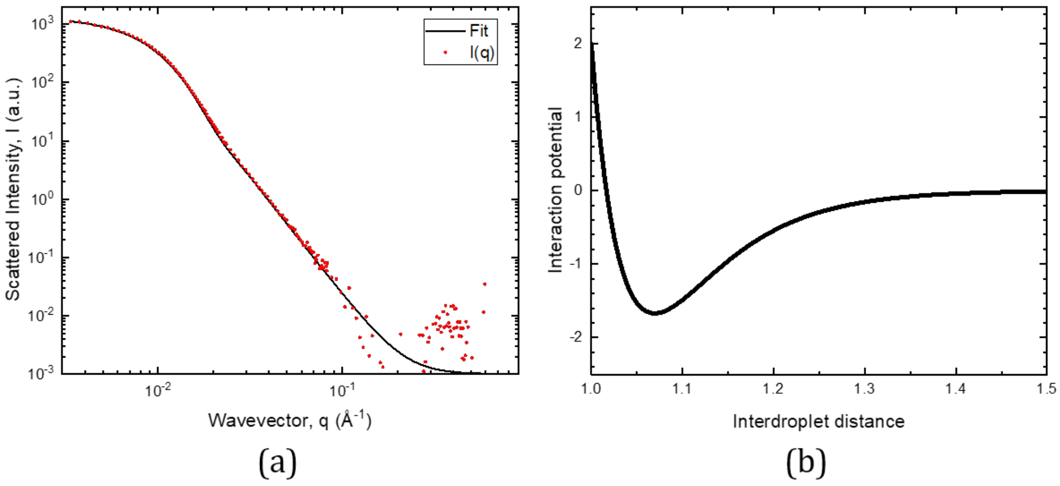

(a)

(b)

Figure 3.5: Determination of interaction potential using small angle neutron scattering data. Best fit parameters, in line with Equation (2.6), are summarized in Table 3.1. (a) The reduced intensity data points in red, along with the model fit in black composed of a Schulz sphere contribution for the form factor and a Two Yukawa interaction potential for the structure factor. (b) The two Yukawa potential associated with the scattering data at 25 °C. Fit parameters and equivalent reparameterization values are also shown in Table 3.2

3.6 Two Yukawa Parameters from SANS Data

Two Yukawa parameters can be determined from small angle neutron scattering data of the thermoresponsive nanoemulsion as a function of temperature. To this end, we make use of previously published scattering data initially fit to a hard sphere plus square well model. [16] The scattering data is processed using the SANS Data Analysis package provided by the National Institute for Standards and Technology Center for Neutron Research (NCNR). Figure 3.5 shows representative reduced scattering data with the corresponding model fit.

By converting these fit parameters into the physical parameters which include $\tilde{r}_{min}$ as shown in Table 3.2, we see that the well minimum is located at $\tilde{r}_{min} \approx 1.07$, corresponding to a dimensional distance of $r_{min} \approx 2.8$ nm for a droplet radius of 20 nm. This value is

Parameter	Value	Units
Volume Fraction, ϕ	9.417e-03	
Radius, a	17.097	nm
Polydispersity	0.3067	
Droplet Scattering Length Density	1.24e-06	Å^{-2}
Solvent Scattering Length Density	6.38e-06	Å^{-2}
Attraction Strength, K_1	9.0654	
Attraction Range, Z_1	12.5575	
Repulsion Strength,K_2	-11.0512	
Repulsion Range, Z_2	24.6046	
Background	0.001	$\text{cm}^{-1}\text{sr}^{-1}$

Table 3.1: Fit parameters for SANS data at 25 °C. The parameters describing attraction and repulsion are used to develop the two Yukawa potential as a model interaction for thermoresponsive gelation. The volume fraction, radius, and polydispersity are held fixed for varying temperatures as they contribute to the form factor contribution to the scattering intensity. The scattering length densities and background intensity are fixed, with the former calculated from the chemical compositions. [35] The attraction and repulsion ranges are fit at the 25 °C reference temperature and held fixed across all other temperatures, while the attraction and repulsion strengths are allowed to vary with temperature.

consistent with the expected location for PEGDA in free solution, as the diameter of a chain is reported as $2R_g \approx 2.5\,\text{nm}$. [24]

For comparison, we can also see how the new two Yukawa form of potential compares against the prior, simplified model using the HSSW potential. As shown in Figure 3.6, pairs of curves at equivalent second virial coefficients are shown in identical color for the continuous two Yukawa and the discontinuous square well. Because the second virial coefficient calculation has a weighing factor of $\tilde{r}^2$, a two Yukawa potential with equivalent B_2^* to a HSSW potential results in a deeper attraction well minimum to compensate for the smooth decay to zero net interaction with increasing interdroplet separation.

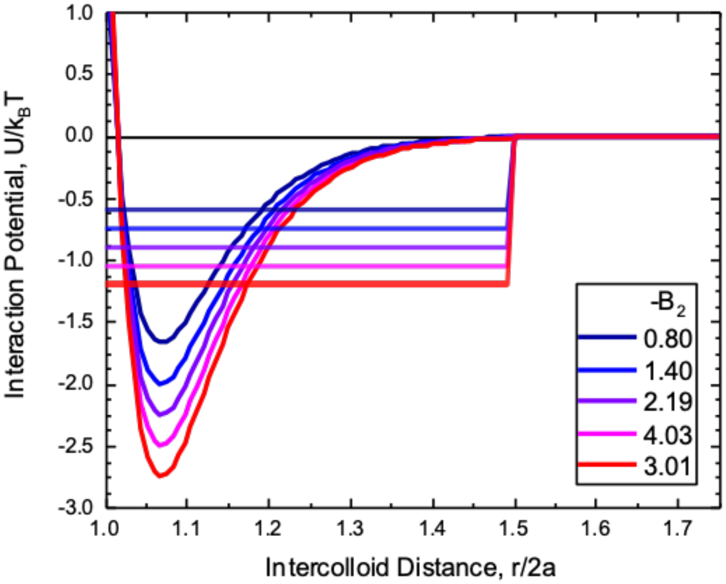

Figure 3.6: Comparison of square well and two Yukawa interaction potentials. Both potentials are fit to the same intensity data measured via neutron scattering.

3.7 Conclusions

In this chapter, we have established a usable interaction potential for thermoresponsive nanoemulsions by developing physical arguments and fitting experimental scattering data. We find that the two Yukawa potential, which has proven useful in modeling other colloidal systems, can be reparameterized to provide physically meaningful parameters that capture the preferred polymer bridging distance between nanoemulsions. We ratio-

SANS Fit Parameter	Fit Value	Recast 2Y Form Parameter	Value
K_1	9.0654	ϵ	1.6705
Z_1	12.5575	Z_1	12.5575
K_2	-11.0512	$\tilde{r}_{min}$	1.0695
Z_2	24.6046	κ	1.9594

Table 3.2: Two Yukawa parameters for the different parameterization of the potential, via Equations (3.12) and (3.14). These parameters correspond to a temperature of 25 °C, or equivalently $B_2^* = -0.80$.

nalize the particular form of the two Yukawa potential (i.e., having a short range repulsion and long range attraction) by evaluating a simple statistical mechanical model for end-adsorbing polymer bridging configurations. From neutron scattering data, we can extract a set of parameters to concisely describe the observed thermoresponsive nanoemulsion behavior.

The work that remains ahead includes further usage and validation of this rationalized interaction potential. As we will see in the subsequent chapter, mean field free energy calculations can be employed to provide testable predictions of phase behavior in the thermoresponsive nanoemulsion system.

Bibliography

[1] Y. Gao, J. Kim, and M. E. Helgeson, "Microdynamics and arrest of coarsening during spinodal decomposition in thermoreversible colloidal gels," *Soft Matter*, vol. 11, no. 32, pp. 6360–6370, 2015.

[2] L.-C. Cheng, S. M. Hashemnejad, B. Zarket, S. Muthukrishnan, and P. S. Doyle, "Thermally and ph-responsive gelation of nanoemulsions stabilized by weak acid surfactants," *Journal of Colloid and Interface Science*, 2019.

[3] J. Mewis and N. J. Wagner, *Colloidal suspension rheology.* Cambridge New York: Cambridge University Press, 2012.

[4] N. Verhaegh and H. Lekkerkerker, "Phase transitions in colloidal suspensions," in *International School of Physics Enrico Fermi*, vol. 134, pp. 347–381, IOS Press, 1997.

[5] C. P. Royall, "Hunting mermaids in real space: known knowns, known unknowns and unknown unknowns," *Soft Matter*, vol. 14, no. 20, pp. 4020–4028, 2018.

[6] B. V. Derjaguin, "Untersuchungen über die reibung und adhäsion, iv," *Colloid & Polymer Science*, vol. 69, no. 2, pp. 155–164, 1934.

[7] S. Asakura and F. Oosawa, "On interaction between two bodies immersed in a solution of macromolecules," *The Journal of Chemical Physics*, vol. 22, no. 7, pp. 1255–1256, 1954.

[8] K. Ioannidou, M. Kanduč, L. Li, D. Frenkel, J. Dobnikar, and E. Del Gado, "The crucial effect of early-stage gelation on the mechanical properties of cement hydrates," *Nature communications*, vol. 7, p. 12106, 2016.

[9] S. Buzzaccaro, R. Rusconi, and R. Piazza, "sticky hard spheres: equation of state, phase diagram, and metastable gels," *Physical review letters*, vol. 99, no. 9, p. 098301, 2007.

[10] A. P. Eberle, N. J. Wagner, and R. Castañeda-Priego, "Dynamical arrest transition in nanoparticle dispersions with short-range interactions," *Physical review letters*, vol. 106, no. 10, p. 105704, 2011.

[11] A. P. Eberle, R. Castaneda-Priego, J. M. Kim, and N. J. Wagner, "Dynamical arrest, percolation, gelation, and glass formation in model nanoparticle dispersions with thermoreversible adhesive interactions," *Langmuir*, vol. 28, no. 3, pp. 1866–1878, 2012.

[12] S.-H. Chen, M. Broccio, Y. Liu, E. Fratini, and P. Baglioni, "The two-yukawa model and its applications: the cases of charged proteins and copolymer micellar solutions," *Applied Crystallography*, vol. 40, no. s1, pp. s321–s326, 2007.

[13] J. Wu, Y. Liu, W.-R. Chen, J. Cao, and S.-H. Chen, "Structural arrest transitions in fluids described by two yukawa potentials," *Physical Review E*, vol. 70, no. 5, p. 050401, 2004.

[14] Y. Liu, W.-R. Chen, and S.-H. Chen, "Cluster formation in two-yukawa fluids," *The Journal of chemical physics*, vol. 122, no. 4, p. 044507, 2005.

[15] Y. Liu, E. Fratini, P. Baglioni, W.-R. Chen, and S.-H. Chen, "Effective long-range attraction between protein molecules in solutions studied by small angle neutron scattering," *Physical review letters*, vol. 95, no. 11, p. 118102, 2005.

[16] M. E. Helgeson, S. E. Moran, H. Z. An, and P. S. Doyle, "Mesoporous organohy-

drogels from thermogelling photocrosslinkable nanoemulsions," *Nature Materials*, vol. 11, pp. 344–352, February 2012.

[17] M. E. Helgeson, Y. Gao, S. E. Moran, J. Lee, M. Godfrin, A. Tripathi, A. Bose, and P. S. Doyle, "Homogeneous percolation versus arrested phase separation in attractively-driven nanoemulsion colloidal gels," *Soft matter*, vol. 10, no. 17, pp. 3122–3133, 2014.

[18] L. C. Hsiao and P. S. Doyle, "Celebrating soft matter's 10th anniversary: Sequential phase transitions in thermoresponsive nanoemulsions," *Soft Matter*, vol. 11, no. 43, pp. 8426–8431, 2015.

[19] J. N. Israelachvili, *Intermolecular and surface forces*, vol. 53. 2011.

[20] A. Dolan and S. Edwards, "Theory of the stabilization of colloids by adsorbed polymer," in *Proceedings of the Royal Society of London A: Mathematical, Physical and Engineering Sciences*, vol. 337, pp. 509–516, The Royal Society, 1974.

[21] S. R. Bhatia and W. B. Russel, "End-Capped Associative Polymer Chains between Nanospheres: Attractions in Ideal Solutions," *Macromolecules*, vol. 33, pp. 5713–5720, jul 2000.

[22] M. E. Helgeson and N. J. Wagner, "Colloidal interactions mediated by end-adsorbing polymer-like micelles," *The Journal of chemical physics*, vol. 135, no. 8, p. 084901, 2011.

[23] H. S. Carslaw and J. C. Jaeger, "Conduction of heat in solids," *Oxford: Clarendon Press, 1959, 2nd ed.*, 1959.

[24] P. Malo de Molina, S. Lad, and M. E. Helgeson, "Heterogeneity and its influence

on the properties of difunctional poly (ethylene glycol) hydrogels: Structure and mechanics," *Macromolecules*, vol. 48, no. 15, pp. 5402–5411, 2015.

[25] D. A. McQuarrie, *Statistical thermodynamics.* HarperCollins Publishers, 1973.

[26] M. G. Noro and D. Frenkel, "Extended corresponding-states behavior for particles with variable range attractions," *The Journal of Chemical Physics*, vol. 113, no. 8, pp. 2941–2944, 2000.

[27] K. Van Gruijthuijsen, M. Obiols-Rabasa, P. Schurtenberger, W. Bouwman, and A. Stradner, "The extended law of corresponding states when attractions meet repulsions," *Soft matter*, vol. 14, no. 19, pp. 3704–3715, 2018.

[28] G. L. Hunter and E. R. Weeks, "The physics of the colloidal glass transition," *Reports on progress in physics*, vol. 75, no. 6, p. 066501, 2012.

[29] R. Baxter, "Percus–yevick equation for hard spheres with surface adhesion," *The Journal of chemical physics*, vol. 49, no. 6, pp. 2770–2774, 1968.

[30] J. Rowlinson, "The yukawa potential," *Physica A: Statistical Mechanics and its Applications*, vol. 156, no. 1, pp. 15–34, 1989.

[31] H. Guérin, "A double yukawa potential for the van der waals interaction of molecules: application to a determination of the critical temperature," *Journal of Physics: Condensed Matter*, vol. 10, no. 31, p. L527, 1998.

[32] U. Schwarz and S. Safran, "Phase behavior and material properties of hollow nanoparticles," *Physical Review E*, vol. 62, no. 5, p. 6957, 2000.

[33] E. S. Boek, T. F. Headen, and J. T. Padding, "Multi-scale simulation of asphaltene aggregation and deposition in capillary flow," *Faraday discussions*, vol. 144, pp. 271–284, 2010.

[34] J. Bergenholtz, W. C. Poon, and M. Fuchs, "Gelation in model colloid- polymer mixtures," *Langmuir*, vol. 19, no. 10, pp. 4493–4503, 2003.

[35] B. Hammouda, "Probing nanoscale structures-the sans toolbox. national institute of standards and technology," *Center for Neutron Research, Gaithersburg, MD, USA*, 2016.

Chapter 4

Equilibrium colloidal phase behavior: theoretical predictions and experimental measurements

In this chapter, we develop mean field predictions for the phase diagram of thermoresponsive nanoemulsions using an analytic technique adapted from atomistic theories of equilibrium phase behavior. As alluded to in Chapter 1, we make use of the analogy between atomic systems and colloidal systems to study colloidal behavior using shared thermodynamic concepts.

4.1 Variational free energy method

This section outlines a derivation and generalization of the variational free energy calculations carried out by Tejero et al to develop fluid and solid transition phase diagrams. [1] The estimation of the free energy landscape makes use of the Gibbs-Bogoliubov inequality, which introduces a variational parameter $\lambda \equiv \frac{\sigma_{HS}}{\sigma}$ that is adjusted to minimize the free energy estimate and provides an upper bound for the free energy at a given state point. The assumptions that are required to apply this technique include choosing a suitable reference system to which the variational parameter is applied, essentially perturbing that system in a way that captures the contributions from the additional attractions. The natural choice in our case is the hard sphere fluid, and thus the total variational free energy is given by:

$$f(\phi,T) = f_{HS}(\phi) + 12\phi\lambda^3 \int_1^\infty d\tilde{r}\ \tilde{r}^2 g_{HS}\left(\tilde{r},\phi\lambda^3\right) U(\tilde{r},T) \tag{4.1}$$

The first term in Equation (4.1) is known generally, as it captures the free energy of the reference system of purely hard spheres under the Percus-Yevick approximation. It is

$$\beta f_{HS}(\phi) = \ln\left(\frac{6\phi\Lambda^3}{\pi\sigma_{HS}^3}\right) - 1 + \frac{3\phi(2-\phi)}{2(1-\phi)^2} - \ln(1-\phi)$$

where Λ is the constant thermal de Broglie wavelength of the colloids calculated as $\Lambda = h/\sqrt{2\pi m\epsilon}$ with Planck's constant h and particle mass m, taken as unity.

The second term in Equation (4.1) can be simplified since we have chosen an explicit form for $U(r,T)$ by way of the Two Yukawa potential of Equation (3.11). By letting $\tilde{s}_1 \equiv Z_1\lambda$ and $\tilde{s}_2 \equiv Z_2\lambda$, the integral term can be evaluated using the known Percus-Yevick closure of the hard sphere fluid, as derived by Wertheim. [2] In particular, we apply the Laplace-type transform definition

$$\tilde{s}H(\tilde{s},\phi\lambda^3) = \int_0^\infty d\tilde{r}\ \tilde{r}\ \mathrm{e}^{-\tilde{s}\tilde{r}}\ g_{HS}(\tilde{r},\phi\lambda^3) \tag{4.2}$$

where $\tilde{s}$ is the transform variable and the transform $H(\tilde{s},\phi\lambda^3)$ is given by additional functions $L(\tilde{s},\phi\lambda^3)$ and $S(\tilde{s},\phi\lambda^3)$ defined as follows:

$$\begin{aligned}
H(\tilde{s},x) &= \frac{L(\tilde{s},x)}{12xL(\tilde{s},x)+S(\tilde{s},x)\mathrm{e}^{\tilde{s}}} && (4.3)\\
L(\tilde{s},x) &= \left(1+\frac{x}{2}\right)\tilde{s}+1+2x\\
S(\tilde{s},x) &= (1-x)^2\,\tilde{s}^3+6x\,(1-x)\,\tilde{s}^2+18x^2\tilde{s}-12x\,(1+2x)
\end{aligned}$$

Using these simplifications, then, the total free energy can be shown to reduce to

$$\begin{aligned}
\tilde{f}(\phi,T;\lambda) &= \beta f_{HS}+\beta f_{2Y} && (4.4)\\
f_{2Y}\left(\phi,T;\lambda\right) &= 12\phi\lambda^3\epsilon(T)\left[K_1Z_1\mathrm{e}^{Z_1}H\left(Z_1\lambda,\phi\lambda^3\right)-K_2Z_2\mathrm{e}^{Z_2}H\left(Z_2\lambda,\phi\lambda^3\right)\right]
\end{aligned}$$

where f_{HS} is as described previously. From this equation, the free energy at a given state point (ϕ,T) is calculated by determining the free energy at the λ value that minimizes the free energy with respect to λ. By calculating the profile of free energies for a range of volume fractions, the phase envelope is then determined by performing Maxwell's double tangent construction for the van der Waals loop in the $\beta f-\phi^{-1}$ plane. Figure 4.1 demonstrates the free energy plots for a calculation at a single temperature, which results in a determination of the coexisting dense (ϕ_L) and dilute (ϕ_V) volume fractions.

The routine for systematically calculating, minimizing, and tabulating free energies was implemented in MATLAB. (See Appendix B for full implementation details.) The resolution of this technique is set by the resolution in step size, $\Delta(1/\phi)$. Code validation was achieved with $\Delta(1/\phi) = 0.01$, reproducing the phase envelope developed in the original study by Tejero et al. [1].

What remains now is applying this analysis to the relevant parameters associated with the thermoresponsive nanoemulsion system.

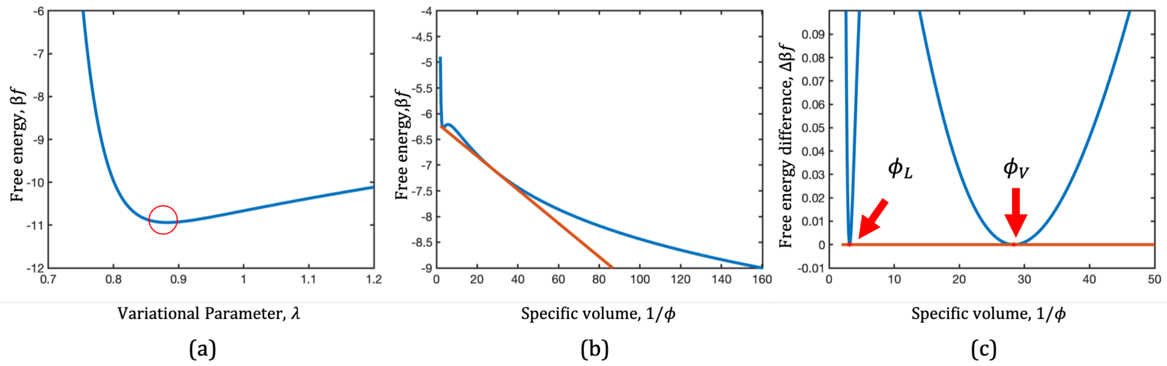

Figure 4.1: Illustration of the intermediate steps in calculations of the $T - \phi$ phase diagram based on the variational free energy. For a given T and ϕ in (a), the free energy is minimized with respect to the variational parameter λ, thereby providing a single free energy value at a given state point. By minimizing the free energy for a range of ϕ values, we develop the free energy curve in (b). Finally, in (c) the coexistence volume fractions are identified as the two volume fractions across which a common tangent line can be constructed. At state points where the phase envelope is not present, no double tangent can be constructed, and the free energy monotonically decreases with increasing $1/\phi$. The predicted spinodal boundary is determined by numerically calculating the inflection points between ϕ_L and ϕ_V in the free energy difference plots such as (c).

4.2 Comparison against Monte Carlo predictions

The resulting phase diagram can be compared against published results for a square well interaction, developed through Monte Carlo approaches. [3] Specifically, we compare against the square well width of $\lambda = 1.5$ that was previously used to model the thermoresponsive bridging interactions. [4] Using the second virial coefficient as an effective temperature, the two phase diagrams can be plotted on the same axis and compared. As seen in Figure 4.2, a majority of the phase envelope overlaps between the two methods. The largest disagreements are seen at shallower quenches and dense colloid volume fractions. Disagreements at shallow quench are expected given that the perturbational method is fundamentally a mean field approach and neglects fluctuations at near-critical quenches, whereas the Monte Carlo approach simulates individual particles with the given interaction potential which would better capture these fluctuations. Disagreement at denser volume fractions likely arises from the differences in shape of potential, with the longer-ranged square well in Monte Carlo having a shallower attraction depth and thus more stable suspensions at volume fractions $0.40 \leq \phi \leq 0.45$.

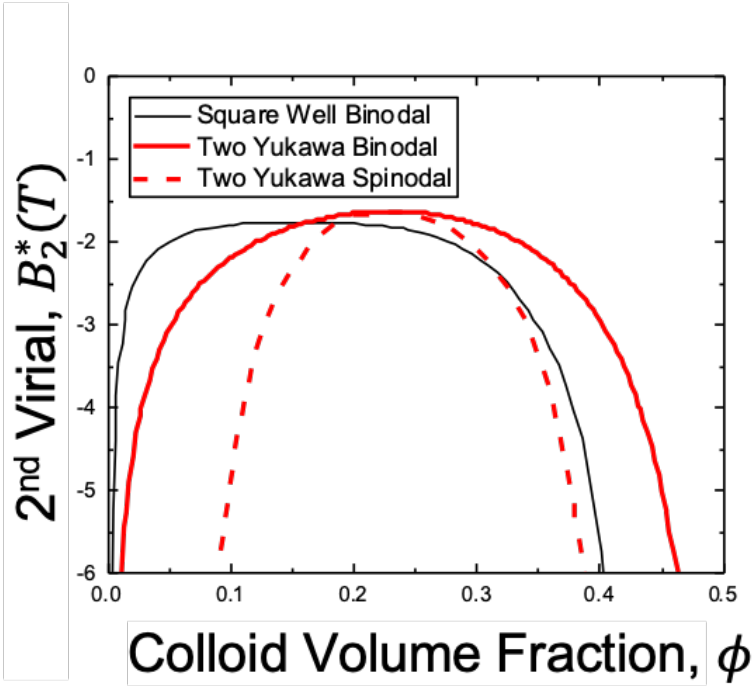

Figure 4.2: Comparison of equilibrium phase envelope predictions based on (black) a square well interaction adapted from literature [3] and (red) present development of variational free energy calculations using a two Yukawa interaction. Binodal and spinodal boundaries are determined from free energy calculations as outlined in this chapter.

4.3 Effect of interaction range on phase envelope

Although determining the two Yukawa potential parameters through SANS data analysis establishes a clear two Yukawa potential with an optimized interaction range, the sensitivity of the technique is limited because scattering is performed on volume fractions in the dilute limit to avoid multi-particle scattering effects that occlude the underlying interparticle potential. Therefore, we use the phase diagrams generated from the variational technique to explore and screen potential range parameters that arise from SANS data analysis.

To understand the effect of interaction range on the resulting phase envelope, we can artificially manipulate the reference potential in such a way that preserves the reduced second virial coefficient, hence effective temperature, while varying the decay width of the potential. We explore the family of Two Yukawa potentials with the same B_2^*, $\tilde{r}_{min}$, and $\epsilon(T = 25°C)$ but systematically vary the Z_1 and κ parameters associated with the interaction potential range. As Table 4.1 shows, the value of B_2^* is held fixed as the range parameters are varied. To quantify the range of each potential, we identify the derived property $\tilde{r}_{1\%}$, which describes the distance at which the potential has decayed to 1% of its maximum well depth.

$\epsilon(T)$	r_{min}	Z_1	κ	B_2^*	$\tilde{r}_{1\%}$
1.6705	1.0695	9.0000	4.8160	-0.8032	1.5670
1.6705	1.0695	10.0201	3.5000	-0.8032	1.5296
1.6705	1.0695	11.0000	2.7202	-0.8032	1.5017
1.6705	1.0695	12.5575	1.9594	-0.8032	1.4704
1.6705	1.0695	17.0000	1.0147	-0.8032	1.4402

Table 4.1: Family of curves showing equivalent effective temperature but varying decay range.

As seen in Figure 4.3, the phase envelope shifts to lower effective temperatures and narrows with increasing decay width. This qualitative trend allows us to make inferences about discrepancies between experiment and theoretical calculations, providing suggestions for the direction in which the model may not accurately capture the measured phase envelope.

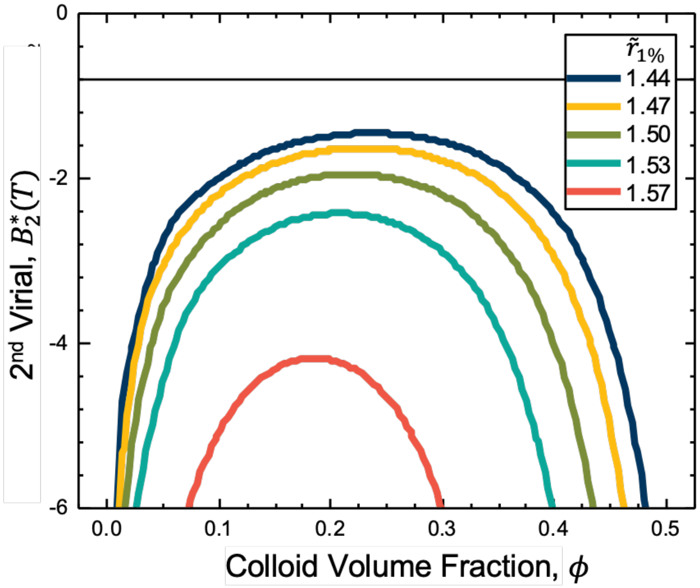

Figure 4.3: Binodal phase envelopes predicted from variational free energy calculations for different interaction widths, as described in Table 4.1. All potentials start at the same effective temperature and interaction strength, only varying the range of interaction. As the interaction strength $\epsilon(T)$ is increased, B_2^* decreases and the system proceeds into the region of phase instability.

4.4 Experimental identification of gel arrest line

Having established a theoretical framework for predicting the underlying equilibrium phase behavior of colloidal systems, we now move on to the comparison of these free energy predictions to measurable experimental phase boundaries as well as the gelation transitions that interrupt our ability to clearly identify these boundaries. First, we outline the challenges of identifying experimental phase envelopes due to the intercession of nonequilibrium colloidal gelation and structural arrest. To circumvent this gelation and resolve phase boundaries, we subsequently employ sedimentation forces as a means of driving the system toward phase equilibrium and extracting quantitative information about the colloid-dense and dilute regions of the gel.

The challenge of interrogating the phase behavior of arrested, non-equilibrium gel structure is made apparent by an experimental mapping of the gelation line relative to the region of phase instability. The relationship between gelation boundaries and phase diagrams have been observed for a variety of colloidal gel systems, [5, 6] with some studies observing the gelation boundary to lie well above the phase coexistence region as seen in a system with adhesive hard spheres, [7] and others with the gelation boundary apparently below the phase coexistence region. [8]

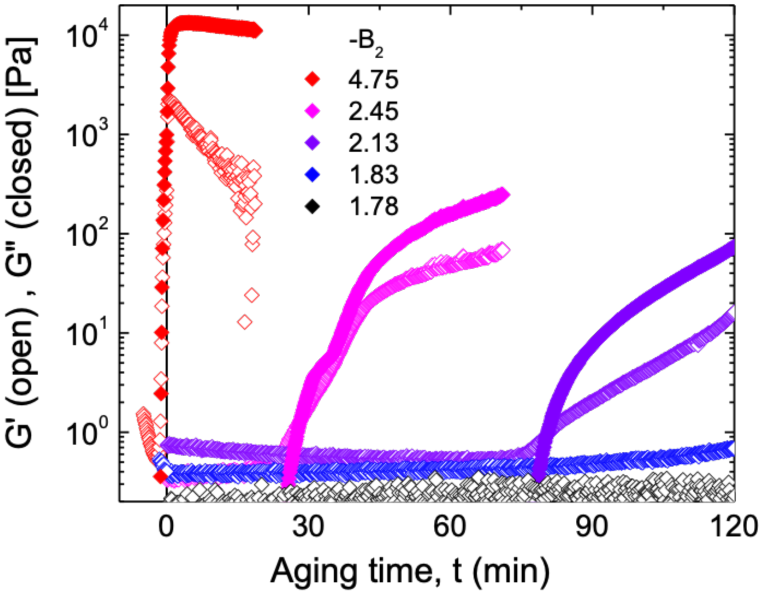

Figure 4.4: Linear viscoelastic gel aging rheology to determine minimum gelation temperature, T_{gel}, and equivalent maximum gelation second virial coefficient, $B^*_{2,gel}(T_{gel})$. For varying quenches, we let the gel age and observe the change in G' and G''.

To determine the locus of second virial coefficients above which no gel forms (or alternatively, the locus of temperature below which no gel forms), which we designate as $B_{2,gel}$, we limit our experiments to slow, quasi-static temperature quenches and give sufficient age times for gelation to be observed or at most two hours of aging, whichever occurs first. The experiments are conducted on a stress-controlled rheometer with a cone-plate geometry as described in Section 2.3.

First, nanoemulsion samples of volume fraction $\phi = 0.33$ are loaded at room temperature. Then, a temperature ramp protocol from room temperature to the final temperature at $5\,^{\circ}\mathrm{C}\,\mathrm{min}^{-1}$ is employed by the Peltier stage controlled through the rheometer software. Throughout this thermal processing, the sample undergoes small amplitude oscillatory shear at strain amplitude $\gamma_0 = 0.001$ and angular frequency $10\,\mathrm{rad}\,\mathrm{s}^{-1}$. The solid-like ($G'$) and liquid-like ($G''$) response are monitored over time, in anticipation of gelation as defined here by a crossover in G'-dominant behavior. This definition of gelation is not absolute given that more rigorous criteria exist, [9] but meeting such criteria is infeasible because the system is mutating over time scales much faster than the time scale of probing frequency sweeps. By repeating the arrest line determination for a series of droplet volume fractions, we develop the experimental points in Figure 4.5. We note that the apparent change in slope of $B_{2,gel}$ coincides closely with the spinodal boundary, which may imply that the processes below this region are governed by spinodal decomposition dynamics. In Chapter 6, we see this to be the case.

Because the majority of the region of interest for phase behavior lies within the arrested gel area, we are not immediately able to access an experimental binodal boundary. Absent an interrupting gelation transition, the colloidal phase separation process would proceed via spinodal decomposition until there were two coexisting colloidal phases — one more concentrated in droplets formed through condensing strands of droplet aggregates; and one more dilute in droplets formed within the void network intertwined with the condensing droplet strand network. However, the slowing of phase separation kinetics due to gelation leaves the resultant gel in an intermediary state within which we are not able to directly interrogate the local volume fractions of the coarsening strands. Our expectation is that the local volume fraction of the dense strand and dilute void phases should inform us about the final compositions of droplets that each phase is evolving

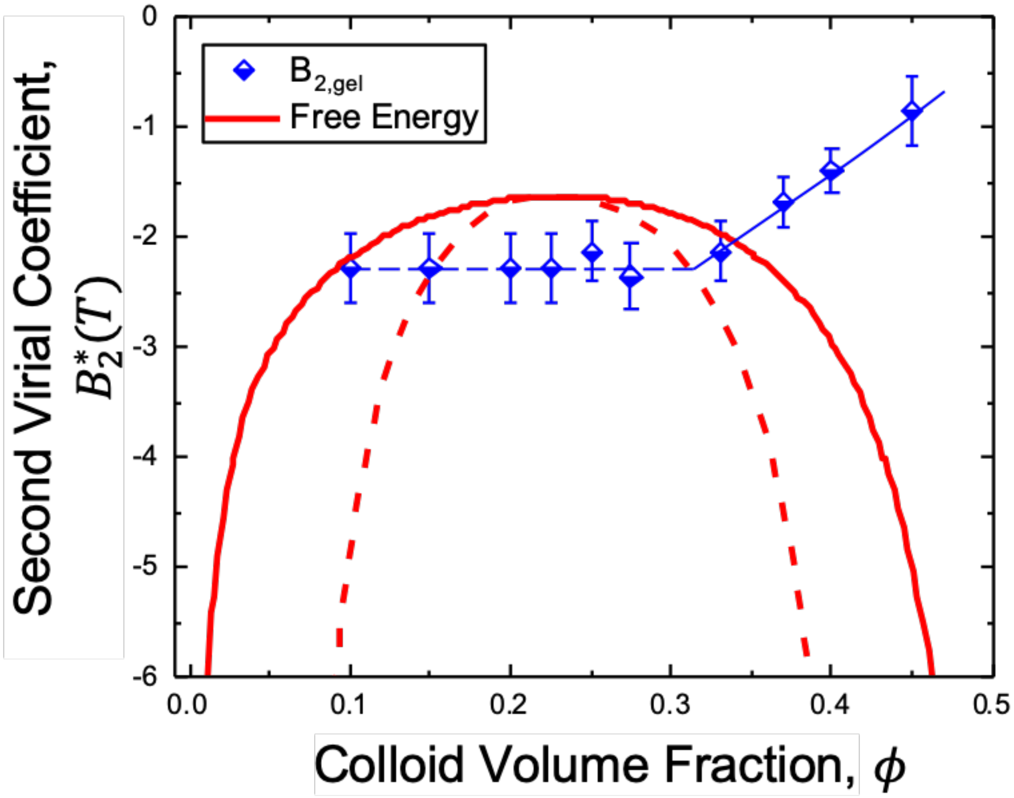

Figure 4.5: Overlay of experimentally determined locus of minimum gelation temperature (corresponding to maximum second virial coefficients) to mean field predictions developed in the current chapter. Experimental points are determined as described in association with Figure 4.4, with error bars reflecting the step size in temperature taken to determine the boundary.

towards. In what follows we develop a spectroscopic technique by which the boundaries can be more clearly determined, achieved through sedimenting the gel.

4.5 Interrogating colloidal volume fractions through NMR spectroscopy

The measurable quantity we are interested in through phase mapping is simply: what is the colloidal volume fraction ϕ of the strands and voids in our arrested gel? The strands comprise tens of aggregated nanoemulsions, whereas the voids are filled with scarce nanoemulsions in a bulk continuum fluid. To answer this question, we turn to NMR spectroscopy as a technique to unambiguously and quantitatively measure chemical composition. Characterizing the oil fraction in nanoemulsion samples requires that we examine the relevant chemical species in the material system, as shown in Figure 4.6.

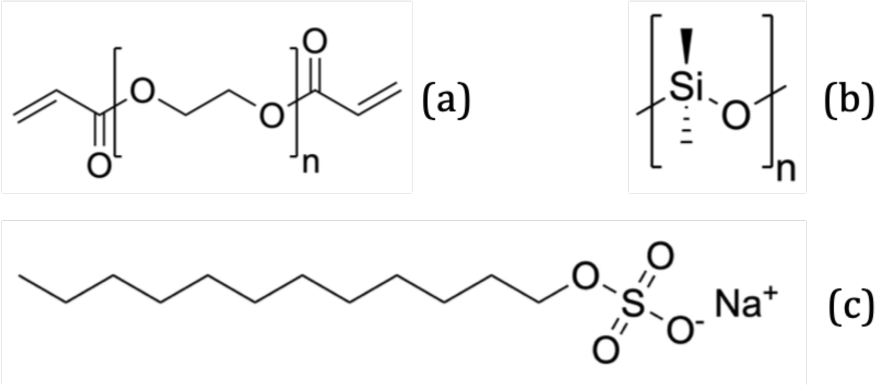

Figure 4.6: Chemical structures of relevant species, including (a) PEGDA, (b) Silicone oil, and (c) SDS surfactant

For a fixed formulation of thermoresponsive nanoemulsion with known input volume fractions of polymer and oil, we can calculate the molar ratio of oil to polymer, $R_{oil/polymer}$. Generally, the number of moles n_i of component i for a known volume V_i is calculated from the density ρ_i and molecular weight $M_{W,i}$ of that component.

$$n_i = \frac{V_i \rho_i}{M_{W,i}} \tag{4.5}$$

Consequently, the molar ratio of oil to polymer is given by

$$R_{oil/polymer} = \frac{V_{oil}\rho_{oil}/M_{W,oil}}{V_{polymer}\rho_{polymer}/M_{W,polymer}} \tag{4.6}$$

Using the experimental formulation parameters for nanoemulsion synthesis, namely ϕ as the volume fraction of oil in the entire volume V such that $V_{oil} = V\phi$ and P as the volume fraction of polymer in the non-oil volume such that $V_{polymer} = V(1-\phi)P$, the calculation of the molar ratio based on known input volume fractions is then

$$R_{oil/polymer} = \frac{\phi\rho_{oil}/M_{W,oil}}{(1-\phi)P\rho_{polymer}/M_{W,polymer}} \tag{4.7}$$

Because the intensity of NMR signal at a given chemical shift is directly proportional to the number of nuclei contributing to that signal, an equivalent expression for the molar ratio is

$$R_{oil/polymer} = \frac{I_{oil}/Z_{oil}}{I_{polymer}/Z_{polymer}} \tag{4.8}$$

where I_α is the integrated signal intensity associated with species α and Z_α is the number of protons (i.e. hydrogen atoms) per molecule of species α. Additionally critical to this analysis is that the chemical shifts that identify each species do not overlap. For the PEGDA polymer, the distinguishing proton environment is the acrylate end group $-\mathrm{CO}-\mathrm{CH}=\mathrm{CH_2}$ which contributes $Z_{polymer} = 6$ protons to its signal. The chemical shift range for acrylate signal occurs in the $6.4 - 5.8$ ppm range.

For the PDMS oil, there is only one proton environment throughout the linear chain

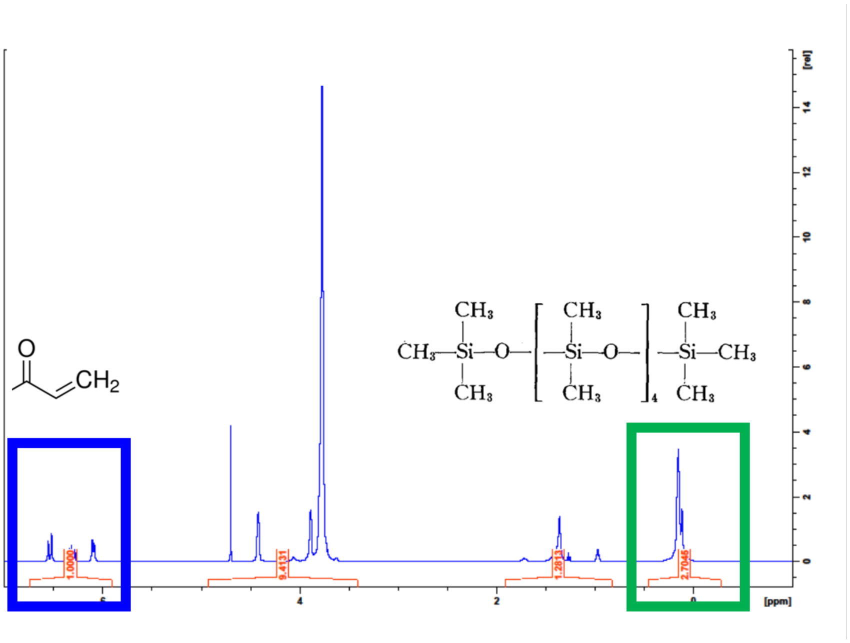

Figure 4.7: NMR spectrum for deuterated nanoemulsion to identify the molar ratio of oil to polymer via integrated intensities and Equation (4.8). The integrated intensity of the acrylate peaks (boxed in blue) is set to 1 as reference, and here the relative signal from the methyl protons (boxed in green) is 2.7045. the unboxed signals in the spectrum are associated with the ethylene oxide backbone and the surfactant proton environments.

in the form of the Si——CH_3 group. The chemical shift for the methyl environment signal occurs in the $0.1 - 0.0$ ppm range. Based on the known molecular weight of the silicone oil, we can determine the number of contributing protons using the formula

$$Z_{oil} = 18 + 6n \tag{4.9}$$

where 18 is the number of protons on the polymer chain ends, 6 is the number of protons per polymer repeat unit, n is the number of polymer repeat units. The average number of polymer repeat units can be calculated based on the known molecular weight of the silicone, $795\,\mathrm{g\,mol^{-1}}$. Consequently, we find that $Z_{oil} = 69$ for the oil in our system.

Altogether, the ratio of integrated NMR signal intensity for the PDMS relative to the PEGDA is measured in comparison to the known input compositions by combining

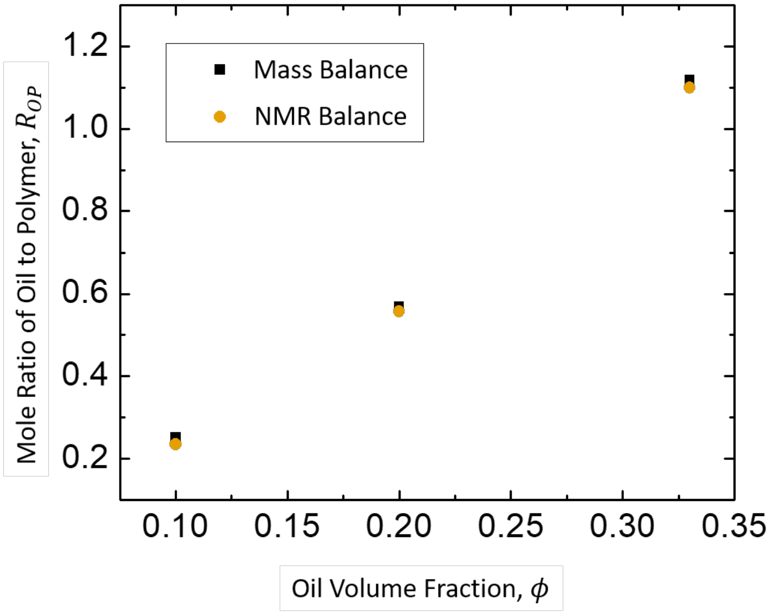

Figure 4.8: Comparison of polymer/oil molar ratio calculations based on known inputs, as in Equation (4.7), and based on integrated NMR signal intensities, as in Equation (4.8). This validation experiment is used to support usage of quantitative NMR analysis in subsequent experiments where we do not know the true volume fraction ratio of oil to polymer a priori.

Equations (4.7) and (4.8), for varying values of ϕ. Figure 4.7 shows a representative NMR spectrum for a nanoemulsions prepared at $\phi = 0.10$. Note that deuterated water is used in place of deionized water to remove the otherwise overpowering proton signal from the solvent.

By performing a control study in which a known amount of oil and polymer is formulated for a given system, we are able to validate the signal obtained via this technique. As shown in Figure 4.8, for the range of oil droplet volume fractions tested, there is very good agreement between the calculation of molar ratio based on the integrated NMR signal intensities and the known molar ratio based on input concentrations.

Moving forward, we can effectively calculate the volume ratio of oil to polymer by combining Equations (4.7) and (4.8), which leads to the design equation

$$\Phi \equiv \frac{\phi_O}{\phi_P} = \frac{I_O/Z_O}{I_P/Z_P} \times \frac{\rho_P/M_{W,P}}{\rho_O/M_{W,O}} = \frac{Z_P}{Z_O} \times \frac{I_O}{I_P} \times \frac{\rho_P}{\rho_O} \times \frac{M_{W,O}}{M_{W,P}} \tag{4.10}$$

where *oil* is abbreviated by O, and *polymer* is abbreviated by P.

4.6 Determining droplet volume fractions from centrifugation experiments

The principle by which arrested gels are separated into co-existing phases relies on centrifugation at accelerations large enough to collapse the gel but not large enough to fully separate the individual dispersed colloids. Centrifugation, and more generally sedimentation, has been observed to collapse colloidal gels and affect gelation boundaries through the introduction of a competing time scale against phase separation. [10–12] In this methodology, the relevant dimensionless group is the gravitational Péclet number given by

$$Pe_g = \frac{4\pi\Delta\rho g a^4}{3k_B T} \tag{4.11}$$

where $\Delta\rho$ is the density difference between dispersed and continuous phase, g is the centrifugal acceleration, a is the droplet radius, k_B is Boltzmann's constant, and T is absolute temperature. At rest and at room temperature, the gravitational Péclet number for the system is $\mathcal{O}\left(10^{-7}\right)$. However, upon gelation at elevated temperatures in an isothermal chamber (Innova 44) the dominant length scale of structure due to the arrested spinodal decomposition is on the order of 1 µm. With sufficient centrifuge accelerations of $9000 \times g$, the corresponding gravitational Péclet numbers are $\mathcal{O}\left(10^{-2}\right)$ based on the droplet radius but $\mathcal{O}\left(10^{3}\right)$ based on the structural length scale. Thus, at higher accelerations imposed by the centrifuge (Sorvall RC 6+), the oil droplet rich gel strands will collapse towards the surface, without causing full separation of the individual oil droplets.

Whether the two arrested gel networks — one of droplet strands and one of dilute voids — reflect equilibrium or nonequilibrium states can be inferred by comparison against the theoretically predicted equilibrium boundary. Once the two colloidal gel components are separated by centrifugation, the component with fewer oil droplets (thus denser overall) can be syringed out of the bottom of the vial, leaving the upper gel layer with more oil droplets (thus less dense overall). In this separation, we are left with four unknown quantities: the two volume fractions of oil and polymer in the two layers, top and bottom. The conservation equations we have to balance the system are given by

$$\begin{aligned}
\phi_{O,total} V_{total} &= \phi_{O,top} V_{top} + \phi_{O,bottom} V_{bottom} \\
\phi_{P,total} V_{total} &= \phi_{P,top} V_{top} + \phi_{P,bottom} V_{bottom} \\
\Phi_{top} &= \frac{\phi_{O,top}}{\phi_{P,top}} \\
\Phi_{bottom} &= \frac{\phi_{O,bottom}}{\phi_{P,bottom}}
\end{aligned}$$

where Φ is the molar ratio of oil to polymer as determined from integrated NMR signal intensities. With four linear equations, we can easily solve for the desired quantities and determine the volume fraction of oil in each layer. The values that are known or measured include the total initial composition and volume ($\phi_{O,total}, \phi_{P,total}$, and V_{total}), the final volume of each phase V_{top} and V_{bottom}, and the molar ratios as determined by

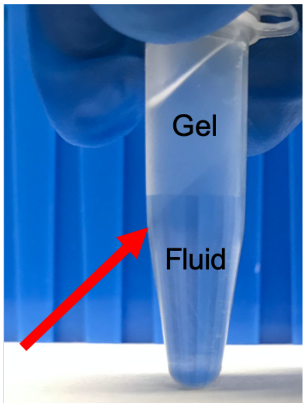

Figure 4.9: Image of 1.5 mL tube with sample after centrifugation, showing a clear separation line between the oil droplet rich (less dense) gel phase on top and the oil droplet lean (more dense) fluid phase on bottom. By extracting the fluid phase from the lower portion, we are able to determine separate oil droplet compositions as outlined in this chapter.

NMR signal intensities using Equation (4.10), Φ_{top} and Φ_{bottom}.

$$\begin{aligned}
\phi_{O,top} &= \frac{-V_{total}}{V_{top}} \times \frac{\phi_{P,total} - \phi_{O,total}\Phi_{bottom}^{-1}}{\Phi_{bottom}^{-1} - \Phi_{top}^{-1}} \\
\phi_{O,bottom} &= \frac{V_{total}}{V_{bottom}} \times \frac{\phi_{P,total} - \phi_{O,total}\Phi_{top}^{-1}}{\Phi_{bottom}^{-1} - \Phi_{top}^{-1}} \\
\phi_{P,top} &= \phi_{O,top}\Phi_{top}^{-1} \\
\phi_{P,bottom} &= \phi_{O,bottom}\Phi_{bottom}^{-1}
\end{aligned}$$

Thus, to proceed, we prepare nanoemulsions of known initial composition and arrest them at varying temperatures. Once arrested for 30 minutes, the gels undergo a sedimentation acceleration of $9000 \times g$ in a temperature-controlled centrifuge for 20 minutes. The acceleration magnitude was chosen to sediment the gel phase but not the droplets, as described previously based on the gravitational Péclet number. [8] The separation line is visible macroscopically, as shown in Figure 4.9.

Afterwards, the subnatant is separated from the supernatant using a syringe. The separated colloidal phases are characterized via solution-state NMR spectroscopy, diluted in deuterated water to facilitate loading into the NMR sample tubes while still preserving the molar ratio of oil to polymer.

4.7 Results and comparison to theory

The results of the sedimentation experiments in combination with the mean-field predictions from perturbation theory are presented in Figure 4.10, building from the gel line developed through Figure 4.5. Given the limited number of studies that are able to combine predicted and measured colloidal phase behavior, we emphasize that these results tie together our understanding of both .

We find that the experimentally determined phase envelope agrees very well with the mean field theoretical prediction, with the most noticeable deviation at the shallowest quench. Such a deviation is not surprising because a mean-field model as we have used will become less accurate near the critical point due to density fluctuations. Additionally, the polydispersity of the experimental system is not accounted for in the theoretical model. Polydispersity has been shown to stabilize a wider range of droplet volume fractions and suppress the phase separation envelope. [13] The closest agreement is seen at moderate quenches, with experimental points tracking the predicted binodal to within $\Delta\phi \sim 0.02 - 0.03$. That the experimental points consistently under-predict the binodal may reflect the limitations of the sedimentation process in fully separating the viscoelastic gel strands.

At sufficiently deep quenches, we also observe a modest but clear decrease in the dense volume fraction. This trend reversal is opposite to the direction of the binodal with increasing quench depth and supports an increased susceptibility of dense gel strands to not reflect equilibrium boundaries, similar to the observations made in arrested protein systems. [8] The droplet growth instability of the nanoemulsion system at temperatures below the deepest quenches precluded further interrogation.

In its entirety, we argue that Figure 4.10 presents a comprehensive picture of gelation and phase separation for a single model colloidal gel, with the near-equilibrium sedimentation experiments and mean-field theory agreeing to a reasonable degree.

4.8 Comparison to coarse-grained simulations

Recent simulation work has also investigated the effect of sedimentation forces on arrested colloidal gels. [14] In their work, Padmanabhan and Zia find that the mechanism of gel collapse is due to a negative osmotic pressure inside the gel, and thus the gravitational field is sufficient to collapse the gel strands and determine a dense droplet volume fraction. As their work shows, the droplet rich phase exhibits a final volume fraction that is quench dependent (cf. Figure 4 in [14]). They observe a decrease in the droplet rich phase volume fraction ϕ_L with increasing quench depth from $5k_BT$ to $6k_BT$ that is reminiscent of the trend we see at the deepest quenches in our study.

A direct quantitative comparison between sedimentation simulations and the experimental measurements is also provided in Figure 4.10, with simulations implemented in line with the published work from Padmanabhan and Zia. These molecular dynamics simulations employ a qualitatively different short-ranged potential by way of a Morse potential as opposed to the two-Yukawa potential proposed in Chapter 3, but the B_2^* values are equivalent and thus allow for quantitative comparison by the law of corresponding states. [15] Additionally, as in their prior work the gel is freely draining and subjected to a sedimentation force to induce collapse. [14] To accurately compare their simulation with our data, the gravitational Péclet number and reduced second virial coefficient are matched accordingly. As the figure shows, the simulation data similarly shows excellent agreement with the mean field predictions and thus with the experimental data, with

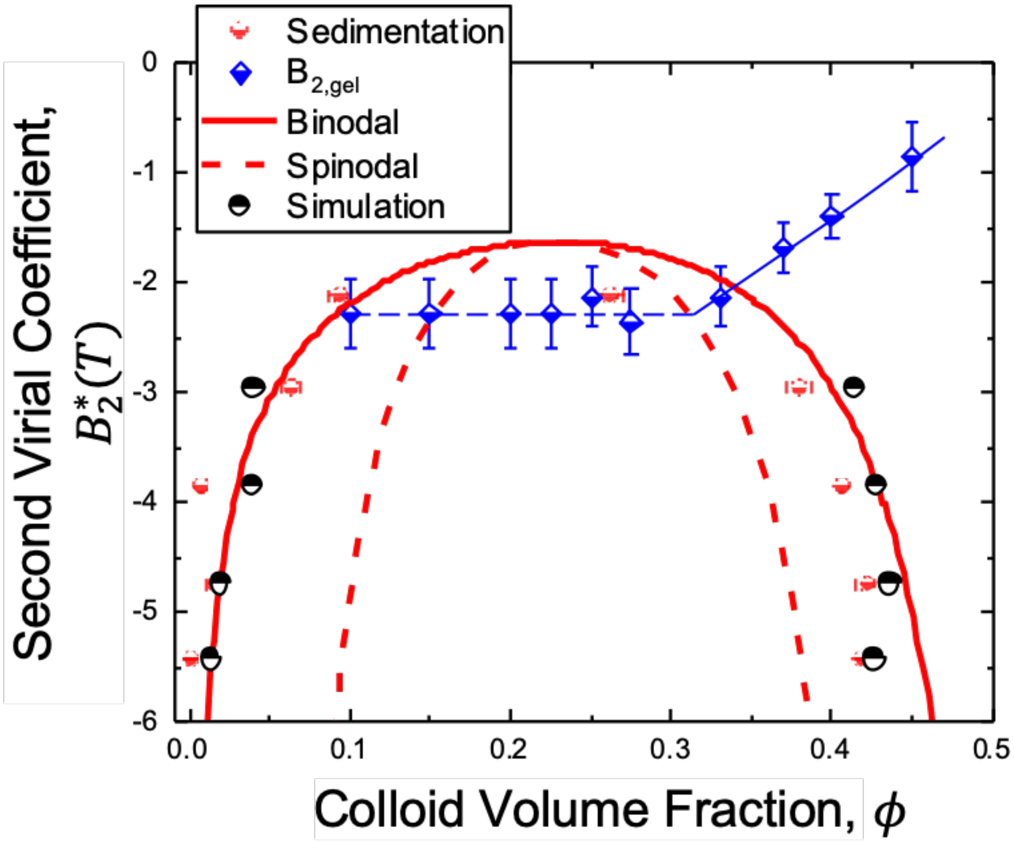

Figure 4.10: Comparison of experimentally determined phase envelope (red points) to mean field predictions (red lines) developed in the current chapter. Also shown is the gel arrest line as determined through Figure 4.5. Experimental determination of phase envelope is based on centrifugation experiments. Error bars represent standard deviations from triplicate samples as well as varying initial colloidal volume fractions before quench. Molecular dynamics simulations are achieved through sedimentation of gels formed with at an equivalent effective temperature and gravitational Péclet number, following the techniques of Padmanabhan and Zia. [14]

further similarities seen at the deepest quench regarding the apparent intersection of the glassy arrest line.

4.9 Conclusions

In this section, we have developed mean field theoretical predictions for the equilibrium phase envelope of colloidal phase separation that underlies the non-equilibrium arrest observed in the thermoresponsive nanoemulsion system. We find that the predicted region of phase instability agrees reasonably well with experimental efforts to the same end. Furthermore, the measured gelation boundary lies significantly within the phase instability boundary, suggesting that the two processes are highly coupled in the system. This aspect of the system's colloidal gelation will prove pertinent to interpreting further observations. With evidence from this chapter in support of the equilibrium piece of the larger picture, in the subsequent chapter we will turn to considering the kinetic descriptions of non-equilibrium transitions in the colloidal gel.

Bibliography

[1] C. Tejero, A. Daanoun, H. Lakkerkerker, and M. Baus, "Isostructural solid-solid transition of (colloidal) simple fluids," *Physical Review E*, vol. 51, no. 1, p. 558, 1995.

[2] M. S. Wertheim, "Exact solution of the percus-yevick integral equation for hard spheres," *Physical Review Letters*, 1963.

[3] F. Del Rio, E. Avalos, R. Espindola, L. F. Rull, G. Jackson, and S. Lago, "Vapourliquid equilibrium of the square-well fluid of variable range via a hybrid simulation approach," *Molecular Physics*, vol. 100, no. 15, pp. 2531–2546, 2002.

[4] Y. Gao, J. Kim, and M. E. Helgeson, "Microdynamics and arrest of coarsening during spinodal decomposition in thermoreversible colloidal gels," *Soft Matter*, vol. 11, no. 32, pp. 6360–6370, 2015.

[5] P. D. Godfrin, P. Falus, L. Porcar, K. Hong, S. D. Hudson, N. J. Wagner, and Y. Liu, "Dynamic properties of different liquid states in systems with competing interactions studied with lysozyme solutions," *Soft matter*, vol. 14, no. 42, pp. 8570–8579, 2018.

[6] C. Rueb and C. Zukoski, "Viscoelastic properties of colloidal gels," *Journal of Rheology*, vol. 41, no. 2, p. 197, 1998.

[7] A. P. Eberle, R. Castaneda-Priego, J. M. Kim, and N. J. Wagner, "Dynamical arrest, percolation, gelation, and glass formation in model nanoparticle dispersions with thermoreversible adhesive interactions," *Langmuir*, vol. 28, no. 3, pp. 1866–1878, 2012.

[8] F. Cardinaux, T. Gibaud, A. Stradner, and P. Schurtenberger, "Interplay between

Spinodal Decomposition and Glass Formation in Proteins Exhibiting Short-Range Attractions," *Physical Review Letters*, vol. 99, p. 118301, sep 2007.

[9] H. H. Winter and F. Chambon, "Analysis of Linear Viscoelasticity of a Crosslinking Polymer at the Gel Point," *Journal of Rheology*, vol. 30, no. 2, p. 367, 1986.

[10] C. Allain, M. Cloitre, and M. Wafra, "Aggregation and sedimentation in colloidal suspensions," *Physical review letters*, vol. 74, no. 8, p. 1478, 1995.

[11] A. Bailey, W. C. K. Poon, R. J. Christianson, A. B. Schofield, U. Gasser, V. Prasad, S. Manley, P. N. Segre, L. Cipelletti, W. V. Meyer, *et al.*, "Spinodal decomposition in a model colloid-polymer mixture in microgravity," *Physical review letters*, vol. 99, no. 20, p. 205701, 2007.

[12] J. M. Kim, J. Fang, A. P. Eberle, R. Castañeda-Priego, and N. J. Wagner, "Gel transition in adhesive hard-sphere colloidal dispersions: The role of gravitational effects," *Physical review letters*, vol. 110, no. 20, p. 208302, 2013.

[13] S. M. Liddle, *Polydispersity effects on colloidal phase transitions and kinetic arrest*. PhD thesis, University of Edinburgh, 2014.

[14] P. Padmanabhan and R. Zia, "Gravitational collapse of colloidal gels: non-equilibrium phase separation driven by osmotic pressure," *Soft matter*, vol. 14, no. 17, pp. 3265–3287, 2018.

[15] M. G. Noro and D. Frenkel, "Extended corresponding-states behavior for particles with variable range attractions," *The Journal of Chemical Physics*, vol. 113, no. 8, pp. 2941–2944, 2000.

Chapter 5

Sequential transitions in arrested phase separation colloidal gels

Having considered the equilibrium phase behavior and nonequilibrium gelation transition as general state transformations of the thermoresponsive nanoemulsion system, in this chapter we begin an experimental investigation into the kinetic processes that occur en route to colloidal gel arrest. The pertinence of this analysis is made evident through a simple kinetic comparison of gelation inside and outside of the phase coexistence region. To address the kinetics inside the phase envelope, we employ rheo-microscopy as a characterization technique to simultaneously track the linear viscoelastic rheology and structure formation during the arrested phase separation process. Ultimately, we are able to develop a kinetic processing diagram in the form of a time temperature transformation diagram to summarize the sequence of colloidal gel evolution. We are also able to make comparisons to molecular dynamics simulations implemented in colloidal gel literature. For this study, we focus on a single thermoresponsive nanoemulsion formulation where $\phi = 0.33$, $P = 0.33$, and $C_S = 200\,\text{mM}$, where formulation parameters are described in Chapter 2. As such, the phase diagram in Figure 4.5 provides an equilibrium road map for probing into the two phase region.

5.1 Motivating thermal processing strategies

Imparting desirable properties to engineered materials requires processing strategies that recognize the microstructural transformations accessible by the system. Thermo-temporal processing is a ubiquitous strategy across a wide range of systems – including metal alloys, ceramics, and polymer blends – due to the relative ease of tuning protocols for heating and aging a material. [1–3] Generally, through thermo-temporal processing the material system is quenched into a region of phase instability, which subsequently undergoes either spinodal decomposition or glassification and coarsens to a desired microstructure over time as density fluctuations grow until they are arrested at a desired scale. [4] Control over these microstructural length scales can influence final mechanical properties such as elasticity and yield stress. [5, 6]

Colloidal systems, however, have to date not fit into this thermo-temporal paradigm due to challenges in dynamically tuning interaction strength to navigate the spinodal region. For example, colloidal gels formed through concentration-dependent depletion attractions have been shown to exhibit a phase instability and subsequent gelation, but dynamically tuning the effective interaction strength, by either introducing or removing depletant, will tend to disrupt any nascent gel formation. [7, 8] In systems where thermo-reversible colloidal gelation has been observed, few model systems are available that provide access to the rich structural transformation of phase instability. For well-studied systems such as brush-coated silica, for example, gelation occurs far prior to the emergence of phase instability, thus limiting the ability to tune the resultant arrested gel. [9–11]

More recently, colloidal systems which gel due to thermoreversible bridging of nanoemulsions have shown promise for experimentally realizing thermo-temporal processing, with their attractions effectively described by a temperature-dependent square well depth. [12, 13] As discussed in earlier chapters of this thesis, improvements can be made to our understanding of gelation relative to the equilibrium phase space. Additional progress has been made which shows that the system can be leveraged with processing schemes including 3D printing and sequential temperature jumps. [14] Although attempts at complex thermal processing have been made in recent work, [15] these forays were made without an understanding of the interaction potential, phase diagram, and kinetics to guide the choice of quench depths and rates. Thus, we seek a founded understanding for thermal processing in this chapter. Variations in quench rate have demonstrated qualitative differences in linear viscoelastic features, [16] but through this study we aim to attain more insight into the specific sequence of transitions. Furthermore, we determine the kinetic window during which colloidal gel structure is formed yet thermally malleable, thus identifying opportunities for subsequent materials processing strategies. These results cast light onto the prevailing view that

5.2 Kinetic comparison of spinodal decomposition and glassy arrest

In the thermoresponsive nanoemulsion system, gelation can occur through qualitatively different mechanisms as a result of processing relative to the equilibrium phase envelope. As Figure 4.10 shows, at sufficiently high colloid volume fractions above $\phi \sim 0.35$, temperature quenches fall outside the phase instability window and are instead described by attractive glass kinetics. The demarcating features of this transition include changes to the formation and aging of elasticity. [17]

We can use linear viscoelastic rheology to observe this mechanical feature if we compare two isochoric quenches — one at $\phi = 0.25$, well within the phase boundary, and the other at $\phi = 0.40$, to the right of the phase boundary. As Figure 5.1 shows, the development of elastic-dominated mechanical behavior is qualitatively different for the glassy system at $\phi = 0.40$, in which elasticity continues to grow unbounded during isothermal aging. In contrast, the phase separated system at $\phi = 0.25$ exhibits an induction time during which phase separation proceeds, followed eventually by arrest and emergence of the colloidal network structure. That the different gelation mechanisms give rise to different gelation kinetics is already a means of tuning gel behavior in the system by navigating the possible transitions. This serves as an extension of prior studies into thermoresponsive nanoemulsions, which similarly showed that gelation at more dilute volume fractions can result in homogeneous gelation via percolation as opposed to heterogeneous gelation via arrested phase separation, resulting in clear and measurable differences in elastic modulus and yield stress scaling. [18]

The importance of kinetics for arrested phase separation gels is further emphasized in a fuller study of the arrest time scales. By tracking the age time at which the elastic moduli cross over (i.e. the transition from viscous-dominated to elastic-dominated rheology) for varying quench depths and rates, we can see the consequences of thermal processing conditions on gelation (summarized in Figure 5.2). Figure 5.2(a) shows that the as the quench depth is varied for fixed quench rate for quenches within the phase coexistence region, gelation occurs systematically faster with deeper quenches. In contrast, Figure 5.2(c) shows that for $\phi = 0.40$, the gelation time is essentially insensitive to the quench depth, meaning that the transition is more so induced by simply crossing the minimum gelation temperature. Similarly, Figure 5.2(d) shows that at a fixed quench depth for the denser volume fraction, faster quenches result in faster arrest. This result is

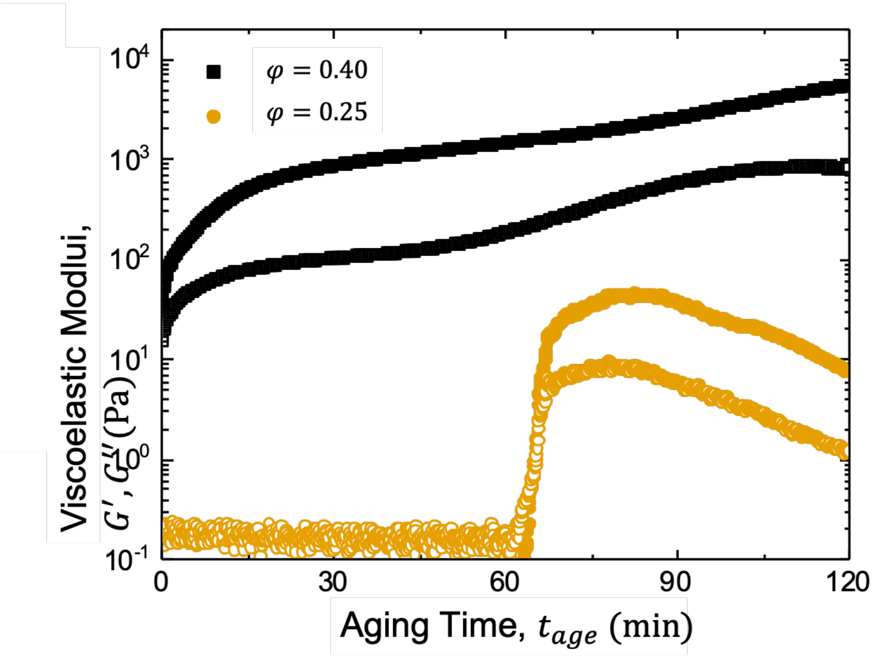

Figure 5.1: Comparison of linear viscoelastic rheology inside and outside the phase envelope. In both cases we quench the suspension to a final temperature above the minimum gelation temperature and allow isothermal aging to proceed. For the $\phi = 0.40$ system outside the phase envelope (black), elasticity grows steadily over time reflecting glassy aging. For the $\phi = 0.25$ system well inside the phase envelope (gold), there is an induction period before elasticity emerges, and the continued aging results in weakening of the gel structure.

again consistent with the physical picture of arrest outside of the phase envelope proceeding due to crossing a threshold temperature for glassy arrest, since faster quenches will naturally cross the minimum gelation temperature sooner. That the $\phi = 0.25$ gelation kinetics in Figure 5.2(b) are relatively constant with quench rate shows how the quench depth is the dominant variable that affects arrest kinetics. Similar exponentially decaying quench kinetics have been observed in microgel and protein systems when attractions are changed by polymer or protein loading concentrations as opposed to changing temperature. [19, 20]

As a result of the quench dependent behavior seen in the arrested phase separation gels, we move on to characterize the detailed sequence of kinetic transitions and gel

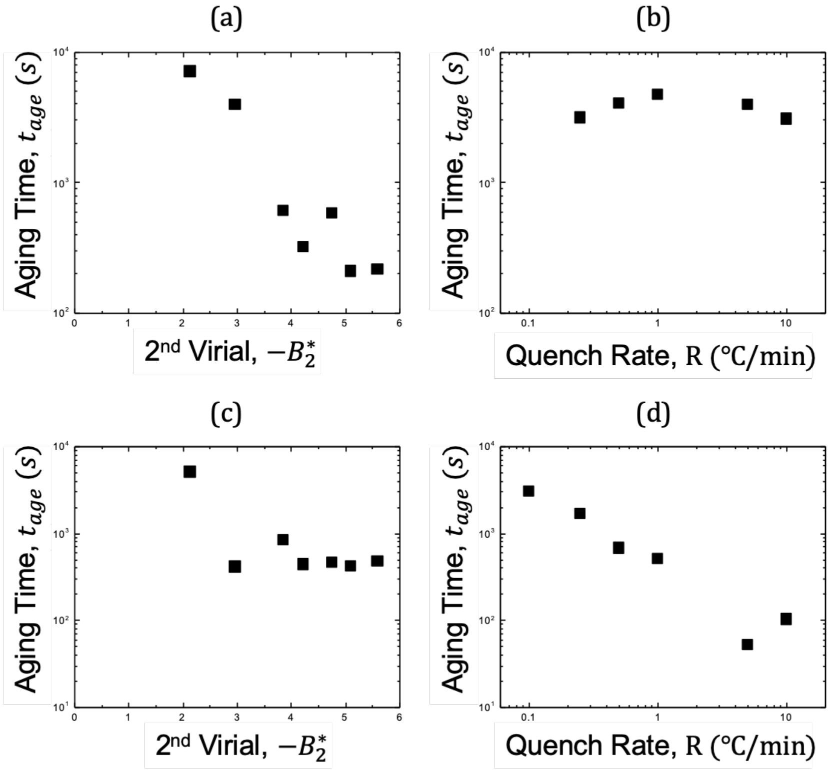

Figure 5.2: Comparison of aging kinetics inside and outside the phase envelope. For $\phi = 20\%$ (a) kinetics inside the phase envelope show a clear dependence on quench depth, with deeper quenches resulting in faster gelation (b). For $\phi = 40\%$ (c) kinetics outside the phase envelope show that gelation and arrest are nearly simultaneous and (d) gelation time speeds up with faster quenches, reflecting a faster crossing of the minimum gelation temperature.

formation that occur through the process of gelation and deep arrest.

5.3 Time temperature transformation diagrams

The processing framework we employ to better understand the kinetic transitions in the colloidal gel system is through time temperature transformation (TTT) diagrams. Also known as isothermal transformation diagrams, TTT diagrams were originally developed to describe the kinetic transitions in metallic alloy processing. [21] Generally, they consider a material system of fixed composition that undergoes structural transi-

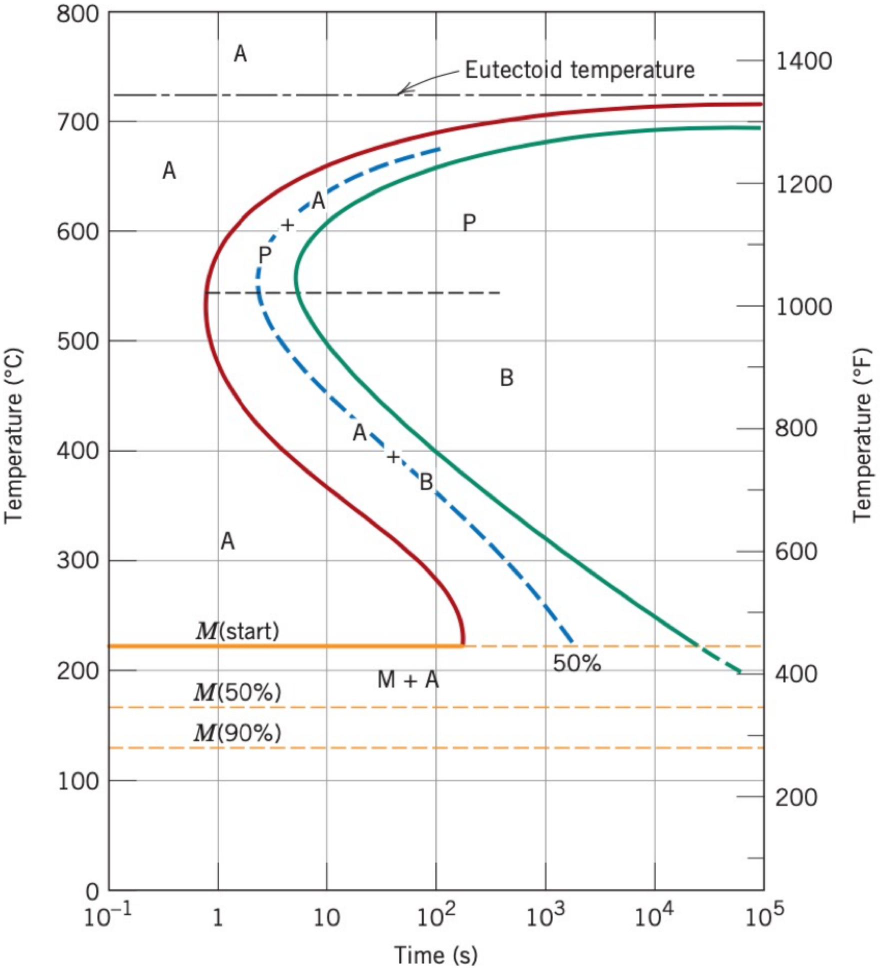

Figure 5.3: Iron-Carbon time temperature transformation diagram, adapted from Callister and Rethwisch. [21] The eutectoid temperature denotes the upper bound of the two-phase region, with A signifying the austenitic structure, P the pearlitic structure, B the bainitic structure, and M the martensitic structure. This diagram is used to illustrate the qualitative features of transformation boundaries in TTT diagrams.

tions due to thermal processing. In solid-state systems, these diagrams are typically arrived at empirically through measured logistic growth of structural transformation as a function of time, modeled with the Johnson-Mehl-Avrami-Kolmogorov Equation to capture the extent of transformation. [22] The axes in TTT diagrams plot time on the abscissa axis and temperature on the ordinate axis, as illustrated in Figure 5.3. As the system undergoes sequential transitions at constant temperature, it crosses over successive temporal boundaries, often exhibiting a non-monotonic “C” shaped curve. [21] The non-monotonicity of the boundary with varying quench has been attributed to so-called solute drag effects at deep quenches, with the quench depth of the nose bearing relation to the minimal cooling rate for equal phase formation. [23, 24]

The applicability of isothermal transformation analysis is also seen in non-metallic systems such as thermally-cured epoxy polymers. Polymeric isothermal transformation diagrams have been reported which delineate their curing, gelation, and vitrification transitions [25] or alternatively their isotropic to liquid crystalline transitions. [26] In either case, the TTT framework facilitates the design of thermal processing by rationalizing sequential transformations across a range of controlled temperature quenches. In what follows, we seek to test the applicability of the TTT framework to colloidal gels vis-à-vis the thermoresponsive nanoemulsion system.

5.4 Characterizing transitions in a thermoresponsive colloidal gel

Because our thermoresponsive colloidal gel system does not exhibit transitions identical to binary alloys nor pure polymer melts, a qualitative characterization of the various structural and mechanical states through which it evolves is needed. For this, we use both structural and mechanical signals to identify these transitions, employing both linear viscoelastic rheology to capture the mechanical gel transition and microscopic observations using optical microscopy to capture structural coarsening.

A snapshot of the rheological and structural data obtained during a rheo-microscopy experiment is provided in Figure 5.4, which gives way to the various features of gelation that can be extracted and summarized with an isothermal transformation diagram.

The rheological data reflects the linear viscoelastic moduli, from which three key transitions are observed. First, the crossover from liquid dispersion to elastic-dominated gel is marked by the crossover of G' and G''. Once the initial network is formed, we later see a second upturn in both moduli, which can also be observed as a local peak in the phase angle, $\delta = \tan^{-1} \dfrac{G''}{G'}$. Finally, the deep arrest is observed somewhat as the rheological plateau in moduli, which later will be shown to correspond to microscopic structural arrest. At these latest times, the visible bicontinuous structure is apparently static over time.

To summarize, we observe three features in the rheological and structural signals that reflect temporal events during colloidal gelation: (1) mechanical gelation, which we call t_G to reflect the equivalence of G' and G''; (2) rapid structural coarsening, which we call t_δ to reflect the local peak in $\tan \delta$; and (3) prolonged structural arrest of microscopic length scales, which we call t_L.

5.5 Isothermal transformation diagram – Results

Isothermal aging experiments can be conducted systematically for varying quench depths into the spinodal region, using the phase diagram of Figure 4.5 as a guide for relative quench depth along the axis of effective temperature. The resultant TTT diagram is presented in Figure 5.5 with data points colored identical to the indications in Figure 5.4. Transition points are not marked for times before 100 s because the temperature ramp from room temperature to final quench temperature is still ongoing; as such, the onset of the transition at such short times is ill-defined in thermodynamic state space. Specifically, for the deepest quenches below $B_2^* < -3.5$, the mechanical gelation crossover happens during the temperature ramp and thus cannot be clearly interpreted as an isothermal aging period.

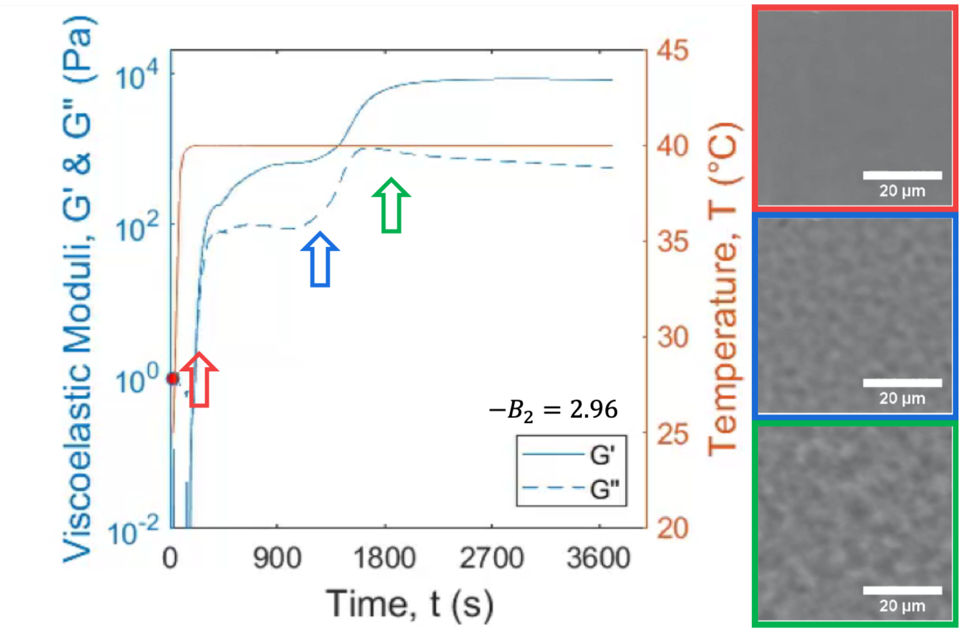

Figure 5.4: Isothermal linear viscoelastic rheology is used to observe colloidal gel transitions during aging. Aging occurs following a temperature ramp inside the spinodal region, with small amplitude oscillatory strain amplitude $\gamma = 0.1\%$ and $\omega = 10\,\mathrm{rad\,s^{-1}}$. Indicated in red is t_G, the incipience of gelation following solution behavior is determined from the crossover of the storage modulus G' and loss modulus G'', after which the elastic storage behavior dominates the material response. Microstructural signal is not resolvable at this time. The blue arrow identifies t_δ, the upturn in moduli corresponding to the appearance of optically resolved texture which grows and eventually plateaus over time. In green is t_L, the plateau of viscoelastic moduli corresponds to an apparent arrest of the microstructural length scale L_c.

Notwithstanding the limitations at early aging times, we can make several observations about the sequence of transitions during colloidal gelation. First, the particular sequence of an emergence of elasticity followed by delayed coarsening and then deep arrest is preserved across varying quenches. If these events were independent we might expect the sequence to change such that we would observe a region of processing where the signatures of coarsening and arrest appear prior to mechanical gelation, reflecting pure liquid-liquid phase separation. Although it remains a possibility that such a region exist outside the quenches depths reported here, the trends do not suggest an approach towards crossover.

We observe a logarithmic dependence of t_G with respect to B_2^*. Alternatively, this time dependence can be thought of as an exponentially decaying dependence of t_G with respect to increasing quench depth. Such kinetics are consistent with a Kramers-type process for gel formation, which posits escape from the attractive well to be the rate-determining step for configurational diffusion of the system, and which also predicts a rate that decreases exponentially with increasing temperature. [27] In fact, the RLCA-like aggregates that we would expect to see as a result of these kinetics have been observed previously for thermoresponsive nanoemulsions at similar volume fractions. [18]

Another remarkable feature of these colloidal gelation kinetics is the time difference between t_G and t_δ. This induction time — ranging from several hundred to several thousand seconds — raises many questions about the precise mechanism that triggers the onset of rapid coarsening, as well as what relation (if any) does it hold to the initial mechanical gel network formation. We anticipate future simulations of the gelation process will be able to better resolve these particle-scale mechanisms.

The other transitions, t_δ and t_L, exhibit similar trends with respect to quench depth but are both not easily described by a purely logarithmic dependence. Interestingly, the current data suggest an approach towards the nose of a potential "C" shaped region for the deepest quenches. Similar shapes have been reported in polymeric TTT diagrams for so-called "gelled-glass" regions. [25, 26] Similar to atomic and molecular systems, the TTT nose may reflect hydrodynamic drag effects on a colloidal scale that arise above sufficiently fast quench rates. [24]

To our knowledge, this is the first isothermal diagram reported for a thermoresponsive colloidal gel. As a point of comparison, we consider thermally cured epoxy polymers, which exhibit transitions to rubbery or glassy states. Similar to our current observations, the sequence of processes is typically preserved across quenches. Discontinuities in the sequence of transitions are mainly observed across the glass transition temperature T_g,

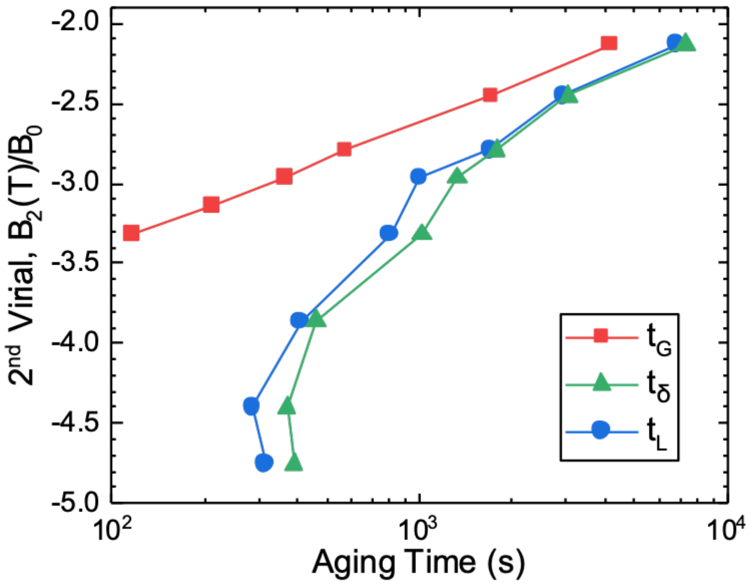

Figure 5.5: Summary of time temperature transformations of thermoresponsive colloidal gel over time, for varying quenches into the spinodal region as indicated by reduced second virial coefficient. Nanoemulsion is composed of $\phi = 0.33$ droplets, $P = 0.33$ volume fraction PEGDA polymer, and 200 mM surfactant.

across which it is reasonable to expect significantly different mobility values for aging materials. In the colloidal gel system, we are well above the glass transition temperature of the short-chained bridging PEGDA polymer. The minimum gel temperature, as delineated in Chapter 4, provides a similar discontinuity for quenches that are outside the phase envelope.

5.6 Comparison to molecular dynamics simulations

Using molecular dynamics simulations, we can interrogate similar sequence transitions during colloidal formation. The simulation results reported here are implemented in line with previous work by Padmanabhan and Zia, specifically using a Morse potential with reduced second virial coefficient matching the two-Yukawa model. [28–30] The simulations were performed using the LAMMPS software package and $750,000$ Brownian particles in an implicit solvent to capture the continuous phase fluid. [31]

To properly nondimensionalize the system for comparative study, we make use of the second virial coefficient again such that we can compare our two Yukawa potential with the Morse potential implemented in simulation. [29] However, the characteristic time scale is not immediately clear given that we do not expect the Brownian time based on a single nanodroplet to dominate during the entire gelation processes, which involve the emergence of hindered diffusion.

To nonetheless produce a quantitative comparison, we can plot the ratio of time scales as observed in both experiment and simulation. In experiment, we take the ratio of time for prolonged structural arrest to the time for mechanical gelation

$$T_{L/G} \equiv \frac{t_L}{t_G} \tag{5.1}$$

where, as described earlier, the prolonged structural arrest is determined from the onset of nearly static microscopic structure.

Analogously, from molecular dynamics simulations of colloidal particles with effective attractions, we take the ratio of time of a change in power law growth of the dominant length scale to the time for viscoelastic moduli crossover, with the assumption that this change in power law growth reflects a qualitative change in growth regimes. Figure 5.6 shows the ratios as computed from experiment and simulation. We observe similar trends with respect to increasing quench depth, with deeper quenches resulting in an increased ratio. At sufficiently deep quenches, we are not able to resolve the ratio experimentally due to the undefined t_G that is observed prior to isothermal aging. Physically, we can understand the trend observed in both experiment and simulation by considering the competing rates of gel formation and gel arrest. That $T_{L/G}$ increases with depth means

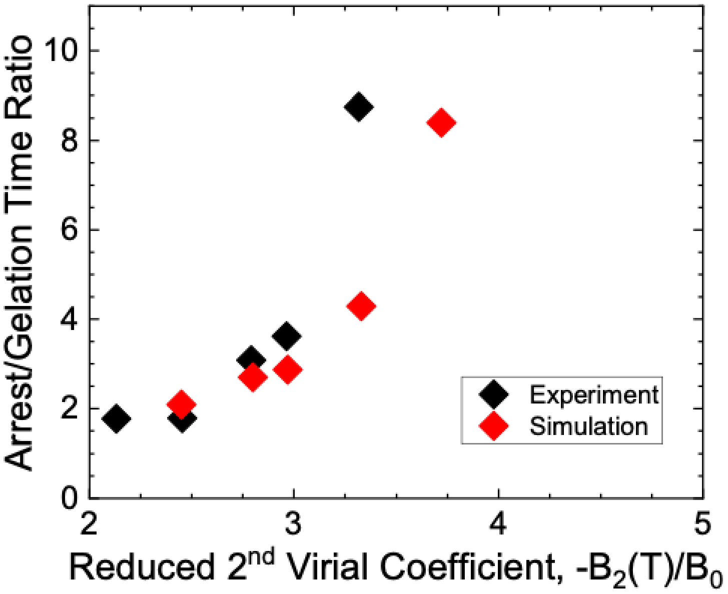

Figure 5.6: Comparison of time scale ratios between experimental aging and molecular dynamics simulations, as implemented following descriptions in [28] and [29].

that once gelation begins as marked by t_G, the kinetics associated with network formation slow down much more for deeper quenches. This slowing down is consistent with the increased strength of bonds between colloids, which would result in fewer successful attempts at bond breakage and rearrangement en route to prolonged arrest.

5.7 Conclusions

In this chapter, we have extended the isothermal transformation framework from metallic and polymeric materials to rationalize the sequence of transitions during colloidal gelation and arrest in our thermoresponsive colloidal system. We find that there is a conserved sequence of mechanical gelation, delayed yet rapid coarsening, and then prolonged deep arrest that describes isothermal aging into the spinodal region. Additionally, we are able to make a qualitative comparison to analogous molecular dynamics simulations, and we see qualitatively similar trends in the ratio of time scales with respect to quench depth. In light of prior kinetic studies of thermoresponsive nanoemulsions, we are able to rationalize the emergence or absence of variations in gel properties as a result of multi-stage processing steps. For example, the residence time at intermediate temperatures was insufficient compared to the natural induction time prior to coarsening, and thus we better understand why no significant material outcomes are observed. [15]

Overall the work in this chapter provides clear quantitative guidelines for future studies into multi-stage processing and establishes precedence for using the TTT framework to sculpt gel properties, as we will discuss over the next two chapters.

Bibliography

[1] J. E. Cahn and J. W. Hilliard, "Free Energy of a Nonuniform System. I. Interfacial Free Energy," *The Journal of Chemical Physics*, vol. 28, no. 2, pp. 258–267, 1958.

[2] C. R. McNeill and N. C. Greenham, "Conjugated-polymer blends for optoelectronics," *Advanced Materials*, vol. 21, no. 38-39, pp. 3840–3850, 2009.

[3] L. Lefebvre, J. Chevalier, L. Gremillard, R. Zenati, G. Thollet, D. Bernache-Assolant, and A. Govin, "Structural transformations of bioactive glass 45s5 with thermal treatments," *Acta Materialia*, vol. 55, no. 10, pp. 3305–3313, 2007.

[4] J. W. Cahn, "On spinodal decomposition," *Acta metallurgica*, vol. 9, no. 9, pp. 795–801, 1961.

[5] J. C. Conrad, H. M. Wyss, V. Trappe, S. Manley, K. Miyazaki, L. J. Kaufman, a. B. Schofield, D. R. Reichman, and D. a. Weitz, "Arrested fluid-fluid phase separation in depletion systems: Implications of the characteristic length on gel formation and rheology," *Journal of Rheology*, vol. 54, no. 2, p. 421, 2010.

[6] L. C. Johnson, E. Moghimi, G. Petekidis, and R. N. Zia, "Influence of structure on the linear response rheology of colloidal gels," *Journal of Rheology*, vol. 63, no. 4, pp. 583–608, 2019.

[7] W. C. Poon, "Phase separation, aggregation and gelation in colloid-polymer mixtures and related systems," *Current Opinion in Colloid & Interface Science*, vol. 3, no. 6, pp. 593–599, 1998.

[8] P. J. Lu, E. Zaccarelli, F. Ciulla, A. B. Schofield, F. Sciortino, and D. a. Weitz, "Gelation of particles with short-range attraction," *Nature*, vol. 453, pp. 499–503, May 2008.

[9] C. Rueb and C. Zukoski, “Viscoelastic properties of colloidal gels,” *Journal of Rheology*, vol. 41, no. 2, p. 197, 1998.

[10] A. P. Eberle, N. J. Wagner, and R. Castañeda-Priego, “Dynamical arrest transition in nanoparticle dispersions with short-range interactions,” *Physical review letters*, vol. 106, no. 10, p. 105704, 2011.

[11] A. P. Eberle, R. Castaneda-Priego, J. M. Kim, and N. J. Wagner, “Dynamical arrest, percolation, gelation, and glass formation in model nanoparticle dispersions with thermoreversible adhesive interactions,” *Langmuir*, vol. 28, no. 3, pp. 1866–1878, 2012.

[12] M. E. Helgeson, S. E. Moran, H. Z. An, and P. S. Doyle, “Mesoporous organohydrogels from thermogelling photocrosslinkable nanoemulsions,” *Nature Materials*, vol. 11, pp. 344–352, February 2012.

[13] Y. Gao, J. Kim, and M. E. Helgeson, “Microdynamics and arrest of coarsening during spinodal decomposition in thermoreversible colloidal gels,” *Soft Matter*, vol. 11, no. 32, pp. 6360–6370, 2015.

[14] L. C. Hsiao, A. Z. M. Badruddoza, L.-C. Cheng, and P. S. Doyle, “3d printing of self-assembling thermoresponsive nanoemulsions into hierarchical mesostructured hydrogels,” *Soft Matter*, vol. 13, no. 5, pp. 921–929, 2017.

[15] L.-C. Cheng, P. D. Godfrin, J. W. Swan, and P. S. Doyle, “Thermal processing of thermogelling nanoemulsions as a route to tune material properties,” *Soft matter*, vol. 14, no. 27, pp. 5604–5614, 2018.

[16] L. C. Hsiao and P. S. Doyle, “Celebrating soft matter’s 10th anniversary: Sequential

phase transitions in thermoresponsive nanoemulsions," *Soft Matter*, vol. 11, no. 43, pp. 8426–8431, 2015.

[17] E. Zaccarelli, "Colloidal Gels: Equilibrium and Non-Equilibrium Routes," *Journal of Physics: Condensed Matter*, vol. 19, p. 323101, aug 2007.

[18] M. E. Helgeson, Y. Gao, S. E. Moran, J. Lee, M. Godfrin, A. Tripathi, A. Bose, and P. S. Doyle, "Homogeneous percolation versus arrested phase separation in attractively-driven nanoemulsion colloidal gels," *Soft matter*, vol. 10, no. 17, pp. 3122–3133, 2014.

[19] A. Tobitani and S. B. Ross-Murphy, "Heat-induced gelation of globular proteins. 1. model for the effects of time and temperature on the gelation time of bsa gels," *Macromolecules*, vol. 30, no. 17, pp. 4845–4854, 1997.

[20] W. Liao, Y. Zhang, Y. Guan, and X. Zhu, "Gelation kinetics of thermosensitive pnipam microgel dispersions," *Macromolecular Chemistry and Physics*, vol. 212, no. 18, pp. 2052–2060, 2011.

[21] W. D. Callister and D. G. Rethwisch, *Fundamentals of materials science and engineering: an integrated approach*. John Wiley & Sons, 2012.

[22] M. Avrami, "Kinetics of phase change. i general theory," *The Journal of chemical physics*, vol. 7, no. 12, pp. 1103–1112, 1939.

[23] H. Bhadeshia, "Thermodynamic analysis of isothermal transformation diagrams," *Metal science*, vol. 16, no. 3, pp. 159–166, 1982.

[24] J. L. Rupp, B. Scherrer, N. Schäuble, and L. J. Gauckler, "Time–temperature–transformation (ttt) diagrams for crystallization of metal oxide thin films," *Advanced Functional Materials*, vol. 20, no. 17, pp. 2807–2814, 2010.

[25] L. Chan, H. Nae, and J. Gillham, "Time-temperature–transformation (ttt) diagrams of high tg epoxy systems: Competition between cure and thermal degradation," *Journal of applied polymer science*, vol. 29, no. 11, pp. 3307–3327, 1984.

[26] Q. Lin, A. F. Yee, J. D. Earls, R. E. Hefner Jr, and H.-J. Sue, "Phase transformations of a liquid crystalline epoxy during curing," *Polymer*, vol. 35, no. 12, pp. 2679–2682, 1994.

[27] H. A. Kramers, "Brownian motion in a field of force and the diffusion model of chemical reactions," *Physica*, vol. 7, no. 4, pp. 284–304, 1940.

[28] R. N. Zia, B. J. Landrum, W. B. Russel, B. J. Landrum, and W. B. Russel, "A micro-mechanical study of coarsening and rheology of colloidal gels : Cage building , cage hopping , and Smoluchowski ' s ratchet," vol. 1121, no. 5, pp. 1121–1157, 2014.

[29] P. Padmanabhan and R. Zia, "Gravitational collapse of colloidal gels: non-equilibrium phase separation driven by osmotic pressure," *Soft matter*, vol. 14, no. 17, pp. 3265–3287, 2018.

[30] P. Padmanabhan, T. T. D. Nguyen, M. E. Helgeson, and R. N. Zia, "Three distinct temporal regimes describe gelation following arrested phase separation of colloids." unpublished, N.D.

[31] S. Plimpton, "Fast parallel algorithms for short-range molecular dynamics," *Journal of computational physics*, vol. 117, no. 1, pp. 1–19, 1995.

Chapter 6

Kinetics and elasticity of colloidal gel structure formation

Having addressed the gelation and phase behavior that occur in the thermoresponsive nanoemulsion system, in this chapter we examine more closely the kinetics of coarsening *en route* to deep arrest. We use rheo-microscopy to uncover the quench dependence of coarsening rates that evidently recapitulates the underlying interdroplet attractions and use the results to formulate a simple model for viscoelastic coarsening kinetics.

6.1 Introduction

Arrested phase separation is a ubiquitous physical phenomena observed in both simple colloidal materials, such as polymer-colloid mixtures, as well as in complex biological systems, such as biophotonic nanostructures. [1, 2] By better understanding the formation processes and material properties associated with arrested phase separation, we can begin to rationally engineer novel soft materials for use as additive manufacturing inks, biomaterial templates, or consumer products. Underlying arrested phase separation is the dynamic interplay between equilibrium phase instability processes, viscoelastic rheology and kinetic arrest of dense glassy states.

6.1.1 Phase separation kinetics

As introduced in Chapter 1, theoretical descriptions to address the kinetic process of spinodal decomposition originate with the Cahn-Hilliard model, which can be used to derive scaling predictions for early and late stage growth of coarsening domains. [3] While these early descriptions provide scaling arguments for early and late stage behavior, as a whole they are insufficient for study of viscoelastic colloidal gel systems as they assume purely Newtonian behavior of the separating phases.

Later work that incorporated fluid velocity fields and viscoelasticity in addition to the diffusive contributions of the Cahn-Hilliard model are comprehensively summarized by Tanaka through a viscoelastic phase separation model, which was developed more generally to describe observations in phase separating polymer solutions and blends. [4] This model is more appropriate for the thermoresponsive nanoemulsion system as it accounts for the asymmetric rheology between the gelling dense phase and the dilute droplet phase. Resulting from this theory is a prediction for order parameter switching during phase separation, described by an intermediate elastic regime of phase separation during which the dominant time scale is set by rheological properties of the domains as opposed to composition coarsening of the domains. Following the arguments of the viscoelastic model, late stage coarsening kinetics revert to hydrodynamic arguments for scaling relations. [5]

While the Tanaka model proscribes quantitative features of viscoelastic phase separating systems, a majority of the experimental evidence is presented with polymeric systems, where the existence of a viscoelastic time scale has been debated. [6, 7] Colloidal systems, in contrast, have not been able to address questions of viscoelastic coarsening kinetics due to the system limitations of kinetic study commonly associated with depletion gels, which includes the inability to dynamically tune attraction strength as well as the relative weak elasticity of the final gels. [8, 9] For the thermoresponsive nanoemulsion system in which kinetic study is much more easily achieved, investigation of microscopic coarsening dynamics by Gao et al. revealed several collective modes of motion including diffusion, advection and coalescence of dense domains that manifests macroscopically as intermittent, superdiffusive coarsening. [10, 11] In aggregate, the thermoresponsive nanoemulsion coarsening dynamics exhibited the late-stage linear growth expected by the viscoelastic model (cf. Figure 3(c) in Ref. [11]). However, because only a single quench was studied, there is insufficient information to examine how the depth of quench into the spinodal region influences the coarsening kinetics.

Quench-dependent phase separation kinetics potentially allows us to control the heterogeneous structure of the arrested colloidal gel. Consequently, we can leverage this property to systematically probe the influence of heterogeneity on properties such as gel elasticity, which we describe next.

6.1.2 Colloidal gel elasticity

Colloidal gel elasticity arises from the network structure of interconnected particles. Predicting gel elasticity from descriptions of the particles, however, has not made significant theoretical progress due the disordered nature of colloidal gels making direct comparisons to experimental systems limited in scope.

For the extreme case of ordered colloidal systems such as those forming stable crystalline lattices, elasticity can be described based on nearest neighbor contacts in addition to particle volume fraction, radius, and interaction potential. [12] In less ordered but more dense depletion gels, Shah et al. reported that the localization length — reflecting the mobility of a particle within a cage of other particles — can serve as an additional relevant length scale contributing to gel elasticity. [13] Finally, providing a more general quantitative description for gels originally developed for gels formed via DLCA, arguments by Patel and Russel suggest that the high-frequency modulus can be estimated by the product of the number density of "bonds" and the elastic constant of a "bond", which for a harmonic potential is given by the curvature of the interaction potential such that

$$G'_{\infty} = \Gamma \frac{\phi^2}{a} \left(\frac{\partial^2 U}{\partial r^2} \right)_{min} \tag{6.1}$$

where Γ is a constant of proportionality that should only depend on the details of the material system and not the interaction potential attraction strength.

Eberle et al. have demonstrated that adhesive hard spheres exhibit gel elasticity somewhat consistent with this elastic modulus scaling, collapsing observed behavior onto a constant of $\Gamma \sim O(10)$. [14] As noted by Patel and Russel, however, if Equation (6.1) is the correct description of colloidal gel elasticity then we would expect $\Gamma \sim O(1)$. For the thermoresponsive nanoemulsion system, no comparison has been made to consider its colloidal gel elasticity with respect to proposed theories.

6.1.3 Goals

Through the current work, we develop a more complete understanding of quench-dependent coarsening kinetics of viscoelastic spinodal decomposition by measuring the rate of coarsening for a range of state points inside the region of arrested spinodal decomposition along an isochore for the thermoresponsive nanoemulsion system. Additionally, to address the features of colloidal gel elasticity that vary with quench depth, we evaluate the reduced elasticity parameter in Equation (6.1) with the two Yukawa interaction model that we have developed to describe the essential physics of the colloidal attractions in the system.

6.2 Methods

Thermoresponsive nanoemulsions with colloid volume fraction $\phi = 0.33$ were synthesized as described in Section 2.1.1 Simultaneous rheology and structural measurements were made using the stress-controlled rheo-microscopy instrument as described in Section 2.4, using an upper glass plate with thickness 4.05 mm. Samples were loaded at room temperature and quenched rapidly over 1 min to a final temperature. Linear viscoelastic moduli were measured over time for an input strain amplitude of 0.1% and angular frequency of $10\,\mathrm{rad\,s^{-1}}$.

Micrographs were acquired with a long working distance objective to image through the lower glass plate with thickness 4.17 mm. Characteristic length scales were determined from radially averaged Fourier transforms of coarsening gels. To filter out the low-wave vector noise, texture analysis microscopy was applied to images to correlate the image features with a Gaussian kernel. In this analysis a correlogram was derived for each image which identified the distribution of colloid-rich domains. [15]

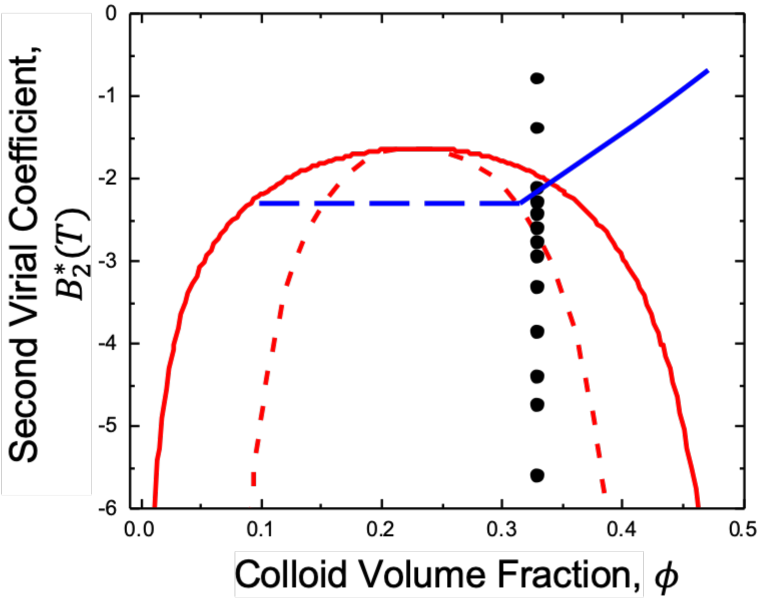

Figure 6.1: Predicted phase diagram of the thermoresponsive nanoemulsion system, as developed in Chapter 4 using the method of variation free energy calculations. The figure here is akin to Figure 4.10, with the blue boundary identifying the experimental gelation boundary. The added black points show the specific quenches tested along the $\phi = 0.33$ isochore from room temperature ($B_2^* = -0.8$) to elevated temperatures within the phase coexistence region ($B_2^* = -5.7$).

6.3 Results and Discussion

6.3.1 Interaction Potential

From the hard sphere plus two Yukawa interaction potential developed in Chapter 3, we are able to map our results into the plane of reduced second virial coefficient and colloid volume fraction ϕ. The phase envelope associated with the interaction potential can be estimated from variational free energy calculations following the method described by Tejero *et al.* for a general Yukawa potential. [16] The predicted binodal and spinodal boundaries are shown once again as in Figure 6.1 as we developed in Chapter 4, with the addition of the specific isochore we explore in this chapter. As such, the location of the variations in thermal quench relative to the predicted phase envelope can be used to rationalize the subsequent discussions.

6.3.2 Structure Formation

Through use of the rheo-microscopy apparatus described in Chapter 2, we are able to simultaneously resolve the linear viscoelastic response of the gel and the microscopic structure. Figure 6.2(a) shows the rheological data superimposed with imaging analyses on a subset of the corresponding data points. Only a subset of the dense image data set is analyzed using the textural analysis to draw focus to the region of structural interest.[1] Because the optically resolvable length scales are $O(10^2)$ times the primary colloid diameter, the observed structure should reflect the late-stage coarsening of spinodal decomposition.

The rheological response of the gelling nanoemulsion is consistent with previously reported isothermal aging experiments. [11, 17–19] However, unprecedented prior to this measurement is the superposition of this viscoelastic time series with microstructure measurements. Immediately we can see that the shoulder in the rheological data, seen around 500 s, coincides closely with the rapid coarsening and eventual plateau of gel domain size.

With respect to the phase coexistence region, the range of quenches for which we are able to observe spinodal coarsening agree with the expected spinodal region at this particular volume fraction, with several coarsening responses shown in Figure 6.3. The two lowest non-zero growth rates fall within the metastable region as predicted by theory, but the observed structure formation appears similar to the spinodal decomposition

---

[1] To choose the subset, we visually identify the temporal region between where we first visually observed the structure up until a static structure is observed.Because of optical component limitations we are not able to reliably resolve structures below $\sim 2\,\mu\text{m}$.

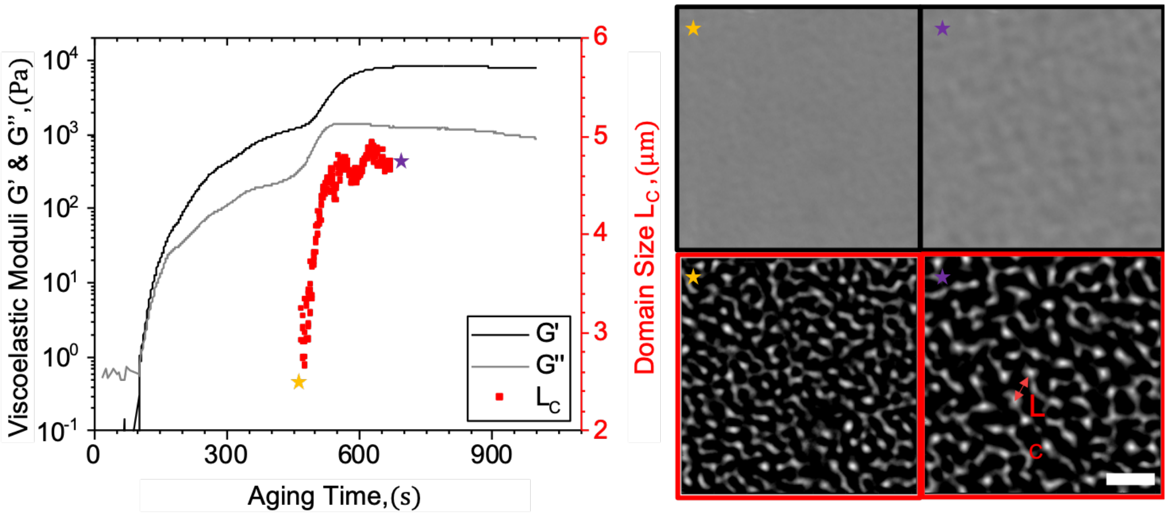

(a) (b)

Figure 6.2: Rheo-microscopy results during isothermal aging for $-B_2^* = 3.86$. (a) Time evolution of viscoelastic moduli and dominant length scale during arrested phase separation as determined by texture analysis microscopy. The yellow and purple stars label the first and last microscopy image analyzed using TAM. (b) The two images above show the corresponding first and last raw microscopy images, which suffer from low contrast, before applying TAM. To develop quantitative measure of the domain spacing L_C over time, textural analysis is applied to a visually identified subset of images to develop the correlograms as shown below, in which the domain spacing is much easier to resolve through a radially averaged Fourier transform. Scale bar indicates 10 µm.

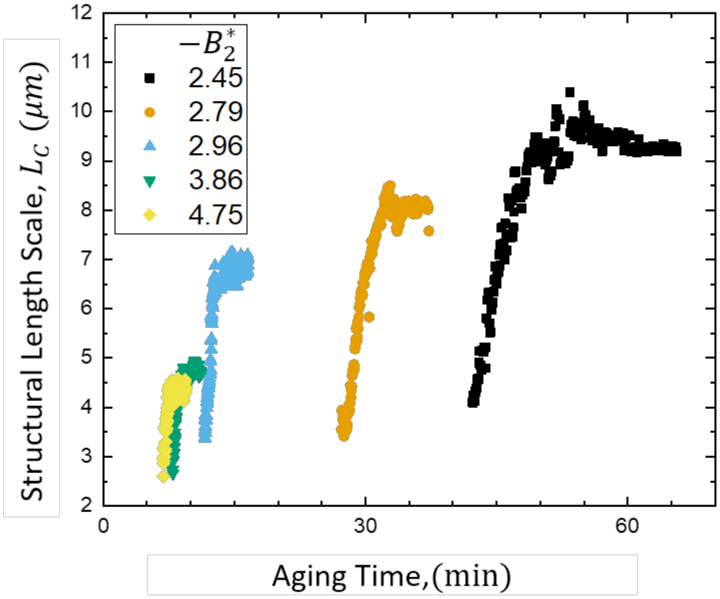

Figure 6.3: Rheo-microscopy length scale results during isothermal aging for varying quench depths. Consistently, we find that the emergence of structure grows rapidly at a linear rate prior to prolonged arrest.

region. Thus, we cannot ascribe complete certainty to the metastable boundary as predicted from theory, which is reasonable given the mean field nature of its predictions and assumptions.

To arrive at a semi-empirical expectation for the variation in coarsening rate as a function of temperature, we begin with scaling arguments for spinodal decomposition kinetics. In the regime of late-stage spinodal decomposition, coarsening is driven primarily by hydrodynamics, and Siggia showed that the rate of coarsening should scale as γ/η, where γ is the interfacial tension between the colloidal phases and η is the effective viscosity of the two phases. [5] Generally, both γ and η will be functions of temperature. But because the fluid components do not undergo a phase change within the studied temperature range, we would expect the change in overall suspension viscosity to be relatively small as a function of quench depth. Thus, the dominant contribution to the scaling will arise from the change in interfacial tension between colloidal phases with respect to temperature such that $R \propto \gamma$ for a growth rate R, where $R \equiv \frac{d\,L_C}{d\,t}$. The surface tension in depletion gels scales proportional to the strength of attraction, as set in part by the osmotic pressure difference between the dilute and dense phases controlled by the concentration of depletant. [20] Analogously, we expect the osmotic pressure gradient in the current system should scale directly proportional to the temperature-dependent attraction strength, $\gamma \propto \varepsilon(T)$, which has been previously shown to be accurately described by a sigmoidal temperature dependence. [11] Similar sigmoidal temperature dependencies have also been observed for thermoresponsive core-shell nanoparticles. [21]

From these scaling relations, we apply the following semi-empirical growth rate model guided by the above arguments that reflects the sigmoidal relation observed in the temperature dependence of the attraction strength

$$R(T) = \frac{R_0}{1 + \exp\left[-\alpha\left(\frac{T}{T_C} - 1\right)\right]} \tag{6.2}$$

where R_0 is the limiting coarsening rate, T_C is the critical temperature, and α describes the steepness of the response.

The measured growth rates for varying quench depths are shown in Figure 6.4. From fitting the growth rates to the proposed model with no fixed parameters, we find a critical temperature of $T_C = 37.1 \pm 0.2\,^{\circ}\mathrm{C}$, corresponding to $B_2^*(T_C) = -2.47$. For comparison, the sigmoidal fit used to describe the temperature-dependent well depth based on scattering data by Gao et al. exhibits a critical inflection temperature of $T_C = 34 \pm 1\,^{\circ}\mathrm{C}$, corresponding to $B_2^*(T_C) = -1.98$.[2] [11] Whereas our empirical fit based on growth rates is a macroscopic observation at moderately dense droplet volume fractions,

---

[2] The uncertainty in T_C is calculated using the reported confidence intervals for the sigmoidal fit parameters in [11]

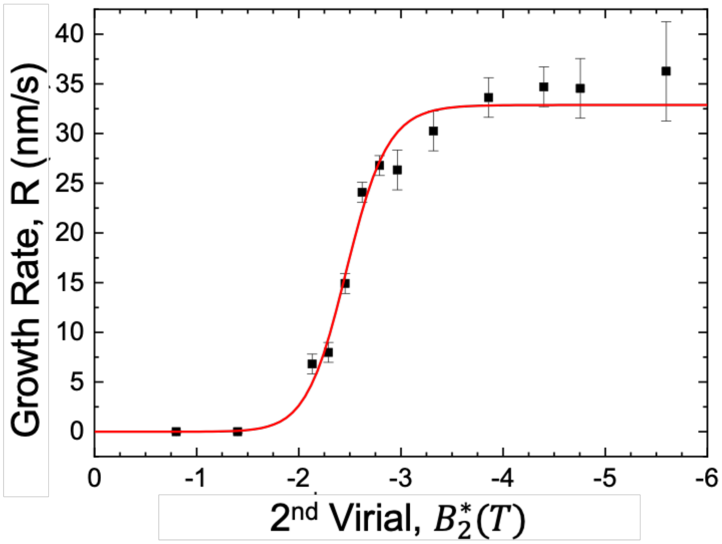

Figure 6.4: Late-stage linear growth rate, R, as a function of isothermal quench depth. Error bars reflect the standard error of the linear fit for each quench depth. Growth rates are fit to the sigmoidal form described in Equation (6.2) based on the functional form of the temperature-dependent interaction strength. Best fit parameters give $B_2^* = -2.47$, $R_0 = 33 \pm 1\,\mathrm{nm\,s^{-1}}$, $\alpha = -257 \pm 26$.

the prior fit based on scattering data more closely describe interparticle interactions in the dilute limit. Thus, we would not expect these critical temperatures to be identical a priori. However, the fact that they only differ by 3 °C is notable given their significantly different assumptions. Additionally, they both compare well with the minimum gelation temperature estimated independently by aging rheology as in Chapter 4, $T_{gel} = 35 \pm 1\,°\mathrm{C}$.

Overall, these structural insights show that in phase separating colloidal gels, the quench dependence of coarsening rates can be connected to the interparticle attractions. In future work with colloidal systems where the interparticle attractions are difficult to (or have not yet been) characterized, observation of coarsening dynamics should provide a useful macroscopic tool for gleaning information about the microscopic features of the colloidal assembly.

6.3.3 Elasticity

While structure formation is a critical step to understand during colloidal gelation, resultant mechanical properties like elasticity are also important as they will also respond to varying quenches and ultimately affect material performance. To evaluate the elasticity of the arrested gels, we consider the plateau storage modulus in association with the presently proposed two Yukawa form of the interaction potential, from which we can directly evaluate the second derivative of $U(r)$ around the potential well minimum. The second derivative encodes information about the shape of the potential and can be used to nondimensionalize the elastic modulus according to Equation (6.1)

When we plot the Γ with respect to quench depth, as shown in Figure 6.5, we see a clear variation as a function of quench depth, ranging over an order of magnitude from 0.07 to 2.8. As referenced in the introduction, studies of silica grafted colloidal systems demonstrate proportionality constants based on yield stress of order $\Gamma \sim O(10^1)$. [14, 22] If the nondimensional scaling was fully captured by the describing potential, we would expect the pre-factor to be invariant with quench depth. However, this is not what is observed, even within the same material system.

Although we do not find that Γ is invariant with respect to quench depth, we nonetheless see limiting behavior at sufficiently deep quenches showing that Γ approaches a value of $O(1)$. We can physically justify this agreement by realizing that these deep quenches should more closely resemble the DLCA gels initially studied by Patel and Russel, wherein the particles of the gel network are towards the limit of irreversible bonding upon contact and thus arrest phase separation.

By contrast, the shallow quench limit reflects gel formation where the coarsening of phase separation dominates gel structure prior to eventual gel arrest. Thus, the arrested structure may comprise more loosely associated larger droplet clusters while still achiev-

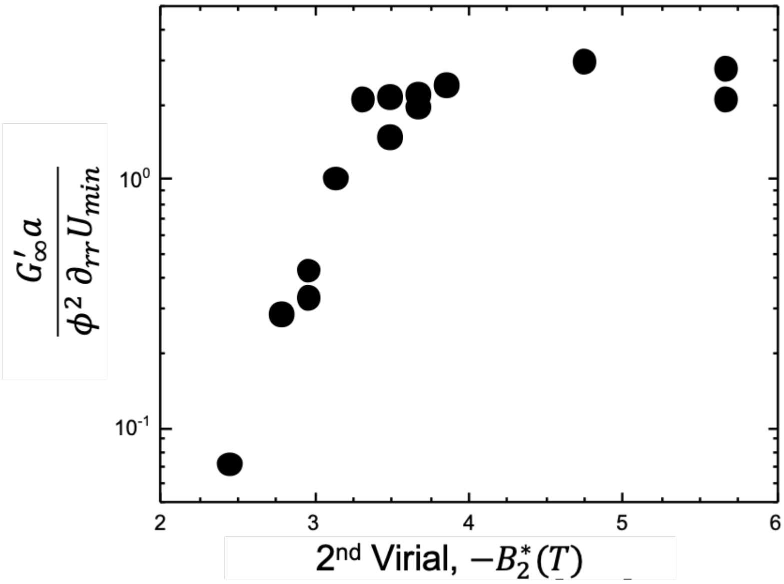

Figure 6.5: The dimensionless colloidal gel elastic modulus, as scaled by the second derivative of the interaction potential at the well minimum using dimensional scaling of elastic modulus.

ing mechanical percolation. However, as a result the assumption that all particle volumes participate in the elastic network (as implied by the ϕ^2 contribution) becomes an overestimate, and the calculated reduced modulus takes on values less than $O(1)$. From this we may reason that the deviations in Γ for shallow quenches is a result of a change in the scaling exponent for ϕ different from ϕ^2, which would reflect a change in the topological assumptions of "bond" arrangement within network strands.

To evaluate a plausible adjustment to the elasticity scaling, we can see whether the structural heterogeneity results in a renormalization of the length scale associated with elastic energy storage. We consider whether it is possible that the larger-scale struts (comprising hundreds of particles and bonds) serve as the characteristic length scale for bond energy storage as opposed to individual particle radii. Simulations of aging colloidal gels have observed this to be the case in the high frequency limit, with both elastic and

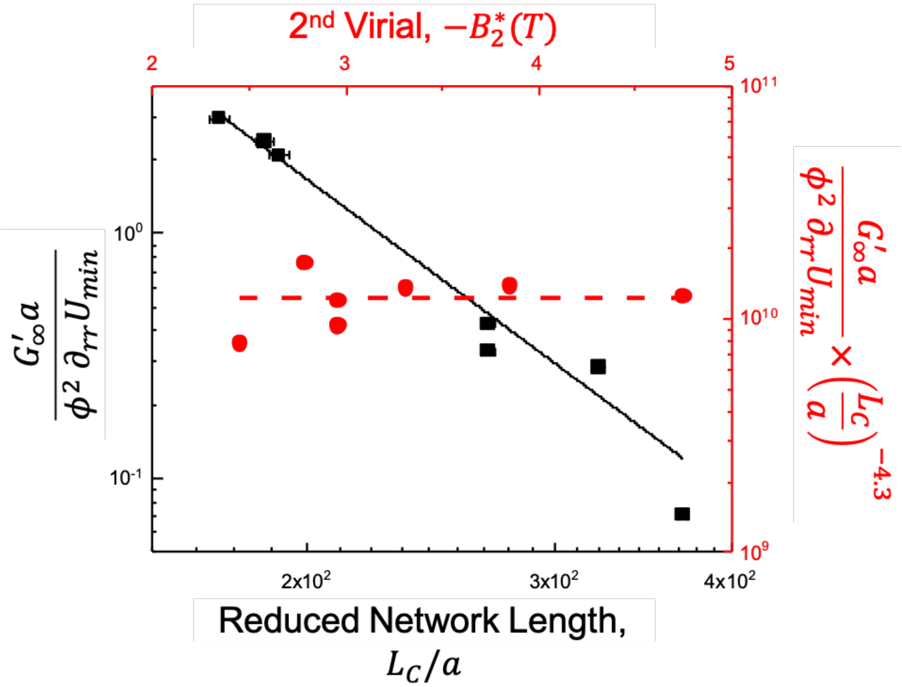

Figure 6.6: In black, the nondimensionalized colloidal gel elastic modulus as a function of network length, with plateau modulus scaled according to Equation (6.1) and domain size L_C scaled by the particle radius a. Fit to a power law finds a scaling exponent of -4.3 ± 0.3. In red, the upper right axes show collapse of the reduced parameter with respect to quench depth, which improves upon the order of magnitude variation observed in Figure 6.5

viscous moduli collapsing with respect to L_C. [23] This comparison as shown in Figure6.6, demonstrates a scaling exponent of -4.3 ± 0.3 to describe the dependence of colloidal gel elasticity on the arrested heterogeneous length scale.

If we then use that scaling to reevaluate our observations of quench dependent elasticity, we see in the red secondary axes of Figure 6.6 that the values collapse much more reasonably around an apparent reduced parameter $\Gamma_{app} \sim O(10^{10})$, where now Γ_{app} is related to the dimensional plateau modulus as

$$G'_\infty = \Gamma_{app} \frac{\phi^2}{a} \left(\frac{\partial^2 U}{\partial r^2} \right)_{min} \left(\frac{L_C}{a} \right)^{4.3} \tag{6.3}$$

which directly incorporates a power law dependence of the heterogeneous network length scale on the colloidal gel elasticity.

6.4 Conclusion

By studying the structure formation and elasticity of colloidal gels formed via thermoresponsive attractions, we have shown that macroscopic colloidal gel behavior reflects the temperature dependence of coarsening and arrest kinetics during gelation, as modulated by attractions between substituent colloids. The quench dependence of coarsening rates is consistent with simple scaling arguments for late stage spinodal decomposition and as a result allows us to indirectly understand more about the interparticle attractions through observation of structure formation. Additionally, we find that the colloidal gel elastic modulus, when nondimensionalized using existing scaling theories, exhibits an order of magnitude variation in pre-factor within the same material system. This result suggests that current theories for colloidal gel elasticity require additional material descriptors to sufficiently describe the scaling behavior with respect to variations in quench depth and more generally interaction strength.

Bibliography

[1] S. Manley, H. Wyss, K. Miyazaki, J. Conrad, V. Trappe, L. Kaufman, D. Reichman, and D. Weitz, "Glasslike arrest in spinodal decomposition as a route to colloidal gelation," *Physical review letters*, vol. 95, no. 23, p. 238302, 2005.

[2] E. R. Dufresne, H. Noh, V. Saranathan, S. G. Mochrie, H. Cao, and R. O. Prum, "Self-assembly of amorphous biophotonic nanostructures by phase separation," *Soft Matter*, vol. 5, no. 9, pp. 1792–1795, 2009.

[3] J. E. Cahn and J. W. Hilliard, "Free Energy of a Nonuniform System. I. Interfacial Free Energy," *The Journal of Chemical Physics*, vol. 28, no. 2, pp. 258–267, 1958.

[4] H. Tanaka, "Viscoelastic phase separation," *Journal of Physics: Condensed Matter*, vol. 12, no. 15, p. R207, 2000.

[5] E. D. Siggia, "Late Stages of Spinodal Decomposition in Binary Mixtures," *Physical Review A*, vol. 20, no. 2, pp. 595–605, 1979.

[6] W. Brown and P. Stepanek, "Viscoelastic relaxation in semidilute and concentrated polymer solutions," *Macromolecules*, vol. 26, no. 25, pp. 6884–6890, 1993.

[7] C. Wang, Z. Sun, and Q. Huang, "Quasielastic light scattering of polystyrene in diethyl malonate in semidilute concentration," *The Journal of chemical physics*, vol. 105, no. 14, pp. 6052–6059, 1996.

[8] N. A. Verhaegh, J. S. van Duijneveldt, J. K. Dhont, and H. N. Lekkerkerker, "Fluid-fluid phase separation in colloid-polymer mixtures studied with small angle light scattering and light microscopy," *Physica A: Statistical Mechanics and its Applications*, vol. 230, no. 3-4, pp. 409–436, 1996.

[9] P. J. Lu, E. Zaccarelli, F. Ciulla, A. B. Schofield, F. Sciortino, and D. a. Weitz, "Gelation of particles with short-range attraction," *Nature*, vol. 453, pp. 499–503, May 2008.

[10] A. Duri and L. Cipelletti, "Length scale dependence of dynamical heterogeneity in a colloidal fractal gel," *EPL (Europhysics Letters)*, vol. 76, no. 5, p. 972, 2006.

[11] Y. Gao, J. Kim, and M. E. Helgeson, "Microdynamics and arrest of coarsening during spinodal decomposition in thermoreversible colloidal gels," *Soft Matter*, vol. 11, no. 32, pp. 6360–6370, 2015.

[12] R. Buscall, J. W. Goodwin, M. W. Hawkins, and R. H. Ottewill, "Viscoelastic properties of concentrated latices. part 2.theoretical analysis," *Journal of the Chemical Society, Faraday Transactions 1: Physical Chemistry in Condensed Phases*, vol. 78, no. 10, pp. 2889–2899, 1982.

[13] S. Shah, Y.-L. Chen, K. S. Schweizer, and C. Zukoski, "Viscoelasticity and rheology of depletion flocculated gels and fluids," *The Journal of chemical physics*, vol. 119, no. 16, pp. 8747–8760, 2003.

[14] A. P. Eberle, N. Martys, L. Porcar, S. R. Kline, W. L. George, J. M. Kim, P. D. Butler, and N. J. Wagner, "Shear viscosity and structural scalings in model adhesive hard-sphere gels," *Physical Review E*, vol. 89, no. 5, p. 050302, 2014.

[15] Y. Gao and M. E. Helgeson, "Texture analysis microscopy: quantifying structure in low-fidelity images of dense fluids.," *Optics express*, vol. 22, pp. 10046–63, apr 2014.

[16] C. Tejero, A. Daanoun, H. Lakkerkerker, and M. Baus, "Isostructural solid-solid transition of (colloidal) simple fluids," *Physical Review E*, vol. 51, no. 1, p. 558, 1995.

[17] M. E. Helgeson, S. E. Moran, H. Z. An, and P. S. Doyle, "Mesoporous organohydrogels from thermogelling photocrosslinkable nanoemulsions," *Nature Materials*, vol. 11, pp. 344–352, February 2012.

[18] L.-C. Cheng, P. D. Godfrin, J. W. Swan, and P. S. Doyle, "Thermal processing of thermogelling nanoemulsions as a route to tune material properties," *Soft matter*, vol. 14, no. 27, pp. 5604–5614, 2018.

[19] L. C. Hsiao and P. S. Doyle, "Celebrating soft matter's 10th anniversary: Sequential phase transitions in thermoresponsive nanoemulsions," *Soft Matter*, vol. 11, no. 43, pp. 8426–8431, 2015.

[20] J. Brader and R. Evans, "The fluid-fluid interface of a model colloid-polymer mixture," *EPL (Europhysics Letters)*, vol. 49, no. 5, p. 678, 2000.

[21] A. Zaccone, J. J. Crassous, B. Béri, and M. Ballauff, "Quantifying the reversible association of thermosensitive nanoparticles," *Physical review letters*, vol. 107, no. 16, p. 168303, 2011.

[22] J. Min Kim, A. P. Eberle, A. Kate Gurnon, L. Porcar, and N. J. Wagner, "The microstructure and rheology of a model, thixotropic nanoparticle gel under steady shear and large amplitude oscillatory shear (laos)," *Journal of Rheology*, vol. 58, no. 5, pp. 1301–1328, 2014.

[23] R. N. Zia, B. J. Landrum, W. B. Russel, B. J. Landrum, and W. B. Russel, "A micro-mechanical study of coarsening and rheology of colloidal gels : Cage building , cage hopping , and Smoluchowski ' s ratchet," vol. 1121, no. 5, pp. 1121–1157, 2014.

Chapter 7

Intracycle yielding of heterogeneous colloidal gels under nonlinear oscillatory deformation

Thus far we have investigated the phase behavior and processing features of the thermoresponsive colloidal gel in the quiescent state. However, one aspect of practical importance is the behavior of the gel during mechanical yielding and the microscopic origins of the yielding phenomenon that set this behavior. In this chapter we lay out experimental progress in observing nonlinear yielding phenomena in heterogeneous gels using rheo-microscopy; this includes the design considerations for properly synchronizing the mechanical and microscopic data streams, as well as quantitative analysis to describe the development of large-scale anisotropy over the course of tens of input cycles. In total we are able to extract information about the void formation, mechanical modulus, and structural anisotropy that provides a testable foundation for further study into these complex yielding processes.

7.1 Introduction

In the broadest sense, yielding of a colloidal gel material refers to some form of mechanical failure of the pristine network as a result of the imposed stress. This stress or strain is outside of the linear viscoelastic limit of rheological behavior and instead access the nonlinear, or large amplitude, material response. [1, 2] While interpretation of nonlinear responses presents its own challenges, [3, 4] we can at the very least develop a sense for the gel yielding processes by probing the rheology and microstructure in this region.

Experimental realizations of colloidal gel yielding have progressed hand in hand with hypotheses related to the microscopic mechanism of failure. To describe the yielding that we aim to characterize in this chapter, we build from prior reports on yielding behavior.

7.1.1 Homogeneous Yielding

Homogeneous yielding refers to breakage of the colloidal network due to a single rupture mechanism resulting in a corresponding change to its viscoelastic response leading to eventual fluidization. [5] In this simplest possibility of colloidal gel yielding, the dominant mechanism of is interparticle bond breakage, which in homogeneous yielding occurs — as the name implies — homogeneously everywhere within the gel structure. This uniform breakage gives rise to a singular, clearly-defined yield stress or strain point. [6]

7.1.2 Heterogeneous Yielding

In contrast to simple homogeneous yielding, many colloidal gels exhibit a more broadened or “heterogeneous” yielding transitions, where it is assumed that material failure proceeds by a combination of two or more yielding mechanisms that in sequence result in ultimate transition to the flowing state. Heterogeneous yielding has been observed in highly dense attractive colloidal glasses, which has been hypothesized to proceed through a two-step process of bond breakage then cage breakage. [7–9] Heterogeneous yielding has also been observed in dilute gels and has similarly been proposed to proceed through first bond rotation and then breakage. [10] These mechanisms only attribute heterogeneity to differences in time scales between two distinct dynamic processes as opposed to differences in time scales due to variations in length scale, for the same fundamental process.

Heterogeneous yielding has also been extended in scope to account for the multiple length scales that can bear relevance to the yielding process. For example, ultrasonic probing of carbon black gels observed a heterogeneous process initiated at the sample cell wall then proceeding to fluidize the entire bulk sample. [11] Additionally, the fluidized microstructure that results following yielding can take on large, anisotropic log-like structures aligned along the vorticity axis. [12, 13] The formation of these log structures has been attributed to the coupling of shear-induced breakage/reformation of particle clusters and long-ranged hydrodynamic interactions. [14–16]

Of direct relevance to this chapter, a recent study by Kim et al. investigated the time-averaged structure (via ultra-small angle neutron scattering, USANS) and rheology of the thermoresponsive nanoemulsion system under large amplitude oscillatory shear (LAOS). LAOS is a convenient deformation protocol for probing the yielding transition because it allows examination of the yielding state in a periodic steady state. This previous investigation revealed an apparent multi-stage process by which yielding is initiated on a length scale much larger than the individual particles at strains near the yielding point. [17] Through progressively larger straining, they proposed a picture of heterogeneous yielding that progressed from hundreds of particle diameters to tens of particle diameters, owing to the formation and saturation of large, fluid-filled voids and consequently compression of the overall heterogeneous network. Furthermore, they found that the deformation rate-dependence of the yield point could be predicted by a simple model for the contribution of poroelastic drainage through the heterogeneous structure to the total shear stress.

A limitation of the previous study was the use of USANS, which limits the characterization of microstructure to pre-averaged measures in Fourier space obtained over very long times, preventing higher-resolution examination of the time-dependent microscopic processes of yielding. Furthermore, the USANS measurement is smeared over one direction of the two-dimensional scattering, prohibiting access to information regarding the anisotropy of structural rearrangement during deformation and flow. In this work, we overcome these limitations through the use of rheo-microscopy, which provides unprecedented insight into the real-space evolution of structure during the heterogeneous yielding processes. Nevertheless, the preceding work of Kim et al. provided a well-defined hypothesis for the multi-scale processes of heterogeneous yielding that can be directly tested with rheo-microscopy by resolving across multiple length scales as gel yielding evolves.

7.2 Data acquisition and analysis

To prepare the colloidal gel, we perform a rapid quench to a final temperature and allow the formation of the gel to fully proceed, as indicated by the plateau in structure and modulus considered in Chapter 5. This preparation ensures a repeatable colloidal gel condition between replicate tests, since the system has irreversibly ruptured subsequent to LAOS testing.

Two signals — one mechanical, one structural — are recorded through use of the rheo-microscope system detailed in Chapter 2. These signals are asynchronous because of the need for an uncompressed image stream, which is not feasible to implement within the rheometer software due to program memory constraints. Because the imaging detector has an upper maximum acquisition rate, this places constraints on the rheological oscillatory operating window within which we can reliably resolve image-to-image changes without aliasing. For the case of LAOS flow, this limits the oscillation frequency and strain amplitude for which structure can be resolved with high spatiotemporal resolution.

The physical constraint on this choice of LAOS angular frequency is given by the Nyquist-Shannon sampling theorem. [18] But the more limiting design constraint is determined as a function of the desired point density, N_p, within a single oscillation cycle. Qualitatively, we can think of this as needing to resolve a minimum number of frames within a single oscillation period, which is naturally a function of oscillation frequency. The resulting expression requires that the input angular frequency ω is limited by

$$\omega \leq 2\pi \, \frac{\text{radian}}{\text{cycle}} \times f_s \, \frac{\text{frame}}{\text{s}} \times \frac{1}{N_p} \, \frac{\text{cycle}}{\text{frame}}. \tag{7.1}$$

We can determine a similar constraint for the strain amplitude by considering the dimensions of pixels along the straining direction. If the strain amplitude is too high, then there will not be a material point that stays in the frame of the camera during the full oscillation cycle. In summary, we can use the operating diagrams as plotted in Figure 7.1. In the current work, our hardware is used at 15 frames per second.

7.2.1 Intercycle analysis

To synchronize the disparate data streams from the rheometer software and image acquisition post hoc, we develop here a rapid means of matching maximum straining rate with the maximum image velocity. We consider the correlation coefficient between

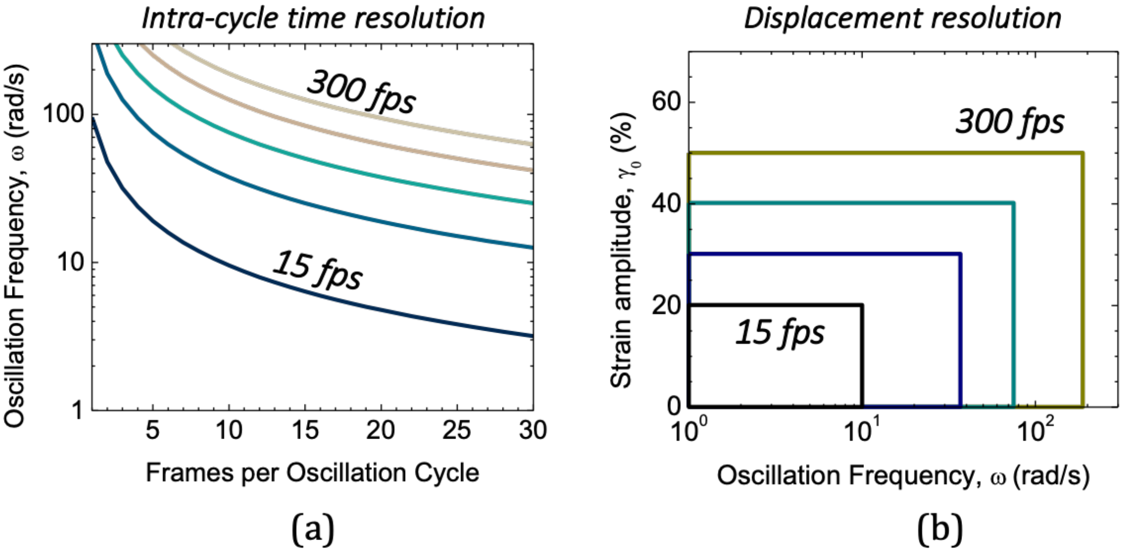

Figure 7.1: Valid operating windows for conducting synchronized LAOS rheo-microscopy. The maximum angular frequency is a function of the imaging frame rate and point density according to Equation (7.1), while the maximum strain amplitude is a function of the imaging window. To determine the present system constraints, we input a maximum frame rate of 15 frames per second, and a desired point density of $N_p = 8$ to capture the nodes, peak, trough, and inflection points in a single cycle. Consequently, the maximum resolvable angular frequency is approximately $10\,\mathrm{rad\,s^{-1}}$, and the maximum resolvable strain amplitude is 20%.

successive frames, calculated as

$$CC = \frac{\sum_x \sum_y \left(I_{xy} - \bar{I}\right)\left(J_{xy} - \bar{J}\right)}{\sqrt{\left[\sum_x \sum_y \left(I_{xy} - \bar{I}\right)^2\right]\left[\sum_x \sum_y \left(J_{xy} - \bar{J}\right)^2\right]}} \tag{7.2}$$

where CC is the correlation coefficient, x and y refer to the horizontal and vertical pixel values in the image, respectively, I and J are the two images to be correlated, and the over bar indicated the average gray scale pixel intensity of an image. By calculating the requisite CC values for the movie frames and overlaying it onto the recorded input strain rate of the strain oscillation cycle (with point density 513 points per cycle as set by the rheometer electronics), we see that the maxima in strain rate correspond to minima in the correlation coefficient. Intuitively this make sense, because at the strain rates of highest magnitude, the correlation between subsequent frames should be relatively the least similar due to the window of material moving the fastest. Once synchronizing

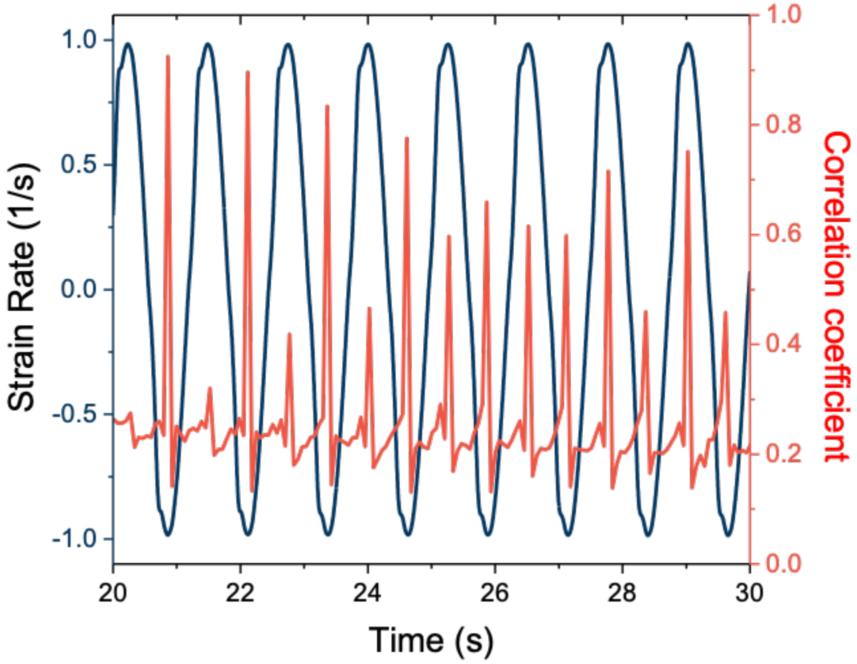

Figure 7.2: Example of plot used to align image and rheology data. The strain rate is known from rheometer software, and the correlation coefficient between sequential frames is calculated according to Equation (7.2). Because sequential frames will be least similar at the highest strain rates, we use that to align the troughs in orange with the extrema in blue.

mechanical and structural signals in this way, we can then consider the difference images between comparable points during an oscillation cycle. For example, we can compare an image of the gel only at the peaks or nodes of the input oscillating strain. This ensures that any subsequent analysis is only tracking the non-affine i.e. irreversible changes in gel structure, at a similar strain rate and at a similar point in the oscillation cycle. The non-affine intensity changes are simply described by the equation for δI, relative to the intensities in the first input cycle $N = 1$:

$$\delta I(x, y; \Delta N) = I(x, y, N) - I(x, y, 1). \tag{7.3}$$

To reduce the non-affine difference images to a single order parameter, we can further condense the difference by calculating a cumulative difference intensity, $\Delta\langle\delta I\rangle$ as the standard deviation of the distribution of pixel intensities within a single difference image. The use of this order parameter is meant to capture the growth of fluctuations due to alignment during yielding. Physically, this analysis assumes the intensity to be proportional to the local droplet concentration such that the resultant cumulative difference intensity is proportional to the mean-squared magnitude of non-affine density fluctuations.

Figure 7.3 summarizes the image analysis through an example of a difference image between images at subsequent oscillation peaks, as well as the corresponding pixel different intensity distribution.

7.2.2 Intracycle mechanical analysis

The highly resolved rheological response contains further information regarding the mechanical evolution of the yielding gel over time i.e. across strain cycles. Figure 7.4 illustrates the features of a single oscillation cycle. To account for the thixotropy (i.e. age-dependent rheology) of the sample, we use the first half of the oscillation cycle (clockwise from zero strain and positive stress to zero strain and negative stress) and mirror it during the second half. Once conditioning the raw data in this way, the material parameters we can consider in a cycle include the residual modulus, G_{Resid}, taken as the slope at zero stress. Physically, this elastic modulus corresponds to the instantaneous gel network elasticity at the beginning of the oscillation cycle.

A second parameter of interest is the overshoot in the stress σ_{Peak}. This overshoot in the second quadrant is followed by an undershoot $\sigma_{Peak} - \Delta\sigma$ before returning to the original stress. In previous work, the overshoot was shown to correspond physically to an

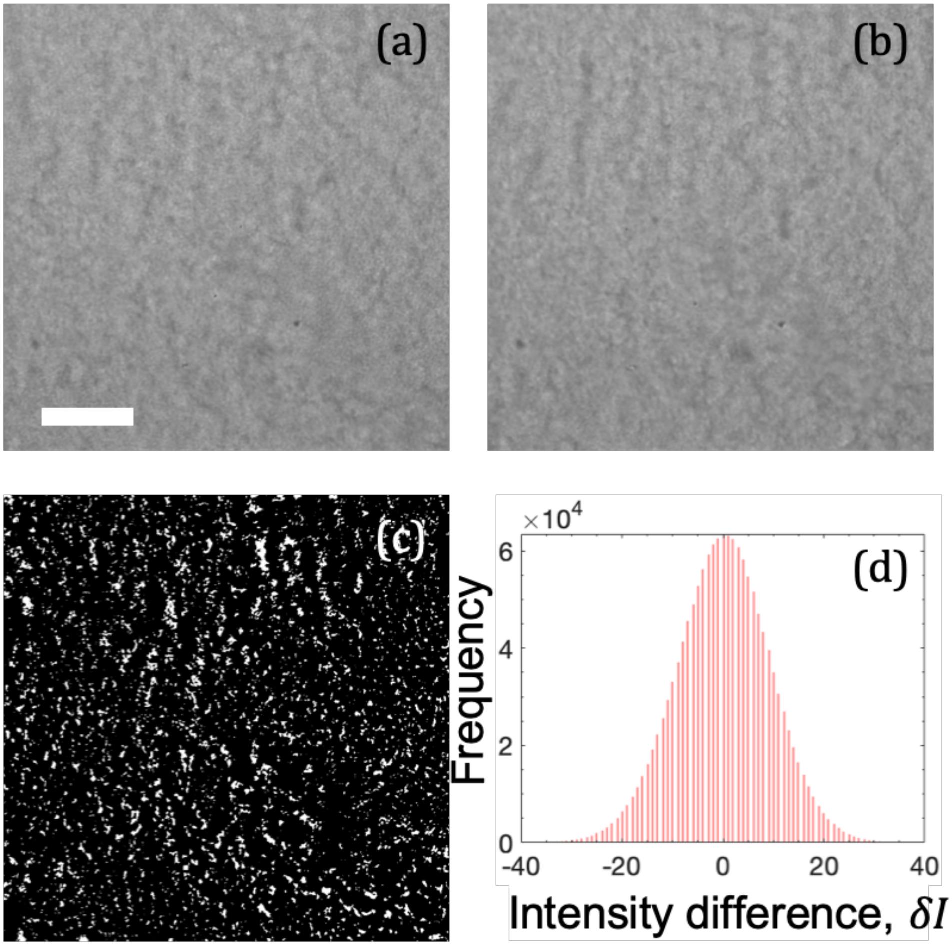

Figure 7.3: Summary of image analyses performed to extract non-affine metrics. Images (a) and (b) show the raw images at subsequent oscillation peaks, as developed by image and rheology synchronization. Scale bar indicates 100 µm. Image (c) shows the rescaled difference image between (a) and (b), with (d) showing the accompanying difference image intensity histogram of (c). The cumulative difference intensity is comparable to the width of the distribution in (d).

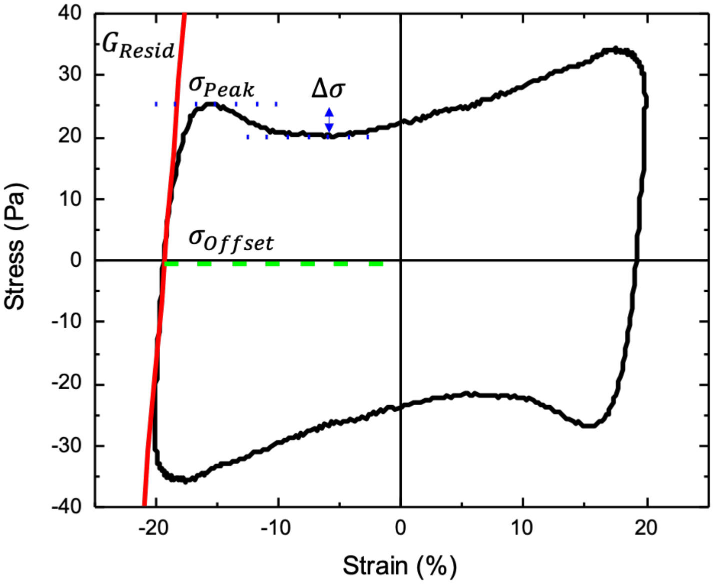

Figure 7.4: Lissajous-Bowditch plot of stress vs strain during a single oscillation cycle for a gel cured at 45C, with frequency 5 rad/s and strain amplitude 20%.

extra contribution to the yield stress due to the viscous stress associated with poroelastic drainage that relaxes after a poroelastic drainage time, as hypothesized and supported by rheo-USANS. [17]

Finally, we account for the fact that the oscillation is not perfectly centered about the origin, and there is a small offset stress σ_{Offset} on the order of 1 Pa between cycles. This offset can arise due to slight drift or slippage of the gel between the plate geometry over the course of the repeated large amplitude oscillation cycles.

We note that the derived parameters and physical interpretations presented here are reliant on a more complete nonlinear analysis performed in prior work, which applied the sequence of physical processes (SPP) framework [4] to the thermoresponsive nanoemulsion system. [17] Through their differential geometric analysis of the three-dimensional stress-strain-rate space curves, Kim et al. developed measures of instantaneous, intracycle viscoelastic moduli.

7.3 Rheo-microscopy results

The three stages of colloidal gel yielding are illustrated in the analysis that follows. We are able to track the rheological and structural metrics that reflect a three-step process toward the formation of aligned colloidal clusters. We discuss these results with close consideration of the previous hypotheses proposed by Kim et al. developed by examining coarser, time-averaged information.

7.3.1 Stage 1: Network rupture and void formation

From the pristine arrested gel state formed at a given temperature quench, the first event that must necessarily occur during nonlinear straining to result in yielding is network rupture. Rheologically, we expect that the gel will transition from a stress-strain curve without a stress overshoot to one with a clear stress overshoot seen with a non-monotonic second quadrant trace. However, apparatus limitations did not allow us to resolve the early cycle rheological response. Nonetheless, the presence of the stress overshoot in the earliest resolvable cycle must mean that this rheological transition took place, since we would expect the initial oscillation cycle to exhibit limiting behavior closer to the linear regime.

The non-affine difference images begin to reveal the formation of large voids within the heterogeneous mesoscopic structure during this stage. As seen in Figure 7.5, by cycle $N = 6$, voids as circled appear within the frame of view. Currently the voids are identified heuristically, by noting regions of the difference image that exhibit long, continuous dark regions corresponding to network rupture propagated to length scales larger than the initial textural size. Demarcation of the voids is achieved by following the “grain” lines that do not follow the texture of the full difference image.

By $N = 15$ straining cycles, the apparent boundaries of these voids are blurred, and they appear to rearrange and combine in favor of more clearly defined vertical stripes. We infer that the structures that are disappearing in this process are the large scale fluid voids, which are collapsed due to poroelastic flows in favor of smaller, cluster-scale voids. This physical picture follows the hypothesis put forth by Kim et al. regarding the larger length scales of breakage in the regimes closest to (but above) the yield point i.e., Region I and into Region II. [17] However, unlike the previous study, here we have remained at a fixed straining amplitude corresponding to Region II and instead observed the transient development of yielding at a strain amplitude sufficient to produce yielding. It is possible that their time-averaged assessment of Region II was unable to resolve the Region I process that transiently occurred early on. This explanation would thus assume that each progressively higher straining regime must to some extent undergo the yielding processes of all lower strain amplitude regimes, which was also shown by previous studies through the use of SPP analysis at different strain amplitudes. [17]

7.3.2 Stage 2: Plastic network rearrangement

The second region of yielding broadly describes the transition from distinct voids to emergent alignment of the voids, prior to full anisotropy, through plastic deformation and rearrangement of the continuous network. An analogous regime is proposed through the work of Kim et al. at very high strain amplitudes, in which the rheological response becomes dominated by a yielded structure instead of the pristine percolated network. [17] This structural feature is evident in the cumulative difference intensity, as shown in Figure 7.6(a). The change in difference intensity is empirically described well by a sigmoidal

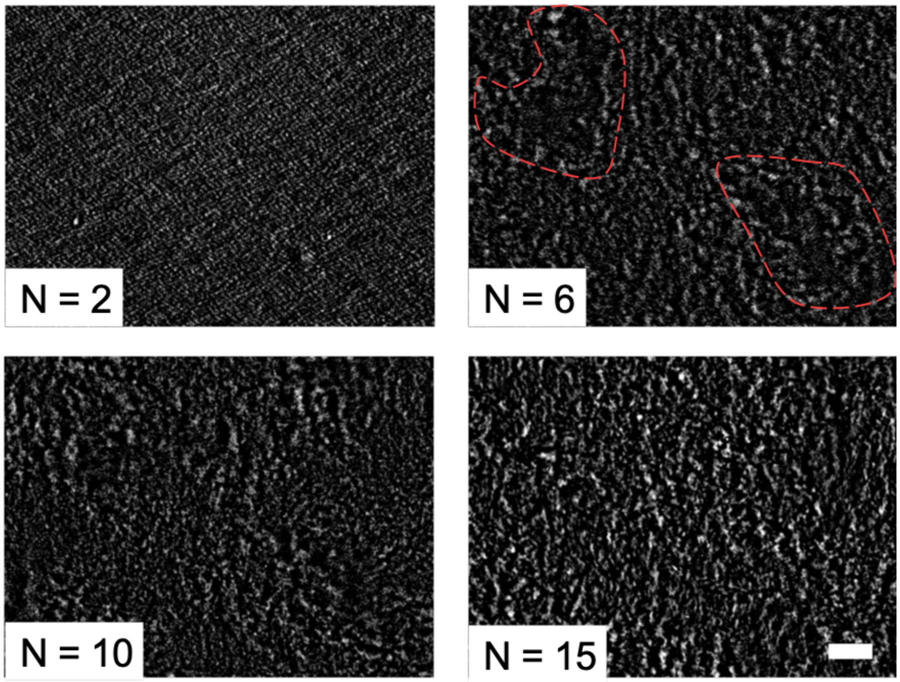

Figure 7.5: Non-affine difference images between the indicated cycle and the first cycle, rescaled in intensity to emphasize the circular voids for identification. Image are taken corresponding to the image closest to the peak strain of 20%, with an angular frequency of $20\,\mathrm{rad\,s^{-1}}$. The manually identified voids as traced by the dashed lines in cycle 6 are used to help the reader identify the voids which persist through cycle 10 and are non-existent by cycle 15, after which the vertical line spacing of clusters dominates. The scale bar is valid across all four images and indicates $50\,\mu\mathrm{m}$.

dependence of the form

$$I_\sigma(N) = I_\sigma^\infty + \frac{I_\sigma^0 - I_\sigma^\infty}{1 + \exp\left(\dfrac{N - N_{1/2}}{\Delta N}\right)} \tag{7.4}$$

where I_σ^∞ is the long-cycle plateau intensity difference, I_σ^0 is the short-cycle plateau intensity difference, $N_{1/2}$ is the inflection cycle, and ΔN is the steepness within the transition region. That a sigmoidal dependence captures the changes in cumulative difference intensity suggests that the density fluctuations experience the largest degree of rearrangement during this stage, and that they are bounded between two levels that apparently reflect the unyielded and yielded states.

Furthermore, the three steps of yielding are reflected in the residual modulus signal, as presented and shaded according to Figure 7.6(b).

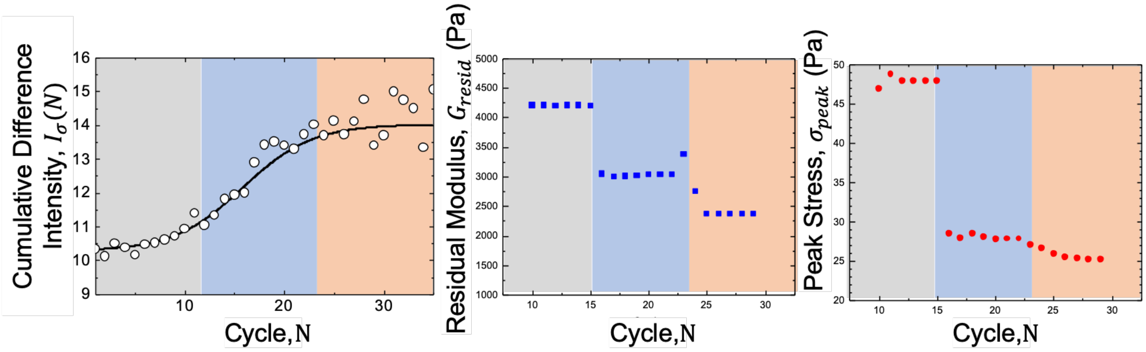

(a) (b) (c)

Figure 7.6: (a) Variations in the non-affine image standard deviation with cycle number, fit to a sigmoidal dependence as in Equation (7.4). Best fit parameters from a non-linear least squares regression give $I_\sigma^\infty = 14.0 \pm 0.2$, $I_\sigma^0 = 10.3 \pm 0.4$, $N_{1/2} = 15.8 \pm 1.5$ and $\Delta N = 3.5 \pm 1.3$. In (b) and (c), the key parameters extracted from intracycle rheological signal are plotted as a function of cycle number, using the definitions as outlined in Figure 7.4. The three steps apparent in the G_{resid} plot are used to color code the different cycle regions in all three subplots.

The structural onset of this second stage is thus marked by the inflection in I_σ, accompanying a marked, discontinuous decrease of G_{resid} and σ_{peak} that results from the loss of structural connectivity within the colloidal network. The steep decrease in G_{resid} coincides with the inflection in I_σ because the loss of gel integrity manifests structurally as the breakage of many network interconnects and plastic network rearrangement. Since these many breakage events should tend to increase the local density variations throughout the gel, we would reasonably expect I_σ (which roughly captures local density variations) to show a corresponding upturn. Similarly, the decrease in σ_{peak} reflects a permanent weakening of the gel structure in its plastic state, which would be consistent with an unrecoverable amount of bond breakages throughout the gel and thus increased local density fluctuations.

7.3.3 Stage 3: Formation of structural anisotropy

As the large voids continue to be sheared, they tend to align with the vorticity axis of flow. This has been observed in simulations of sheared colloidal gels at steady state [13] and transiently. [19] An order parameter reflecting the cluster anisotropy is calculated analogous to the alignment factor, expressed as: [20]

$$A_f = \frac{\int_0^{2\pi} Y(q,\phi)\cos(2\phi)\,\mathrm{d}\phi}{\int_0^{2\pi} Y(q,\phi)\,\mathrm{d}\phi}. \tag{7.5}$$

where $Y(q)$ is the intensity at wavevector q in Fourier space and ϕ is the angle relative to the right abscissa, corresponding to the flow axis. A spectrum will tend toward $A_f = 1$ as it aligns its lobes with the flow direction, whereas a fully isotropic system will have $A_f = 0$. As Figure 7.7(a) shows, the structural images and corresponding 2D Fourier spectra both demonstrate anisotropy either as seen in the aligned columns or the lobes, respectively. Extracting the physical spacing between log clusters from the dominant wavevector in Fourier space (i.e. the peak in $Y(q)$), we summarize in Figure 7.7(b) how the cluster spacing decays towards its plateau value, empirically fit as

$$L_c(N) = L_c^{\infty} + \left(L_c^0 - L_c^{\infty}\right)\exp\left(-N/N_\tau\right) \tag{7.6}$$

where L_c^{∞} is the long-cycle plateau roll spacing distance, L_c^0 is the initial roll spacing, and N_τ is the decay constant.

The apparent overshoot in cluster anisotropy is reminiscent of experimental observations in nonlinear steady shear, which report a transition through an intermediate stage of relatively higher anisotropy during the yielding process. This overshoot is attributed to microstructural rearrangements that immobilize the anisotropic structure prior to complete yielding. [19]

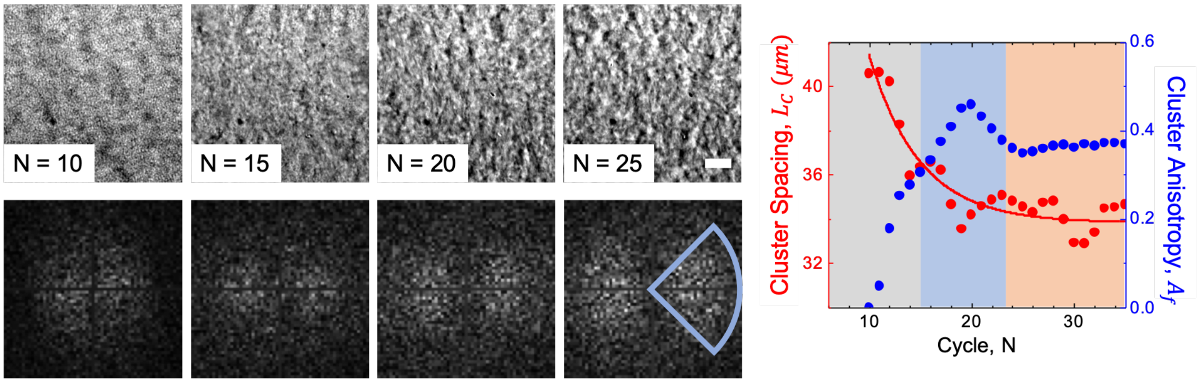

(a) (b)

Figure 7.7: The development of structural anisotropy is evident in the original microscopy images (scale bar 50 µm), in addition to the corresponding 2D Fourier transform of the image as seen in the lobed patters in (a). The quantitative measures we extract from (a) are then plotted in (b) with respect to cycle number, with the cluster spacing L_c in red arising from the peak wavevector in Fourier space, and the cluster anisotropy in blue reflecting the lobed nature of the 2D scattering as calculated by Equation (7.5). The cluster spacing is observed to follow an exponential decay, fit as Equation (7.6) with best fit parameters $L_c^\infty = 33.8 \pm 0.2\,\mu\text{m}$, $L_c^0 = 90 \pm 20\,\mu\text{m}$, and $N_\tau = 4.9 \pm 0.7$.

With respect to the corresponding rheological signature during this stage, we do not observe significant departures from the prior stage, as seen in Figure 7.6(b) and (c). However, we will note that given the anisotropic structure in this stage, it is possible that mechanical properties emerge in an orthogonal direction from the shear stress component probed. Such mechanical anisotropy would be accessible to characterization by alternative methods, such as orthogonal superposition rheometry. This could provide an effective means of describing the rheology of this stage further, [21] with the expectation that qualitatively different moduli values should arise.

7.3.4 Yielding process summary

Combining the stages thus presented, we arrive at a picture of intracycle yielding that is illustrated with Figure 7.8. Beginning from an unyielded gel, large amplitude straining

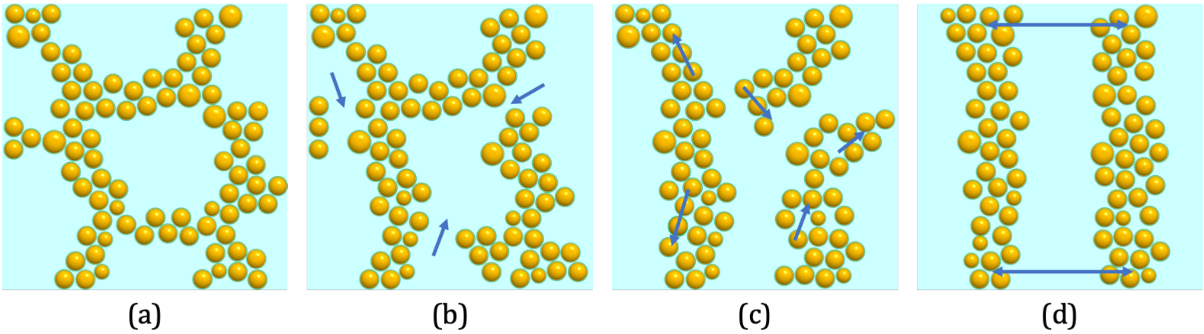

Figure 7.8: Summary schematic of the heterogeneous yielding process. (a) In the quiescent state, the colloidal gel exhibits a heterogeneous network structure comprising strands with tens of droplets in a bicontinuous arrested phase separation gel. (b) Stage 1 of yielding manifests as breakage of weak network interconnects, which has minimal effect on the dominant elasticity and length scale of heterogeneity associated with the network strands but results in a poroelastic flow of fluid into the newly formed narrow channels as indicated by the arrows. (c) Stage 2 corresponds with plastic deformation of the network strands deform and internally rearrange as represented by the movement arrows. The residual elastic modulus drastically declines due to weakening of the network backbone. (d) Stage 3 of yielding is the final stage during which network breakage goes to completion and anisotropic structures persist aligned along the vorticity axis, with a regular spacing indicated by the doubly ended arrows.

proceeds first by sparse network breakages that manifest as large scale voids and the presence of a σ_{peak} yielding feature. Moving on, as the voids collapse the remaining network undergoes more bond breakages and plastic deformation resulting in a stark drop in G_{resid} and increased local density fluctuations. Finally, as the anisotropic log clusters form which we can easily resolve due to their regular spacing, G_{resid} becomes its weakest due to the now absence of a rigid percolated structure.

7.4 Effects of frequency on anisotropy

The tunability of both LAOS interrogation and gel structure allows us to test different hypotheses for yielding mechanisms. As discussed in this chapter's introduction, frequency [17] and shear deformation rate (which is proportional to oscillation frequency) [13] have been reported to have a direct effect on the yield point and anisotropic structuration, respectively. Here we perform a simple test varying the imposed oscillation frequency to see its effect on log cluster spacing. Expanding from the initial test frequency of 5 rad s^{-1}, we show the resultant roll spacing at two other frequencies below and above, 2 rad s^{-1} and 20 rad s^{-1}. We follow the same procedure but now only focus on the final structure after aligned log clusters have formed. In performing these tests, we see that at higher frequencies the alignment take many more cycles to stabilize such that it is beyond the data acquisition limit of imaging throughout cyclic breakage. Nonetheless, we are able to observe a final structure by monitoring the structure over time and capturing the final image after 200 cycles.

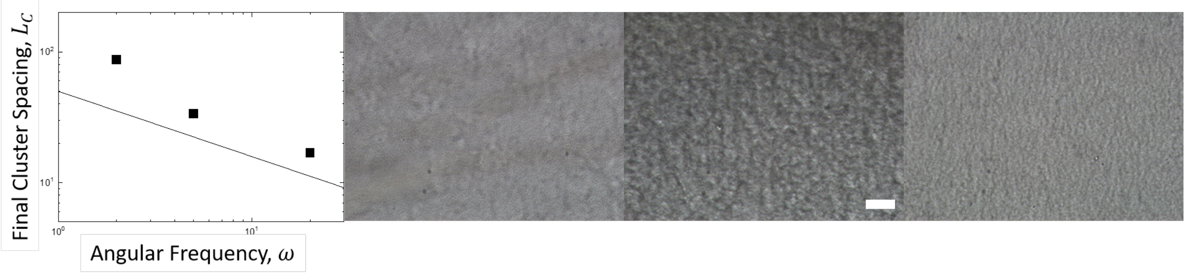

Figure 7.9: For a colloidal gel formed at 45 °C, varying oscillation frequencies for inputted LAOS signals results in variations in roll spacing after the gel has yielded. The far left shows the spacing, as determined via the Fourier signal, for varying frequencies. The scaling relationship plotted for reference is $L_c \propto \omega^{-1/2}$, comparing to simulations studies of large amplitude effects. [13] From left to right, increasing frequency changes the final aligned cluster sizing to progressively smaller sizes. Scale bar is 50 µm.

In recent simulation studies of sheared colloidal gels, Varge and Swan find that the alignment spacing varies according to the Mason number, which describes the strength of the shear force due to oscillations relative to the bond force of particles in contact. [13] The Mason number is calculated as

$$Mn = \frac{6\pi\eta_S a^2 \delta\omega_0\gamma_0}{U} \tag{7.7}$$

where η_S is the solvent viscosity, a is the colloid radius, δ is the width of interaction, ω_0 is the angular oscillation frequency, γ_0 is the strain amplitude, and U is the interaction strength. Under the conditions known for our system and using the Two-Yukawa potential as developed in Chapter 3, we estimate a Mason number of order 10^{-4}. Although the simulations have shown this region of Mason number to have constant spacing with respect to frequency, we observe scaling similar to the high Mason number of $L_c \propto Mn^{-1/2} \propto \omega^{-1/2}$. This discrepancy may be resolved by considering the renormalized Mason number as suggested by Varga and Swan, which for our system is negative and corresponds to bond forces weaker than those studied in simulation. [13] Thus the depletion gel simulation findings may not be entirely correct for our nanoemulsion colloidal gel system, which in comparison has a higher rate of bond breakage.

7.5 Conclusions

In this chapter we have laid out experimental considerations and analysis for interrogating the yielding process of colloidal gels under large amplitude strain. We focus on a single processing temperature to highlight the three-step yielding process that we expect to see in further study of thermal processing variations. This three-step process involves void formation, plastic deformation, and finally the anisotropic alignment as evidenced by both microstructural analysis and reflected in intracycle rheological measurements.

The LAOS study presented thus far has not addressed some salient opportunities through use of the thermoresponsive nanoemulsion system. Notably, the systematic variation in arrested gel length scale with quench depth could provide a means of independently tuning structural length scale (via arrest temperature) and bond strength (via temperature during yielding). The ability to observe the rheological and microscopic consequences of large amplitude strain at fixed bond strength but varying length scale, or vice versa, should provide definitive insight into the governing physics of colloidal gel yielding.

Bibliography

[1] K. Hyun, M. Wilhelm, C. O. Klein, K. S. Cho, J. G. Nam, K. H. Ahn, S. J. Lee, R. H. Ewoldt, and G. H. McKinley, "A review of nonlinear oscillatory shear tests: Analysis and application of large amplitude oscillatory shear (laos)," *Progress in Polymer Science*, vol. 36, no. 12, pp. 1697–1753, 2011.

[2] F. Renou, J. Stellbrink, and G. Petekidis, "Yielding processes in a colloidal glass of soft star-like micelles under large amplitude oscillatory shear (laos)," *Journal of Rheology*, vol. 54, no. 6, pp. 1219–1242, 2010.

[3] R. H. Ewoldt, A. E. Hosoi, and G. H. McKinley, "Rheological fingerprinting of complex fluids using large amplitude oscillatory shear (laos) flow," *Annual Transactions-Nordic Rheology Society*, vol. 15, p. 3, 2007.

[4] S. A. Rogers and M. P. Lettinga, "A sequence of physical processes determined and quantified in large-amplitude oscillatory shear (laos): Application to theoretical nonlinear models," *Journal of Rheology*, vol. 56, no. 1, p. 1, 2011.

[5] D. Bonn, M. M. Denn, L. Berthier, T. Divoux, and S. Manneville, "Yield stress materials in soft condensed matter," *Reviews of Modern Physics*, vol. 89, no. 3, p. 035005, 2017.

[6] Z. Shao, A. S. Negi, and C. O. Osuji, "Role of interparticle attraction in the yielding response of microgel suspensions," *Soft Matter*, vol. 9, no. 22, pp. 5492–5500, 2013.

[7] K. Pham, G. Petekidis, D. Vlassopoulos, S. Egelhaaf, P. Pusey, and W. Poon, "Yielding of colloidal glasses," *EPL (Europhysics Letters)*, vol. 75, no. 4, p. 624, 2006.

[8] K. Pham, G. Petekidis, D. Vlassopoulos, S. Egelhaaf, W. Poon, and P. Pusey, "Yield-

ing behavior of repulsion-and attraction-dominated colloidal glasses," *Journal of Rheology*, vol. 52, no. 2, pp. 649–676, 2008.

[9] M. Laurati, S. Egelhaaf, and G. Petekidis, "Nonlinear rheology of colloidal gels with intermediate volume fraction," *Journal of Rheology*, vol. 55, no. 3, pp. 673–706, 2011.

[10] H. K. Chan and A. Mohraz, "Two-step yielding and directional strain-induced strengthening in dilute colloidal gels," *Physical Review E*, vol. 85, no. 4, p. 041403, 2012.

[11] T. Gibaud, D. Frelat, and S. Manneville, "Heterogeneous yielding dynamics in a colloidal gel," *Soft Matter*, vol. 6, no. 15, pp. 3482–3488, 2010.

[12] C. O. Osuji and D. A. Weitz, "Highly anisotropic vorticity aligned structures in a shear thickening attractive colloidal system," *Soft Matter*, vol. 4, no. 7, pp. 1388–1392, 2008.

[13] Z. Varga and J. W. Swan, "Large scale anisotropies in sheared colloidal gels," *Journal of Rheology*, vol. 62, no. 2, pp. 405–418, 2018.

[14] J. Vermant and M. Solomon, "Flow-induced structure in colloidal suspensions," *Journal of Physics: Condensed Matter*, vol. 17, no. 4, p. R187, 2005.

[15] B. Rajaram and A. Mohraz, "Dynamics of shear-induced yielding and flow in dilute colloidal gels," *Physical Review E*, vol. 84, no. 1, p. 011405, 2011.

[16] Z. Varga, V. Grenard, S. Pecorario, N. Taberlet, V. Dolique, S. Manneville, T. Divoux, G. H. McKinley, and J. W. Swan, "Hydrodynamics control shear-induced pattern formation in attractive suspensions," *Proceedings of the National Academy of Sciences*, vol. 116, no. 25, pp. 12193–12198, 2019.

[17] J. Kim, D. Merger, M. Wilhelm, and M. E. Helgeson, “Microstructure and nonlinear signatures of yielding in a heterogeneous colloidal gel under large amplitude oscillatory shear,” *Journal of Rheology (1978-present)*, vol. 58, no. 5, pp. 1359–1390, 2014.

[18] P. Cha, *Fundamentals of signals and systems : a building block approach.* Cambridge, UK New York: Cambridge University Press, 2006.

[19] B. Rajaram and A. Mohraz, “Microstructural response of dilute colloidal gels to nonlinear shear deformation,” *Soft Matter*, vol. 6, no. 10, pp. 2246–2259, 2010.

[20] L. M. Walker and N. J. Wagner, “Sans analysis of the molecular order in poly (γ-benzyl l-glutamate)/deuterated dimethylformamide (pblg/d-dmf) under shear and during relaxation,” *Macromolecules*, vol. 29, no. 6, pp. 2298–2301, 1996.

[21] E. Moghimi, J. Vermant, and G. Petekidis, “Orthogonal superposition rheometry of model colloidal glasses with short-ranged attractions,” *Journal of Rheology*, vol. 63, no. 4, pp. 533–546, 2019.

Chapter 8

Conclusions and Future Work

Understanding colloidal gels as complex, non-equilibrium materials presents a challenge to their study but also an opportunity for the development of novel soft materials relevant to emergent industries such as additive manufacturing and biomaterial production. The findings presented in this dissertation have hopefully shown that understanding colloidal gelation can be achieved by evaluating phase behavior, processing kinetics, and properties of a model thermoresponsive colloidal gel system. The findings that support this assertion are summarily reiterated now.

8.1 Summary of scientific contributions

8.1.1 Colloidal gel phase behavior

We established a two Yukawa interaction potential between nanodroplets in the presence of thermoresponsive bridging polymers through statistical mechanical arguments. We find that the model provides useful parameters that capture the expected temperature-dependence of polymer bridging distance between associated droplets. From neutron scattering data, we successfully extracted a set of parameters that was consistent with the observed thermoresponsive nanoemulsion behavior.

Further, we developed mean field predictions for the equilibrium phase behavior underlying the thermoresponsive nanoemulsion system through a variational free energy technique. We found that the predicted phase coexistence region agrees well with experiments and simulations to the same effect. This finding further validates the interaction potentials chosen to model the system and supports our claim that the equilibrium phase behavior continues to dictate to some extent the features of colloidal gel strand formation below the dynamic gel arrest line.

8.1.2 Colloidal gel processing kinetics

We used the materials processing framework of isothermal transformations to rationalize the sequence of transitions that occur during colloidal gelation and arrest. We observed a recurring motif of mechanical gelation, delayed yet rapid coarsening, and then prolonged arrest that follows with isothermal colloidal gel aging in the spinodal region. The ratio of kinetic time scales for these regions compares well between experiments and molecular dynamics simulations, and the two exhibit qualitatively similar trends with respect to quench depth, indicating that the relevant time scale of gelation is self-consistent. These results provide a road map for processing colloidal gels with controlled heterogeneity arising from phase separation and reveal opportunities for sculpting gel properties prior to prolonged arrest.

Through study of the structure formation and elasticity of colloidal gels formed *via* thermoresponsive attractions, we also showed that macroscopic behavior reflects the temperature dependence of coarsening and arrest kinetics during gelation, as modulated by attractions between substituent colloids. The quench dependence of coarsening rates proved consistent with scaling arguments for late stage spinodal decomposition. Additionally, we found that the nondimensional elastic modulus exhibits an order of magnitude variation with varying quench depth, suggesting that current theories for colloidal gel elasticity require modification to account for additional material descriptors to sufficiently describe their scaling behavior.

8.1.3 Colloidal gel yielding properties

Finally, we laid out experimental considerations and analysis for studying gel yielding under large amplitude strain. For a single temperature we detailed the three-step yielding process involving void formation, plastic deformation, and anisotropic alignment through both microstructural rheological analyses. These early results showed that we can indeed achieve detailed insight into the colloidal gel yielding process.

8.2 Future directions

We believe that the present work provides a clear foundation for future directions to pursue with respect to the broad strategy of colloidal gel engineering and soft material development. The additional studies suggested subsequently will not only deepen our understanding of themroreversible gelation but also demonstrate its viability as a material development platform.

8.2.1 Effect of thermoreversible chemistry on colloidal behavior

To develop a deeper understanding and intuition of thermoresponsive colloidal gel behavior, this dissertation concerned itself with a single material system comprising the silicone oil, SDS surfactant, and PEGDA bridging polymer. Returning to the original discovery of the thermoresponsive bridging phenomenon, it is clear that this particular combination of chemical species is not necessary to achieving thermoreversible colloidal gelation. Rather, thermoreversible gelation is observed for a variety of other PEG end group chemistries of varying hydrophobicity. [1] It stands to reason that these other chemistries should behave similarly to the PEGDA system in terms of qualitative behavior, but differences in their quantitative behavior may reveal more details about the underlying mechanism and more general design rules for engineered selection of a particular combination of oil, surfactant, and bridging polymer moieties.

8.2.2 Templating hierarchical porosity in polymeric materials

Porous soft materials made from colloidally processed pre-cursors are a common motif in biological systems, including mussel plaques and tissue scaffolds. [2, 3] They provide a much larger surface area for cell adhesion, as well as reduce the amount of material while providing comparable if not improved mechanical performance. [4] The ability to rationally explain the effects of gel porosity, however, is predicated on the ability to systematically generate bulk porous structures of varying pore size and density.

The thermoresponsive nanoemulsion system is well-suited for use as a fluid template for generating porous polymeric materials. Given the inherent two-phase chemistry of the system in terms of the oil and water components, it is feasible to generate porous polymers through the introduction of continuous phase crosslinking agents. As observed in several studies of the thermoresponsive nanoemulsion system, bulk length scales on the order of one to ten microns can be achieved and presumably transferred to the final porous material. [5–8]

Bibliography

[1] M. E. Helgeson, S. E. Moran, H. Z. An, and P. S. Doyle, "Mesoporous organohydrogels from thermogelling photocrosslinkable nanoemulsions," *Nature Materials*, vol. 11, pp. 344–352, February 2012.

[2] E. Filippidi, D. G. DeMartini, P. Malo de Molina, E. W. Danner, J. Kim, M. E. Helgeson, J. H. Waite, and M. T. Valentine, "The microscopic network structure of mussel (Mytilus) adhesive plaques," *Journal of The Royal Society Interface*, vol. 12, p. 20150827, dec 2015.

[3] S. J. Hollister, "Porous scaffold design for tissue engineering," *Nature materials*, vol. 4, no. 7, pp. 518–524, 2005.

[4] K. W. Desmond, N. A. Zacchia, J. H. Waite, and M. T. Valentine, "Dynamics of mussel plaque detachment," *Soft Matter*, vol. 11, no. 34, pp. 6832–6839, 2015.

[5] Y. Gao, J. Kim, and M. E. Helgeson, "Microdynamics and arrest of coarsening during spinodal decomposition in thermoreversible colloidal gels," *Soft Matter*, vol. 11, no. 32, pp. 6360–6370, 2015.

[6] L. C. Hsiao and P. S. Doyle, "Celebrating soft matter's 10th anniversary: Sequential phase transitions in thermoresponsive nanoemulsions," *Soft Matter*, vol. 11, no. 43, pp. 8426–8431, 2015.

[7] L.-C. Cheng, Z. M. Sherman, J. W. Swan, and P. S. Doyle, "Colloidal gelation through thermally triggered surfactant displacement," *Langmuir*, vol. 35, no. 29, pp. 9464–9473, 2019.

[8] L.-C. Cheng, S. M. Hashemnejad, B. Zarket, S. Muthukrishnan, and P. S. Doyle,

"Thermally and ph-responsive gelation of nanoemulsions stabilized by weak acid surfactants," *Journal of Colloid and Interface Science*, 2019.

Appendix A

Derivation of Reparameterized Two Yukawa

The form of the Two Yukawa interaction potential is given by the following equation, in dimensionless distance $\tilde{r} = \frac{r}{a}$:

$$U(\tilde{r}) = K_1 \frac{\mathrm{e}^{-z_1(\tilde{r}-1)}}{\tilde{r}} - K_2 \frac{\mathrm{e}^{-z_2(\tilde{r}-1)}}{\tilde{r}}. \tag{A.1}$$

This general form does not provide sufficient intuition in terms of a physical description of the system. Of greater relevance to our polymer bridging work is the attractive well that is present in this family of curves. Towards a more physically meaningful form, we recast the strength parameters K_1 and K_2 into the parameters r_m and U_m, which specify the location and depth of the attractive well minimum, respectively.

First we find the location of the well minimum based on the first spatial derivative of the potential

$$\frac{\mathrm{d}U(\tilde{r})}{\mathrm{d}\tilde{r}} = K_1 \frac{-z_1\tilde{r}\mathrm{e}^{-z_1(\tilde{r}-1)} - \mathrm{e}^{-z_1(\tilde{r}-1)}}{\tilde{r}^2} - K_2 \frac{-z_2\tilde{r}\mathrm{e}^{-z_2(\tilde{r}-1)} - \mathrm{e}^{-z_2(\tilde{r}-1)}}{\tilde{r}^2}$$

$$\frac{\mathrm{d}U(\tilde{r})}{\mathrm{d}\tilde{r}} = -K_1 \frac{(z_1\tilde{r}+1)\mathrm{e}^{-z_1(\tilde{r}-1)}}{\tilde{r}^2} + K_2 \frac{(z_2\tilde{r}+1)\mathrm{e}^{-z_2(\tilde{r}-1)}}{\tilde{r}^2} \tag{A.2}$$

The finite-valued location of the well mimum will satisfy $\left.\frac{\mathrm{d}U(\tilde{r})}{\mathrm{d}\tilde{r}}\right|_{\tilde{r}=\tilde{r}_m} = 0$, which then allows us to write K_2 in terms of K_1 and $\tilde{r}_m$. We start by setting Equation (A.2) to zero and evaluating at $\tilde{r}_m$

$$0 = -K_1 \frac{(z_1\tilde{r}_m+1)\mathrm{e}^{-z_1(\tilde{r}_m-1)}}{\tilde{r}_m^2} + K_2 \frac{(z_2\tilde{r}_m+1)\mathrm{e}^{-z_2(\tilde{r}_m-1)}}{\tilde{r}_m^2}$$

$$K_2 = K_1 \frac{(z_1\tilde{r}_m+1)}{(z_2\tilde{r}_m+1)} \frac{\mathrm{e}^{-z_1(\tilde{r}_m-1)}}{\mathrm{e}^{-z_2(\tilde{r}_m-1)}} \tag{A.3}$$

By specifying the well depth, we have inherently constrained $U(\tilde{r}_m) = -U_m$, which now allows us to solve for K_1 in terms of U_m, z_1, and z_2. First we plug Equation (A.3) into Equation (A.1), then evaluate at $\tilde{r}_m$

$$U(\tilde{r}) = K_1 \frac{\mathrm{e}^{-z_1(\tilde{r}-1)}}{\tilde{r}} - K_1 \frac{(z_1\tilde{r}_m+1)}{(z_2\tilde{r}_m+1)} \frac{\mathrm{e}^{-z_1(\tilde{r}_m-1)}}{\mathrm{e}^{-z_2(\tilde{r}_m-1)}} \frac{\mathrm{e}^{-z_2(\tilde{r}-1)}}{\tilde{r}}$$

$$U(\tilde{r}_m) = -U_m = K_1 \left[\frac{\mathrm{e}^{-z_1(\tilde{r}_m-1)}}{\tilde{r}_m} - \frac{(z_1\tilde{r}_m+1)}{(z_2\tilde{r}_m+1)} \frac{\mathrm{e}^{-z_1(\tilde{r}_m-1)}}{\mathrm{e}^{-z_2(\tilde{r}_m-1)}} \frac{\mathrm{e}^{-z_2(\tilde{r}_m-1)}}{\tilde{r}_m} \right]$$

$$-U_m = K_1 \frac{\mathrm{e}^{-z_1(\tilde{r}_m-1)}}{\tilde{r}_m} \left[1 - \frac{(z_1\tilde{r}_m+1)}{(z_2\tilde{r}_m+1)} \right]$$

$$K_1 = \frac{-U_m\tilde{r}_m\mathrm{e}^{z_1(\tilde{r}_m-1)}}{1 - \dfrac{(z_1\tilde{r}_m+1)}{(z_2\tilde{r}_m+1)}} \tag{A.4}$$

By substituting Equations (A.3) and (A.4) into the original Two Yukawa potential of

Equation (A.1), we simplify to

$$
\begin{aligned}
U(\tilde{r}) &= \frac{-U_m\tilde{r}_m \mathrm{e}^{z_1(\tilde{r}_m-1)}}{1-\dfrac{(z_1\tilde{r}_m+1)}{(z_2\tilde{r}_m+1)}}\left[\frac{\mathrm{e}^{-z_1(\tilde{r}-1)}}{\tilde{r}}-\frac{(z_1\tilde{r}_m+1)}{(z_2\tilde{r}_m+1)}\frac{\mathrm{e}^{-z_1(\tilde{r}_m-1)}}{\mathrm{e}^{-z_2(\tilde{r}_m-1)}}\frac{\mathrm{e}^{-z_2(\tilde{r}-1)}}{\tilde{r}}\right] \\
U(\tilde{r}) &= \frac{-U_m\tilde{r}_m(z_2\tilde{r}_m+1)}{(z_2-z_1)\tilde{r}_m}\left[\frac{\mathrm{e}^{-z_1(\tilde{r}-\tilde{r}_m)}}{\tilde{r}}-\frac{(z_1\tilde{r}_m+1)}{(z_2\tilde{r}_m+1)}\frac{\mathrm{e}^{-z_2(\tilde{r}-\tilde{r}_m)}}{\tilde{r}}\right] \\
U(\tilde{r}) &= \frac{-U_m}{(z_2-z_1)}\left[(z_2\tilde{r}_m+1)\frac{\mathrm{e}^{-z_1(\tilde{r}-\tilde{r}_m)}}{\tilde{r}}-(z_1\tilde{r}_m+1)\frac{\mathrm{e}^{-z_2(\tilde{r}-\tilde{r}_m)}}{\tilde{r}}\right] \qquad \text{(A.5)}
\end{aligned}
$$

which provides an operative equation for specifying the Two Yukawa potential in terms of $\tilde{r}_m$, U_m, z_1, and z_2. Notes: (1) this form diverges as $(z_2 - z_1) \to 0$; (2) we can write the relationships

$$
\begin{aligned}
K_1 &= \frac{-U_m}{z_2-z_1}(z_2\tilde{r}_m+1)\mathrm{e}^{z_1(\tilde{r}_m-1)} \\
K_2 &= \frac{U_m}{z_2-z_1}(z_1\tilde{r}_m+1)\mathrm{e}^{z_2(\tilde{r}_m-1)}
\end{aligned}
$$

to connect back to the initial form; (3) The transformation from K_1 and K_2 to $\tilde{r}_m$ and U_m is provided by the above system of two nonlinear equations.

Appendix B

MATLAB Code for Variational Free Energy Calculations

Generally, the code developed below carries out a common tangent construction on a variational free energy curve to determine mean field predictions of the binodal and spinodal of a given two Yukawa interaction potential. The technique follows the equations and methods outlined by Tejero et al. [1] The common tangent is calculated by finding the point at which the first local minimum of the difference between the free energy function and the tangent line at a point is equal to zero. Parameters introduced to address numerical accuracy include the step size between values of specific volume, the amplification factor to increase the accuracy of the common tangent calculation. Additionally, various flags are introduced to update the user on the progress of the calculations during execution.

As presented, the code below was used to validate the literature datapoint from Tejero et al. corresponding to their dimensionless temperature $t = 0.9$, for an interaction width (using their definition) of 1.34.

```
% amp Scales up differences by a billion to clearly
```

```
% identify minima
amp = 1000000;
% verbose tells whether to output steps
verbose = 1;
talkStep = 50000;
tangentTalkStep = 0.1;

ind = 15000;

doPlot = 0;
%Assumes that the function sufficiently decays by rMax
rMin = 1;
rMax = 1.6;

lMin = 0.75;
lMax = 1.25;

rhoInvMin = 1;
rhoStepSize = .01;
rhoInvMax = 200;

resn = 0.0001;

firstMin = 1;

saveStuff = 1;

skipBeta = 0;
file='Tej-1p34-0p9';
K1 = 2.1;%4.530054;
Z1 = 2.7;%22.23921;
```

```
K2 = -2.1;%-0.835;
Z2 = 14.4;%3.055266;

%Umin = 3.875;

%K1 = 2.376802224 * Umin;
%Z1 = 8.5;
%K2 = -7.624713267 * Umin;
%Z2 = 49.34675;

if ~skipBeta

        lambda = lMin:resn:lMax;
        lam3 = lambda.^3;
        r = rMin:resn:rMax;

        [~,eps] = TwoYukawa(r,K1,Z1,K2,Z2);
        t = .9;%1/eps

        m = 1;
        sigma_HS = 1;
        h = 1;

        phi_inv = rhoInvMin:rhoStepSize:rhoInvMax;
        fVars = zeros(1,size(phi_inv,2));

        for i=1:size(phi_inv,2)

        rhoBar = 6/pi./phi_inv(i);
        phi  = pi*rhoBar.*lam3/6;
```

```
phi = phi(phi<1);
lambda = lambda(phi<1);
lam3 = lam3(phi<1);

betaf2 = log(rhoBar)-3*log(t)/2+3*log(h)b@x...
    -3*log(2*pi*m*eps)/2...
    -3*log(sigma_HS) +3*log(lambda) -1 +fExcess(phi) ...
    +2*pi*rhoBar*K1/eps/t*lam3.*( ...
    -K2/K1*Z2*exp(Z2)*Hfnc(Z2*lambda,phi) ...
    -Z1*exp(Z1)*Hfnc(Z1*lambda,phi) );

if phi_inv(i)==50
    keybetaf2 = betaf2;
    keyHS = log(rhoBar)-3*log(t)/2 ...
    +3*log(h)-3*log(2*pi*m*eps)/2...
    -3*log(sigma_HS) +3*log(lambda) -1 +fExcess(phi);
    key2Y = 2*pi*rhoBar*K1/eps/t*lam3.*( ...
    -K2/K1*Z2*exp(Z2)*Hfnc(Z2*lambda,phi) ...
    -Z1*exp(Z1)*Hfnc(Z1*lambda,phi) );
end

if ~isreal(betaf2)
        display('oof')
        display(phi_inv(i))
end

if ~mod(i,talkStep)&&verbose
        display(i)
end

if doPlot && i==1
```

```
                    plot(lambda,betaf2)
                    axis([.8 1.2 -10 10])
                    Ycheck = betaf2;
                    Xcheck = lambda;
            end
            fVars(i) = min(real(betaf2));
            end
end
g = gradient(fVars,rhoStepSize);

display(ind)
while firstMin > 0

            zVal = fVars-(g(ind)*(phi_inv-phi_inv(ind))+fVars(ind));
            TF = islocalmin(amp*zVal);

            minValues = zVal(TF);
            ind = ind-1;

            firstMin = minValues(1);
            if ~mod(ind,talkStep*tangentTalkStep)&&verbose
            display(ind)
            end
end




figure(1);
plot(phi_inv,fVars);
hold on
```

```
gPtSlope = g(ind)*(phi_inv-phi_inv(ind))+fVars(ind);

plot(phi_inv,gPtSlope)
axis([1 rhoInvMax min(fVars) 5])
hold off

figure(2);
plot(phi_inv,zVal,phi_inv,zeros(1,size(phi_inv,2)),...
    phi_inv(TF),zVal(TF),'r*')
axis([1 rhoInvMax -1e-4 10000])
axis([1 rhoInvMax -1/amp 1/amp])

rho = 6/pi./phi_inv(TF);

figure(1)
if saveStuff
        saveas(gcf,file,'fig')
end

figure(2)
if saveStuff
        saveas(gcf,strcat(file,'-zeroCheck'),'fig')
end

%clear g TF gPtSlope lam3

if saveStuff
        save(strcat(file,'.mat'))
end
```

Bibliography

[1] C. Tejero, A. Daanoun, H. Lakkerkerker, and M. Baus, "Isostructural solid-solid transition of (colloidal) simple fluids," *Physical Review E*, vol. 51, no. 1, p. 558, 1995.